A CHARACTERIZATION OF FLAT-PLATE HEAT EXCHANGERS FOR THERMAL LOAD MANAGEMENT OF THERMOELECTRIC GENERATORS

A CHARACTERIZATION OF FLAT-PLATE HEAT EXCHANGERS FOR THERMAL LOAD MANAGEMENT OF THERMOELECTRIC GENERATORS

BY

YAKOOB HANA, B.Eng.

A THESIS
SUMBITTED TO THE DEPARTMENT OF MECHANICAL ENGINEERING
AND THE SCHOOL OF GRADUATE STUDIES
OF MCMASTER UNIVERSITY
IN PARTIAL FULFILMENT OF THE REQUIREMENTS
FOR THE DEGREE OF
MASTER OF APPLIED SCIENCE

Master of Applied Science (2014) McMaster University

(Mechanical Engineering) Hamilton, Ontario, Canada

TITLE: A Characterization of Flat-Plate Heat Exchangers for Thermal Load Management of Thermoelectric Generators

AUTHOR: Yakoob Hana

B.Sc., (Mechanical Engineering)

McMaster University, Hamilton, Canada

SUPERVISOR: Dr. James Cotton

NUMBER OF PAGES: xix, 168

Abstract

Thermoelectric generator (TEG) is a solid state technology based on the Seebeck effect that can generate electrical power from waste heat. For continuous electrical power generation heat exchangers are integrated into the "cold side" and the "hot side" of the TEG such that a temperature difference across the TEG can be established and maintained. This thesis will focus on characterizing two different flat-plate cold side heat exchanger prototypes specifically designed for dissipating the thermal loads from TEG modules.

The majority of TEGs modules available have a flat geometry design and a square shape with typical dimension of 40 mm × 40 mm or 56 mm × 56 mm. To maximize the net electrical power generated by the TEGs the cold side heat exchanger is required to have uniform surface temperature distribution, and excellent heat transfer performance with minimum pressure drop.

To achieve the previously mentioned requirements, two flat-plate heat exchanger prototypes having two distinct heat transfer techniques were investigated. Each heat exchanger is designed to accommodate an array of 14 TEG modules arranged in two parallel rows with 7 TEGs per row a typical arrangement for large waste energy harvesting applications.

The first heat exchanger prototype utilized single-phase forced convection through 140 minichannels (1 mm × 1 mm × 90 mm long) as a heat transfer technique. The second prototype utilized 14 liquid jets, 3 mm in diameter and 40.3 mm apart, impinging on a flat surface located 5 mm above. Each impinging jets was positioned at the centre of the TEG cooling area.

An experimental facility was constructed in order to test the minichannels heat exchanger and the impinging jets thermally and

hydrodynamically. The heat transfer, pressure drop and temperature distribution results were compared to determine the most appropriate cold side heat exchanger prototype for the TEG POWER system. The TEG POWER system is a waste heat recovery system designed to recoup waste heat from the exhaust gases of commercial pizza ovens. The TEG POWER system is capable of harvesting waste thermal energy produced by an establishment and utilize it for electrical power generation and thermal storage purposes.

Heat transfer results indicated that for a given mass flow rate the minichannels heat exchanger has better heat transfer performance compared to the impinging jets heat exchanger. The minichannels heat exchanger design had a thermal conductance of 238 W/°C at 0.19 kg/s coolant flow rate compared to 111 W/°C for the impinging jets heat exchanger.

The total pressure drop and the minor losses for each heat exchanger prototype were measured experimentally. For the minichannels heat exchanger, the total pressure drop is 23.3 kPa at flow rate of 0.235 kg/s. Comparatively, the total pressure drop for the impinging jets heat exchanger was 27.4 kPa at the same flow rate. Fittings losses for the minichannels heat and impinging jets heat exchanger were found to be 50% and 80% respectively. The maximum total measured drop corresponded to pumping power requirements of 5.7 W and 6.8 W for the minichannels and impinging jets heat exchanger respectively.

Local and average temperature distributions and their influence on the electrical power generated were studied for both heat exchanger prototypes. It was found that the minichannels heat exchanger offers more uniform surface temperature distribution per row of TEGs compared to the impinging jets heat exchanger. Therefore the minichannels heat exchanger is well suited for cooling two rows of TEGs simultaneously.

Based on the thermal and hydrodynamics comparison results the minichannels heat exchanger prototype is recommended for implementation in the TEG POWER system.

Acknowledgements

I would like to extend my sincere gratitude to my supervisor Dr. James Cotton for his continuous and unlimited support throughout the past two years. Thank you for giving me the chance to work with yourself and the *awesome* TMRL team.

I would also like to thank Dr. Hossam Sadek for providing me with unlimited help, motivation and valuable advice during the course of this project. In addition, I would like to express my gratitude to Dr. Chan Ching who frequently asked about the status of my research.

To Raf, Jeff, Corbin, Donal and Mike who made the TEG team a wonderful group to work with.

To all the members of the TMRL research group who had, *often*, endured the pain of listening to my lengthy progress presentations.

To the mechanical engineering shop technicians: Ron, Mark, Michael and Joe, thank you for your technical guidance and unlimited help while working at the machine shop.

For the project industry sponsors Thermal Electronics Corp., Pizza Pizza, Acrolab, N.S.E.R.C., and O.C.E. and who provided financial support for this project.

To all my friends inside and outside the university community who kept me company throughout the years.

Most importantly, to my wonderful and loving family who have always provided endless support and continuous encouragement.

To *you*, for taking the time to read all my acknowledgments.

Table of Contents

List of Figures

List of Tables

Nomenclature and Abbreviations

Nomenclature

$\dot{m}$	Mass flow rate (kg/s)
$\dot{\forall}$	Volume flow rate (m^3/s)
A	Convection area (m^2)
A_{flow}	Flow area (m^2)
A_{ss}	Cross sectional area of the stainless steel block (m^2)
B	Bias error
C_p	Specific heat capacity (kJ/kg·K)
CAD	Computer aided design
D	Diameter (mm)
d_h	Diameter of the heated surface (mm)
D_h	Hydraulic diameter (mm)
D_j	Jet diameter (mm)
f	Darcy friction factor
f_{app}	Apparent Darcy friction factor
f_{app}^*	Apparent Fanning friction factor
h	Average heat transfer coefficient ($W/m^2 \cdot K$)
H	Jet to target distance (mm)
H_{ch}	Channel height (mm)
hA	Thermal conductance (W/K)
HX	Heat exchanger
k	Thermal conductivity (W/m·K)
$K(\infty)$	Fully developed Hagenbach factor
K_e	Expansion loss coefficient
K_c	Contraction loss coefficient
l	Jet orifice plate thickness (mm)
L	Length (m), characteristic fin length (mm)
L_{ch}	Minichannel length (mm)
L_{hy}	Hydrodynamic entrance length (mm)
L_{th}	Thermal entrance length (mm)
N_{ch}	Number of minichannels
N_j	Number of impinging jets
Nu	Average Nusselt number

Nu_0	Stagnation Nusselt number
Nu_x	Local Nusselt number
ΔP	Pressure drop between two locations, total pressure drop across a heat exchanger (kPa)
P	Precision error, perimeter (m)
P_E	Electrical power (W)
P_p	Hydraulic pumping power (W)
TEG POWER	Acronym for TEG Pizza Oven Waste Heat Recovery
Pr	Prandtl number
q''	Heat flux W/m^2
$Q_{heaters}$	Thermal energy generated by the electrical heaters (W)
Q_{HX}	Thermal energy transferred from the heat exchanger to the cooling water (W)
Q_{ss}	Thermal energy flowing through the stainless steel block (W)
Q_{water}	Thermal energy transferred to the cooling water (W)
r	Radial distance from the jet centre
R	Thermal resistance (°C/W)
Re	Reynolds number
RTD	Resistive temperature device
S	Lateral spacing between adjacent jets (mm)
ΔT	Temperature difference between two locations (°C)
ΔT_{LM_CL}	Log-mean temperature difference calculated using the centerline slope (°C)
T	Temperature (°C)
T_{Cold}	Temperature of the TEG's cold side (°C)
T_{copper}	Temperature of the copper block (°C)
T_{Hot}	Temperature of the TEG's hot side (°C)
T_{ss}	Measured temperature of the stainless steel block for a given location (°C)
T_{w_in}	Measured inlet water temperature(°C)
$\bar{T}_{w\_in}$	Calculated average water temperature (°C)
T_{w_out}	Measured outlet water temperature(°C)
$\bar{T}_{w\_out}$	Calculated average water temperature (°C)
T_{s_CL}	Surface temperature at the interface between the heat exchanger wall and the cooling water based on the

	centerline slope (°C)
$\left(\frac{dT}{dx}\right)_{ss}$	Temperature gradient in the stainless steel block (°C/m)
TEG	Thermoelectric generator
V	Fluid velocity (m/s)
V_{TEG}	Voltage generated by the TEG (V)
W_{ch}	Minichannel width (mm)
$\bar{x}$	Average location of the centerline thermocouples (mm)
x	Thermocouple location (mm)

Greek letters

α	Seebeck coefficient (V/K)
δR	Error in a calculated parameter
δx	Error in a measured parameter
β	Channel aspect ratio (H_{ch}/W_{ch})
ρ	Density (kg/m^3)
μ	Viscosity (N·s/m^2)
ε	Roughness (μm)
η_{fin}	Fin efficiency

Subscripts

avg	Average value
b	Bulk
ch	Channel
CL	Centre line
cond	Conduction
conv	Convection
FD	Fully developed
int	Interface
lam	Laminar
LM	Log-mean
s	surface
ss	Stainless steel
w	Water

1. Introduction

1.1. Waste Heat

Thermal energy is an essential element in our everyday life. Some applications include food preparation, providing warmth in cold weather, industrial processes and electricity generation. Common sources of thermal energy are fossil fuels, solar radiation, and nuclear fission. Considering the use of thermal energy in electrical power generation, it is estimated that in 2012, 35% of the total electrical energy generation in Canada was produced using thermal processes [1]. On a global scale, the total electricity generated in 2010 was 21 PWh, 80% of which was generated using various thermal processes [2].

The majority of the thermal energy generated worldwide comes from three main sources coal, natural gas, and nuclear fission. Depending on unsustainable fossil fuels as energy sources is problematic, as the greenhouse gases emitted are linked to climate change. Hence, sustainable energy sources such as wind, geothermal, solar, wave and tidal have been receiving more attention.

As society continues to depend on fossil fuels and conventional processes utilizing thermodynamic cycles for electrical energy generation, it is critical that the generation process is done in the most efficient manner possible. Thermodynamic cycles normally dissipate (i.e. waste) unused thermal energy to the surrounding environment. Recovering the wasted thermal energy is critical in order to maximize the input energy source utilization. Recent research efforts have been focused on storing low and medium grade waste thermal energy (i.e. waste heat) and using it for space or district heating [3]. Waste heat is an abundant resource and it can be harvested using existing technologies. For example, it is estimated that in the

United States alone, 35 GW (1050 TBtu/year) of waste heat, that has work potential, is wasted from the industrial and commercial infrastructure [4]. Likewise in Canada, it is estimated that 2300 PJ/year of waste heat is rejected from industrials processes such as oil refining, paper making, chemical and petrochemical processes. In fact, up to 400 PJ/year of that waste heat is recoverable using existing waste heat recovery technologies [5].

Waste heat is classified according to the media temperature to three main categories: high grade (T > 650 °C), medium grade (650 °C > T > 230 °C) and low grade (T < 230 °C) [6]. Once the waste energy is recouped it can be used for preheating processes, electrical power generation, and space heating/cooling. Technologies such as an organic Rankine cycle and thermoelectric generators (TEGs) can be used for generating electrical power using waste heat [7]. The focus of this investigation is on low grade waste heat Energy harvesting in this range of temperatures has received limited attention due to difficulties associated with generating electrical energy from the wasted heat.

1.2. Thermoelectric Generators

A Thermoelectric generator (TEG) is an appealing technology for implementation in waste heat recovery. TEGs are solid state devices that have the ability of directly converting heat into useful electricity. The main advantage of thermoelectric generators is that the heat required does not have to be high grade to be converted. Thus TEGs are an ideal option for low grade waste heat recovery applications. In addition, thermoelectric generators have no moving parts for converting the waste heat, which is advantageous because they can operate for long periods of time without requiring maintenance [8].

A thermoelectric generator is composed of P and N type semiconductors elements, connected electrically in series and thermally in parallel, inserted between two ceramic plates as illustrated in Figure 1.1. A temperature difference across the P an N elements induces a voltage difference needed to generate electrical power (this phenomenon is known as the Seebeck effect). In general, there are three main properties which represent the performance for a thermoelectric generator, which are the Seebeck coefficient (α), electrical resistance (R), and thermal conductivity (k). The three properties can be combined as the figure of merit, ZT $\left(ZT = \frac{\alpha^2 T}{k\,\mathrm{R}}\right)$ which reflects efficiency of the TEG module.

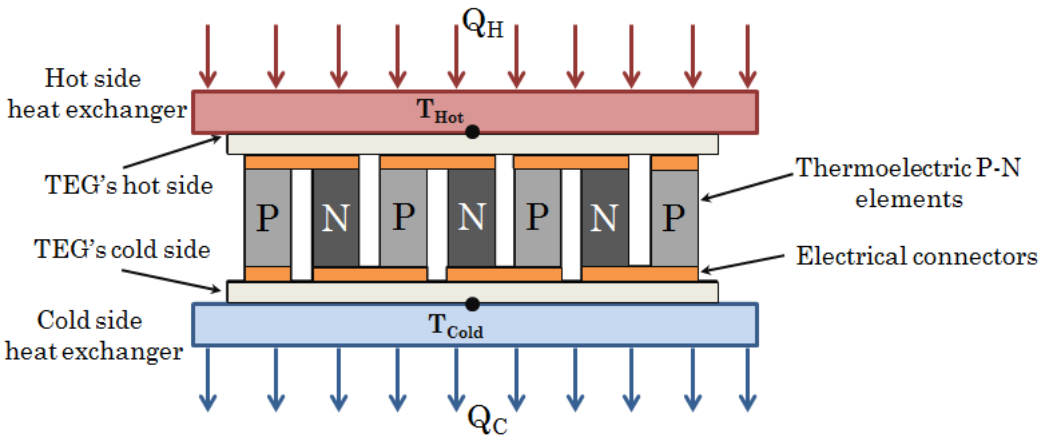

Figure 1.1. A schematic of a thermoelectric generator.

The magnitude of the voltage generated by a TEG (V_{TEG}) is proportional to the temperature difference between the hot and cold sides of the TEG and the Seebeck coefficient.

$$V_{TEG} = \alpha\,(T_{Hot} - T_{Cold}) \qquad (1.1)$$

The Seebeck coefficient of a particular TEG module is a function of the Seebeck coefficients of the thermoelectric materials that make the P and N elements. T_{Hot} and T_{Cold} are the temperature of the TEG's hot side and cold side, respectively. Equation 1.1 indicates that the electrical voltage generated

(V_{TEG}) increases as the temperature difference ($T_{Hot} - T_{Cold}$) increases assuming that the change in the Seebeck effect (α) (due to temperature dependence) is small and T_H is held constant.

The variation in the electrical power generated by a TEG (P_E) at the matched load condition as a function of T_{Cold} was experimentally studied by Finnerty [8] as part of the TEG POWER. The results are presented in Table 1.1. The TEG POWER system is discussed in Section 1.3.

Table 1.1. The variation in the electrical power generated by a TEG as a function of the cold side temperature ($\boldsymbol{T_{Cold}}$).

T_{Hot} (°C)	T_{Cold} (°C)	P_E (W)	Reduction in P_E
200	30	3.5	20%
200	50	2.8	
150	30	2.1	28%
150	50	1.5	

The experimental data indicated that for T_{Hot} = 150 °C, increasing T_{Cold} from 30 °C to 50 °C decreased the electrical power generated by the TEG by 28% at T_{Hot} = 150 °C, and by 20% at T_{Hot} = 200 °C. On average, it can be concluded that increasing T_{Cold} by 10 °C reduces the electrical power generated by the TEG by approximately 12% (1.2% per 1 °C).

For waste heat recovery systems multiple TEGs arranged in an array are used to generate a useful amount of electrical power. For multiple TEG modules arranged in an array and connected electrically in series, the total electrical power generated by the TEG array could be affected by the worst performing TEG (i.e. the weakest link). To illustrate this concept, consider three identical TEG modules connected electrically in series as depicted in Figure 1.2. In the first case, assume that all the TEGs have the same electrical resistance (R) of 2 Ω, and all the TEG generate the same voltage

(V_{TEG}) of 4 V. For these conditions, the electrical current passing through the TEG array (I) can be calculated using Ohm's law ($V = IR$) to be 2 Amp and the total electrical power generated would be 6 W (at the matched load condition). For the second case, assume that the voltage generated by each TEG (in Figure 1.2) is still 4 V; but TEG3 has higher electrical resistance of 4 Ω (while TEG1 and TEG2 both have R 2 Ω). For this case the electrical current generated would be 1.5 Amp, and the total power generated would be 4.5 W. Note how the second case has a lower total electrical power generated by the TEG array, which illustrates the effect of the worst performing TEG on the overall electrical power generated by a TEG array.

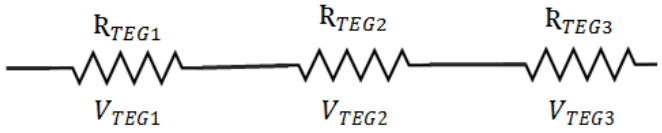

Figure 1.2. An electrical schematic of three TEG modules electrically connected in series.

Another important factor that can affect the electrical power generated by a TEG array is the temperature distribution of the hot side and cold side heat exchangers. It is critical that all the TEGs in the array are subjected to the same temperature at their hot and cold sides. A maldistribution in the surface temperature of the cold side heat exchanger, will affect the cold side temperature (T_{Cold}) of each TEG module in the array. This situation could locally affect the voltage output and the electrical resistance of each TEG in the array, and could negatively impact the total power generated by the TEG array. This concept will be discussed in Section 1.3.1 in more details.

1.3. The TEG POWER Project

The project presented in this thesis is a component of a larger research project at McMaster University known as the TEG POWER project, TEG POWER is an acronym for TEG Pizza Oven Waste Energy Recovery. The TEG POWER project is developed by the Thermal Management Research Laboratory (TMRL) in partnership with Pizza Pizza, Thermal Electronics Corp. and Acrolab who are interested in making Pizza Pizza stores more energy efficient. The main objective of the project is to harvest low grade waste heat from the exhaust gases of commercial pizza ovens, the typical exhaust gas temperature is around 200 °C – 270 °C. Part of the recovered wasted heat will be converted directly to electricity using thermoelectric generators, the rest will provide thermal energy to a restaurant's HVAC and water heating system. Other students are working on different aspects of the TEG POWER such as thermal energy storage system, hot side heat transfer system, characterization of thermoelectric generators, and restaurant energy system optimization. The TEG POWER system will provide Pizza Pizza restaurants with autonomous energy making them functional in case of a power outage. Moreover, the thermal energy that is not converted to electrical energy will be stored using a dedicated thermal storage system and subsequently used for potable hot water supply and restaurant heating requirements.

Figure 1.3 shows a simplified schematic diagram of the TEG POWER system and the corresponding thermal resistance diagram for the whole system. For continuous electrical power generation, a temperature gradient across the TEG must be maintained. To maintain such temperature gradient, a hot side heat exchanger must be used to supply thermal energy (Q_H) to the TEG's hot side. Furthermore, a cold side heat exchanger must be used to remove thermal energy (Q_C) from the TEG's cold side. Each component has its

own thermal resistance which is a function of the flow conditions and the heat exchanger design. Effective hot side and cold side heat exchanger design (i.e. low thermal resistance) allows for high temperature gradient to develop across the TEGs and therefore increases the total electrical power generated by the system. This project will focus on the design of the cold side heat exchanger for the TEG POWER system.

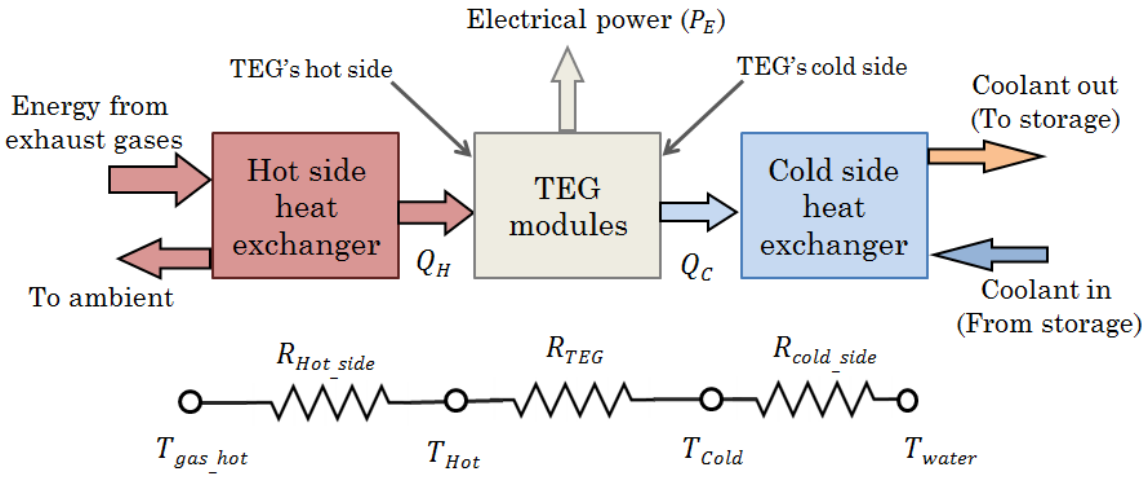

Figure 1.3. A simplified schematic of the TEG POWER setup illustrating the different components and the corresponding thermal resistance diagram.

1.3.1. Design Parameters and Constraints for the Cold Side Heat Exchanger

For designing the cold side heat exchanger, there are few design parameters and constraints that must be considered carefully, these design parameters and constraints are discussed below.

- **Heat transfer requirements**

  The TEG POWER system utilizes 48 TEGs per assembly to generate usable electrical energy. The total electrical power generated from the 48 TEGs is approximately 110 W at an oven set temperature of 315 °C (600 °F). To generate 110 W, 4 kW of thermal energy must be recouped from

the exhaust gases stream. Given that the TEG POWER system utilizes 48 TEG modules, 40 mm × 40 mm, the heat flux that must be dissipated per TEG module is calculated to be 52.1 kW/m^2. In addition, the heat exchanger must be able to effectively transport the thermal energy gained to a dedicated thermal storage system as depicted in Figure 1.3.

- **Pressure drop constraints**

The allowable parasitic losses, due to the pumping power required for the cold side prototype was limited by design to 10 W. The remaining electrical power generated by the TEG POWER system is to be utilized for other restaurant requirements. For any heat exchanger design, the pumping power is a function of the mass flow rate flow through the heat exchanger and the pressure drop across it.

- **Heat exchanger size and TEG arrangement**

The exhaust duct of the pizza oven is 610 mm (24 in) wide. Therefore the full scale cold side heat exchanger prototypes must be at least 160 mm and be able to cool 24 TEG modules simultaneously. However, testing such the full scale heat exchanger requires the construction of a large scale experimental facility which can be an expensive option. Therefore, it was proposed to build "smaller" cold side heat exchanger prototypes and test them using a dedicated experimental facility. The heat exchanger prototypes would have an identical design as the full scale heat exchangers. The size of the heat exchange prototypes was chosen to be nearly half the size of the full scale heat exchanger and capable of accommodating 14 TEG (instead of 24 TEGs) modules simultaneously. In essence, the cold side heat exchanger prototypes will have the same design as the full scale cold side heat exchanger, the only difference will in the heat exchanger length. The designed heat exchanger prototypes will

be about half the length of the full scale heat exchanger required for the TEG POWER system.

Figure 1.4 depicted a possible installation arrangement of a TEG array with a cold side heat exchanger. Typically, the TEGs are electrically wired in series, as seen in Figure 1.4, in order to generate a useful amount of voltage.

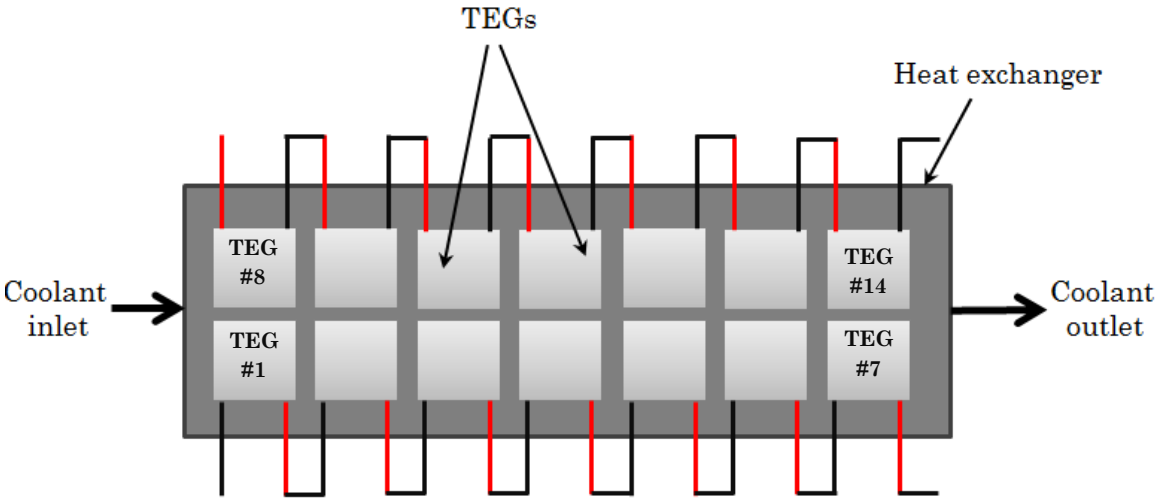

Figure 1.4. An illustration of the proposed TEG arrangement on the top surface of flat-plate cold side heat exchanger (top view).

- **Uniform heat exchanger surface temperature distribution**

The heat exchanger surface temperature will directly affect the temperature of the TEG's cold side (T_{Cold}). A maldistribution in the heat exchanger surface temperature will result in differences in the cold side temperatures of the TEGs. For example, if the heat exchanger depicted in Figure 1.4 had a surface temperature or coolant flow maldistribution, the cold side temperatures of TEG #1 and TEG #7 will be different. As a result the electrical power generated by TEG #1 will be different compared to TEG #10 assuming that the hot side of all TEGs is kept at the same temperature. As calculated in Section 1.2, if the cold side heat exchanger

surface has a temperature maldistribution of 10 °C, the power generated by the TEGs could decrease by approximately 12%.

- **Flat heat transfer surface**

As shown in Figure 1.5, heat is transferred from the TEG's cold side to the heat exchanger via conduction. Therefore, having a flat heat exchanger surface is crucial so that good contact is established between the TEG and the heat exchanger surface. A non-flat heat exchanger surface can lead to the formation of air gaps between the TEG and the heat exchanger surface. The presence of air gaps will increase T_{Cold} which will cause a reduction the electrical power generated by the TEG. Figure 1.5 shows the formation of an air gap under a TEG when there is a notable "low spot" in the heat exchanger surface. It is recommended that the heat transfer surface of the cold side heat exchanger be machined using a fly-cutting operation in order to obtain a flat heat transfer surface. Typical tolerances associated with fly-cutting operations range from 0.02 mm to 0.1 mm. A thin layer of thermal interface material (thermal paste) must be added, between the heat transfer plate and the cold side surface of the TEGs, in order to fill any air gaps and reduce the contact resistance between the dissimilar surfaces.

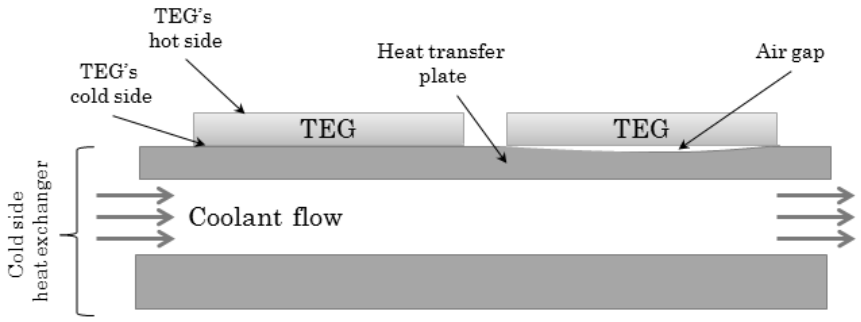

Figure 1.5. Air gap formation due to the heat transfer plate being not perfectly flat.

- **Heat exchanger materials and corrosion prevention**

The cold side heat exchangers should fabricated using aluminum because of its good thermal properties, cost effectiveness and the ease of machining. For implementation in the TEG POWER system, a mixture of water and glycol (4:1 ratio) will be used as the working fluid for the system as opposed to pure water. Using water/ propylene glycol mixture will retard the corrosion and scale buildup on the wetted surfaces inside the cold side heat exchanger. A water/propylene glycol mixture is nonpoisonous and therefore it can be safely implemented in waste heat recovery applications catered for the food industry.

1.4. Motivation

Waste heat recovery systems using thermoelectric generators are affected by the conversion efficiency of the thermoelectric generators and the design of the hot side and the colds side heat exchangers. Effective heat exchanger design can improve the efficiency of the waste heat recovery system [9].

Limited research has been conducted regarding the integration of flat-plate heat exchanger with thermoelectric generators [10] used for waste heat recovery systems. Therefore there is a need for more research work in this field. The goal for this research work is to determine the appropriate flat-plate cold side heat exchanger design for implementation in the TEG POWER system.

1.5. Research Objectives

The following research objectives were developed in order to achieve the goals of the project,

- Review the possible cooling techniques for designing the cold side heat exchanger prototypes and select cooling techniques that are well suited for the TEG POWER system.

- Design and fabricate flat-plate exchanger prototypes capable of accommodating an array of TEGs simultaneously based on the selected cooling technologies.
- Design, built and characterize an experimental facility capable of performing heat transfer and pressure drop tests for flat-shaped heat exchangers.
- Use the experimental facility to characterize the thermal and hydrodynamic performance of the designed heat exchanger prototypes.
- Compare the thermal and hydrodynamic performance of the heat exchanger prototypes to determine the most suitable heat exchanger design for implementation in the TEG POWER system.

1.6. Scope of Work

This thesis is comprised of to six chapters. Chapter one is a thesis introduction that discusses the abundance of waste heat, the TEG POWER system and the motivation for the current research work. In chapter two, common cooling technologies used for similar heat transfer processes, such as cooling electrical components, are presented and discussed. The chapter also contains a literature review regarding fluid flow and heat transfer in minichannels and submerged impinging jets. Chapter three discusses the design of the heat exchanger prototypes proposed for implementation in the TEG POWER system.

A detailed design of the experimental facility used for testing the heat exchanger prototypes is discussed in chapter four. The chapter also contains data reduction steps, experimental procedure and uncertainty analysis for the experimental data obtained. In chapter five, the experimental heat transfer and pressure drop, for both exchanger prototypes, are presented,

discussed, and compared to correlations. Chapter six contains research conclusions and recommendations for future work.

2. Literature Review

Limited studies are available regarding the heat transfer techniques suitable for cooling TEG modules. Thus, the literature review will focus on the common cooling techniques used for dissipating the thermal energy generated by electrical systems and components. The commonly used cooling techniques will be evaluated to determine the suitable cooling techniques for designing the cold side heat exchanger to be implemented in the TEG POWER system.

2.1. Common Cooling Techniques Utilized for Cooling Electronic Components

Almost all electrical components require a heat transfer system to operate safely and efficiently. The objective of the heat transfer system is to dissipate the unwanted thermal energy generated by a component such that its working temperature remains within a predetermined safe operating limit (i.e. provide cooling effect). For example, external fins are typically added to the outer casing of some electrical motors in order to dissipate the thermal energy generated inside the motor. Failing to properly dissipate the undesired thermal energy leads to excessive increase of the component temperature which in turn leads to premature failure.

Heat exchangers designed for dissipating the thermal energy from electrical components, usually employ single-phase or two-phase heat transfer techniques (also called cooling techniques). A detailed review of the common cooling techniques used for electronic components can be found in [11, 12]. The selection of an appropriate cooling technique depends on the amount of heat dissipation required, maximum allowable component temperature, component geometry/shape and its physical size. A discussion

regarding the applicability of each cooling technique for the TEG POWER system is provided below.

Two-phase cooling techniques can be classified as passive or forced. Passive two-phase cooling techniques include heat pipes, while forced two-phase cooling techniques (specifically designed for electronic cooling) include two-phase forced convection in minichannels and microchannels. Two phase cooling techniques are typically used for dissipating high heat fluxes of approximately 500 kW/m^2 [12] and above. For the TEG POWER system the applied heat flux is between 50 – 60 kW/m^2 per TEG. The applied heat flux is relatively low compared to the heat flux dissipation capabilities of two-phase systems. Due to design complexities associated with two-phase cooling systems and the relatively low applied heat flux heat flux (50 – 60 kW/m^2 per TEG) passive and forced two-phase cooling techniques were not selected for designing the cold side heat exchanger utilized in TEG POWER system.

Heat transfer systems utilizing single-phase cooling techniques normally employ air or liquids as the working fluids. Extended fin heat sinks integrated with an electrical fan is an example of a single-phase cooling technique that employs air as the working fluid. Air based single-phase cooling techniques are typically used for low thermal energy dissipation requirements. Furthermore, air has low heat capacity and low thermal conductivity. The thermal properties of air render it an unfavorable choice of working fluid for thermal load management systems thermally linked to heat energy storage systems. Due to their inadequate heat transfer capabilities, air based cooling techniques were not chosen for designing the cold side heat exchanger implemented in the TEG POWER system.

Single-phase forced convection using liquids is the most appropriate cooling technique for designing the cold side heat exchanger implemented in the TEG POWER system. Liquids have better thermal conductivity and

specific heat capacity compared to air. Therefore liquid based forced convection systems are capable of dissipating higher heat fluxes compared to air based forced convection systems. In addition, because of the improved thermal properties of liquids over air, liquid based heat exchangers are capable of effectively transporting the harvested thermal energy to a thermal storage system, which is one of the requirements for TEG POWER cold side heat exchanger.

For designing the cold side heat exchanger, the two promising forced convection single-phase cooling strategies are liquid based forced convection through channels and liquid jet impingement. These cooling strategies are well established and they have been successfully used for designing compact closed loop cooling systems for electrical components. Examples of electronics cooling systems utilizing forced convection in miniature channels and single impinging jet can be found in [13, 14]. Both cooling strategies are discussed below in more details.

2.1.1. Single-Phase Forced Convection in Channels

The thermal and hydrodynamic performance of single-phase forced convection of liquids through channels is well studied in the literature. For internal fluid flow inside channels, Kandlikar and Grande [15] proposed the following channel classification[1] which is based on flow considerations inside the channel,

- Conventional size channels: $D_h > 3$ mm.
- Minichannels: 3 mm $\geq D_h >$ 200 μm.
- Microchannels: 200 μm $\geq D_h >$ 10 μm.
- Transitional channels: 10 μm $\geq D_h >$ 0.1 μm

[1] It should be mentioned that the channel classification proposed by Kandlikar and Grande is not always followed by researchers. Often confusions are created due to inappropriate use of the term "microchannel".

- Molecular nanochannels: 0.1 μm ≥ D_h

Forced convection in enclosed channels is commonly used for designing flat-plate heat exchangers. The idea is to fabricate channels on one side of a substrate material and apply thermal loads on the other side. The thermal energy applied to the heat exchanger will be dissipated by the coolant flowing inside the channels. Figure 2.1 is a schematic showing the utilization of forced convection in channels technique in heat exchanger design.

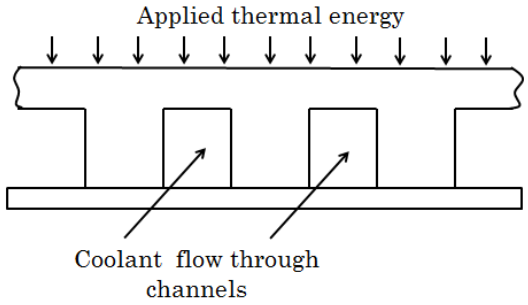

Figure 2.1. A concept diagram illustrating the utilization of forced convection inside channels as a heat removal technique.

Single-phase forced convection through microchannels offers large heat transfer area and high convection heat transfer coefficients because of the small channel hydraulic diameter (D_h). However, large pressure head is required to drive the flow through the microchannels [16]. Conversely, forced convection through conventional size channels does not yield very high heat transfer coefficients but the pressure drop required is typically lower when compared to microchannels [16]. Alternatively, single-phase forced convection though minichannels offers good heat transfer performance while requiring moderate pressure drop [16]. In general, flow through minichannels has the advantage of demanding lower pressure head compared to flow through microchannels. Another advantage of minichannels is the ease of machining. As indicated above minichannels have larger hydraulic diameters compared to microchannels, therefore conventional precision machining operations can

be utilized for minichannels fabrication. Fabricating microchannels requires complex fabrication processes such as wet chemical etching [15]. In conclusion, minichannels offer good combination of pressure drop and heat transfer and they can be machined easily using conventional machining methods. Due to their appealing design features, minichannels were selected for fabricating one cold side heat exchanger prototype, this prototypes is called the 'minichannels heat exchanger' prototype.

A possible method to increase the heat transfer performance for single-phase internal flow is to use utilize curved channels instead of straight channels. In the laminar flow regime, curved channels induce secondary rotational flow, known as the Dean vortices, inside the channel [17]. The secondary flow generated induces mixing which improves the heat transfer performance [18]. The fluid flow and heat transfer in wavy (i.e. curved) rectangular microchannels (depicted in Figure 2.2) was numerically studied by Sui et al. [18]. The authors concluded that wavy microchannels offer significant heat transfer enhancement with smaller pressure drop penalty compared to straight microchannels.

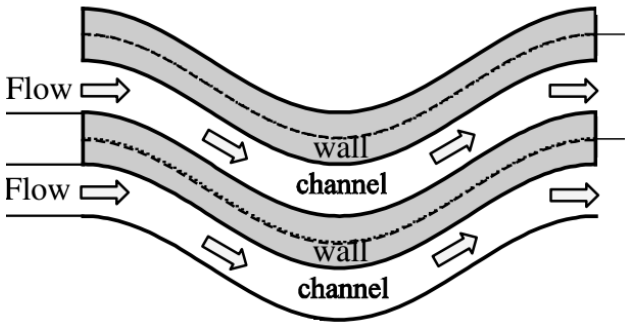

Figure 2.2. A schematic depicting curved (wavy) microchannels (from [18]).

The benefit of utilizing curved minichannels instead of straight minichannels was investigated in order to improve the heat transfer

performance of the minichannels heat exchanger. However, manufacturing the curved channels with conventional machining techniques was difficult and time consuming process. Typically, such miniature channels are fabricated using high speed micromachining [19] techniques which can be difficult to implement. Due to the fabrication difficulties associated with machining the curves minichannels, straight minichannels were selected for designing the cold side heat exchanger.

Besides utilizing curved channels to improve the heat transfer performance, convectional heat transfer enhancement methods were also explored in order to improve the heat transfer performance of the minichannels heat exchanger. Examples of conventional heat transfer enhancement methods include extended surfaces, roughened surfaces, twisted tapes and turbulators. Figure 2.3 illustrates few conventional heat transfer enchantment options.

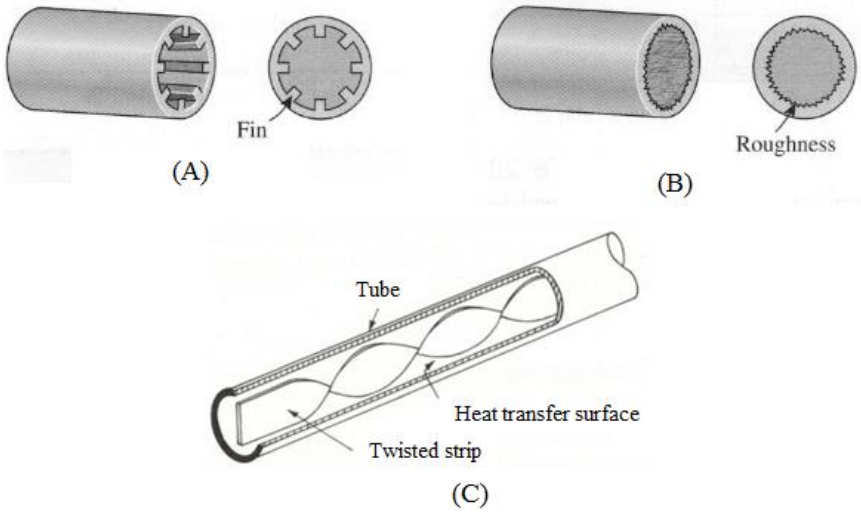

Figure 2.3. Selected heat transfer enhancement methods, (A) internal finned surfaces, (B) roughened surfaces (A and B from [20]) and (C) swirl tape insert (from [21]).

The conventional heat transfer enhancement methods seen in Figure 2.3 are passive heat enhancement since they cannot be controlled once they are implemented inside a heat exchanger. In general, convectional enhancement methods are designed to increase the thermal conductance (hA). Conventional heat transfer enhancement methods are known to increase the heat transfer. However, implementation of such enhancement methods also leads to an increase in the friction factor; which eventually increases in the pressure drop required for operation. In some cases, adding turbulators increased the heat transfer performance by about 200%. However the increase in friction factors was higher compared to the enhancement of heat transfer [22]. Typically conventional heat enhancement methods are designed to improve the heat transfer performance of conventional size tubes and channels. They are not well suited for implementation in minichannels due to the small hydraulic diameter of the minichannels.

To conclude, conventional heat transfer enhancement methods are capable of improving the thermal performance of a heat exchanger. However, due to the undesired increase in pressure drop and implementation complexity, conventional heat transfer enhancement techniques were not utilized in the design of the minichannels cold side heat exchanger

2.1.2. Single-Phase Liquid Jet Impingement

Single-phase liquid impinging jets is another forced convection strategy which can be used for making another cold side heat exchanger prototype. Typically, impinging jets heat exchanger designs require the following: a flat plate and single or multiple cooling jets. The flat plate can be positioned above or below the impinging jets depending on the heat exchange design. The impinging jets remove thermal energy from the heated surface upon their impingement on the heated surface. A simple conceptual heat exchanger diagram utilizing single jet is depicted in Figure 2.4.

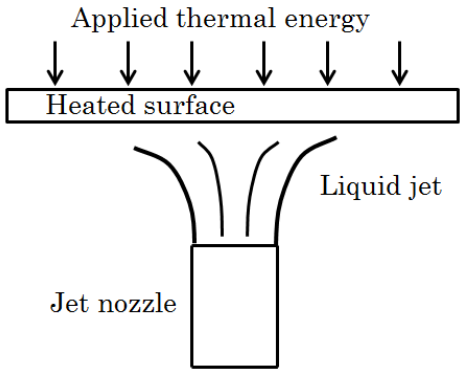

Figure 2.4. A schematic illustrating the idea of using jet impingement for heat removal.

Impinging jets offer very high heat transfer coefficients and good temperature uniformity when the jets are arranged in arrays [23]. In addition, the impinging jets can be strategically positioned to target specific locations where high heat transfer rates are required (i.e. localized cooling). Impinging jets are usually used for cooling devices that dissipate high heat fluxes such as lasers [12]. Typically, the impinging jet thermally interacts with a flat-plate heated surface. Therefore the heat transfer area of the impinging jets is smaller when compared to the heat transfer area of minichannels and microchannels.

Impinging jets can be divided into three main categories submerged jet (liquid jet surrounded by liquid media), free jets (liquid jet surrounded by vapour or gaseous media) [24] and confined jets (jets are confined between a nozzle and a heated wall) [12]. For similar operating conditions, submerged jets performed equally or better compared to free jets [25]. In addition to their thermal performance, submerged jets are well suited for designing enclosed heat exchangers. Therefore submerged liquid jets were selected for designing an additional cold side heat exchanger prototype (called the impinging jets heat exchanger). Free jets are normally used for “open spraying” processes

such as metal quenching and are not applicable for the current design configuration.

To summarize, numerous cooling techniques are available for cooling electrical components, the selection of a cooling technique depends on various factors such as the shape and physical size of the component being cooled. Upon the review of the common cooling techniques, single-phase forced convection of liquids was the most appropriate cooling technique for designing the cold side heat exchanger prototypes for the TEG POWER project. Two cooling strategies were selected for designing the cold side heat exchanger prototypes. The first heat exchanger prototype utilizes single-phase forced convection in straight minichannels, while the second heat exchanger prototype employs submerged liquid jets impinging on a flat-plate.

A literature review regarding the fluid flow and heat transfer in minichannels and submerged impinging jets is presented in the next section.

2.2. Heat Transfer and Pressure Drop in Minichannels and Microchannels Heat Exchangers

This section contains literature review studies regarding fluid flow and heat transfer in rectangular-shaped minichannels and microchannels. Relevant fluid flow and heat transfer correlations are also presented and discussed.

The idea of using compact microchannels for high heat flux removal from electronic components was first introduced in 1981 by Tuckerman and Pease [26]. Since then extensive research has been devoted to study the field of minichannel and microchannel cooling. Comprehensive review papers regarding fluid flow and heat transfer in minichannels and microchannels are presented by several researchers [27 – 33]. Various channel shapes and sizes were studied using different working fluids. Studies relevant to this work were selected and reviewed below.

Table 2.1 contains a summary of 12 studies regarding single-phase fluid flow and heat transfer in minichannels and microchannels. The study results are compared to conventional heat transfer and fluid flow correlations. For all studies reviewed in Table 2.1, water was used as the working fluid. In addition, the selected studies are for rectangular channel geometry unless specified under the 'Notes' section.

Table 2.1. Review of selected studies regarding fluid flow and heat transfer in minichannels and microchannels.

Study by	D_h (μm)	Number of channels	Channel material	Re range	Nu	f	Transition Re	Notes
Wang and Peng [34]	311-747	4 and 6	stainless steel	80 -3500	↓↓	Not studied	Fully turbulent regime at Re 1000 - 1500	Water and methanol. Different microchannel configuration tested
Peng and Peterson [35]	133-367	Different for each substrate	stainless steel	85 -4000	↓↓	↓↓	Critical Re function of substrate geometry	12 different substrates tested
Harms et al. [36]	1923, 404	1 and 68	silicon	173 - 12900	≈	≈	1500	
Mokrani et al. [37]	100 - 1000	1	stainless steel	100 - 5000	≈	≈	2200 - 3000	large aspect ratio channels
Rahman [38]	299 - 491	12 for the straight channel	silicon	250 - 4000	↑↑	Frictional losses not presented as friction factors	No clear transition observed	Straight and U-shaped channels with various configurations tested

Table 2.1. (continued)

Study by	D_h (μm)	Number of channels	Channel material	Re range	Nu	f	Transition Re	Notes
Qu and Mudawar [39]	349	21	Oxygen-free copper	139 - 1672	≈	≈	Early transition not observed	Experimental and numerical study
Xu et al. [40]	29.59-344.3	Different for each substrate	aluminum and silicon	20 -4000	Not studied	≈	1500	12 different substrates tested
Mirmanto et al. [41]	438-635	1	copper	150 - 6000	↑↑	≈	1000 - 2000	
Park and Punch [42]	106 - 307	16-100	silicon	69 -800	Data did not agree with conventional correlations	≈	Laminar flow regime	
Cany et al. [43]	1000	1	aluminum	310 - 7780	Not compared	≈	2500	Square channels

Table 2.1. (continued)

Study by	D_h (μm)	Number of channels	Channel material	Re range	Nu	f	Transition Re	Notes
Lee et al. [44]	318 - 903	10	copper	300 - 3500	Noticeable deviations observed	Not studied	1500 - 200	Experimental Nu agreed well with numerical simulations conducted by the authors
Pfund et al. [45]	D_h not repor-ted	1	channel formed between polycarb-onate and polyimide	60 -3450	Not studied	↑↑	Critical Re affected by channel depth ~ 1700 - 2800	Smooth and rough channels relative roughness =3%. H_c =128 - 521 μm. High aspect ratio channels.

↑↑- Values higher than convectional correlations.

↓↓- Values lower than convectional correlations.

≈- Values agree with convectional correlations.

Harms et al. [36] conducted experiments to study single-phase convective heat transfer in deep rectangular microchannels fabricated in a 25 mm × 25 mm silicon substrate. Two microchannel configurations were tested. The first configuration had a single microchannel 25 mm wide × 1 mm deep (D_h= 1.923 mm), the second configuration utilized 68 microchannels 0.251 mm wide and 1.030 mm deep (D_h= 0.404 mm). The channel Reynolds number ranged from 173 to 12900. Results indicated that the thermal resistance of the multiple microchannels configuration was approximately 45% lower compared to the single microchannel configuration. However, local Nusselt numbers for a single microchannel was higher than the local Nusselt numbers for multiple microchannels. At high Reynolds number, good agreement was found between the experimental results and the local Nusselt numbers obtained using conventional flow correlations but for lower Reynolds values the agreement deteriorated. This behavior was attributed to the manifold design, which was also deemed responsible for the early transition to from laminar flow conditions which occurred at Re = 1500.

Qu and Mudawar [39] conducted an experimental and numerical investigation to study single-phase pressure drop and heat transfer in a microchannel heat sink. Twenty one rectangular microchannels 0.231 mm wide × 0.731 mm deep (D_h = 0.351 mm) and 44.8 mm long were machined in a copper substrate. Experimental heat transfer and pressure drop results were in a good agreement with numerical results obtained using Navier-Stokes and energy equations. However, their experimental data were not compared to conventional heat transfer and pressure drop correlations. Early transition from laminar flow conditions inside the microchannels was not observed for the tested Reynolds numbers which were between 139 – 1692.

Lee et al. [33] studied single-phase heat transfer in microchannels experimentally and numerically. Ten microchannels were machined on a 25.4

mm × 24.4 mm × 70 mm copper substrate. The microchannels width ranged from 0.194 mm to 0.534 mm. The microchannel depth was nominally five times the microchannel width. Reynolds numbers were in the range of 300 – 3500 which allowed for either simultaneously developing, or hydrodynamically developed thermally developing flow conditions in the microchannels. Experimental results indicated that the transition from laminar to turbulent flow conditions occurred at Reynolds numbers of 1500 – 2000. Significant deviations were observed between the experimentally obtained Nusselt numbers and the Nusselt numbers calculated using convectional flow correlations. The authors proposed that the deviations observed were due to boundary and inlet conditions mismatch between the convectional correlations and those of the test section. However, numerical simulations based on the Navier-Stokes equations were found to be in good agreement with experimental results which seems to confirm the conclusions of Qu and Mudawar [39]. The authors concluded that Navier-Stokes can predict the performance of microchannels if the effects of the boundary and inlet conditions are carefully accounted for.

Shen et al. [46] conducted experiments to study single-phase convective heat transfer and fluid flow in microchannels. The heat exchanger was made from copper (50 mm × 15.3 mm) on which 26 rectangular microchannels 0.3 mm wide × 0.8 mm deep (D_h = 0.43 mm) were fabricated. The microchannel's length was 50 mm long, and the relative roughness was between 4-6%. Tested Reynolds numbers varied from 152 to 1257 and were in the laminar regime. Heat transfer results showed that the local and average Nusselt numbers were lower than local and average Nusselt numbers predicted by conventional correlations. The authors proposed that the deviations in the heat transfer results are attributed to the cross sectional area and surface roughness effects on the 'near wall velocity'. However,

surface roughness does not typically affect the heat transfer in the laminar regime. In fact, if roughness did actually affect the heat transfer in laminar flow, it would tend to increase in heat transfer instead of decreasing it. The transition from laminar flow was not reported in this testing range.

Peng and Peterson [47] experimentally studied fluid flow and heat transfer in twelve different microchannels configurations machined on stainless steel substrate with microchannel's D_h = 0.133 – 0.367 mm. Tested Reynolds numbers were between 50 – 4000. Results showed that a microchannels' geometric configuration, such as aspect ratio and hydraulic diameter to centre to centre spacing, affected the convective heat transfer and fluid flow behavior. The authors proposed correlations for predicting Nusselt number for microchannels in the laminar the turbulent flow regimes.

Regarding pressure drop in microchannels, Park and Punch [48] studied the thermal and hydrodynamic behavior of microchannels having 0.106 mm < D_h < 0.307 mm. The tested Reynolds numbers were between 69 to 800. The experimentally obtained friction factors agree well with the theoretical friction factor calculated using convectional flow correlations. The authors highlighted the importance of including manifold effects for accurate evaluation of microchannel's pressure drop and friction factor. Laminar and turbulent friction factors (for the multiple channel system) measured by Harms et al. [36] friction factors results were also in good agreement with conventional friction factors correlation. Caney et al. [49] measured the friction factors for a single minichannel 1 mm wide × 1 mm deep × 420 mm long, Reynolds numbers were in the rage of 310 to 7780. The experimentally obtained friction factors agreed well with conventional channel correlations.

Pfund et al. [50] experimentally measured the measured the friction factors for water flowing in smooth and rough (ε/D_h=3%) high aspect ratio rectangular microchannels with depth from 0.128 mm to 521 mm. Tested

Reynolds number were in the range of 60 – 3450. Results indicated that the transition from laminar flow conditions occurred at Reynolds number of 2500, which is about the same for conventional size tubes which is 2300 [51]. Moreover, it was found that laminar friction factors were higher than what is predicted by conventional theory especially for the rough microchannels.

Jiang et al. [52] experimentally measured the friction factors for a microchannel heat exchanger. The channels were rectangular and had a hydraulic diameter of 0.300 mm, the relative microchannel roughness was 0.1%. The experimentally measured friction factors were larger than the values predicted by conventional theory. The discrepancy was attributed to the effects of the hydrodynamic entrance region present in the test section.

In conclusion, experimental and numerical studies are available in the literature regarding single-phase fluid flow and heat transfer in minichannels and microchannels. However, these studies often lead to contradicting conclusions regarding the thermal and hydrodynamic behavior. Heat transfer results for minichannels and microchannels show a mixed agreement with conventional correlations. Factors such as channel geometry, development length effects, wall roughness, inlet manifold configuration, control of boundary conditions and conjugate effects are presumed to be responsible for the discrepancies and deviations observed in the literature [53].

2.2.1. Suggested Correlations for Determining the Heat Transfer and Pressure Drop in Minichannels and Microchannels

There is no clear evidence suggesting that the heat transfer in minichannels and microchannels is different from convectional channel flow heat transfer. Therefore, the heat transfer and pressure drop results of minichannels and microchannels are often compared to conventional heat transfer and pressure drop correlations [28, 33].

Internal fluid flow regimes in closed channels and tubes can be classified based on the thermal and hydrodynamic entry lengths. For laminar flow, the hydrodynamic (L_{hy}) and the thermal (L_{th}) entry lengths are given by, (adapted from [51])

$$L_{hy} \approx 0.05 Re_D D \tag{2.1}$$

$$L_{th} \approx 0.05 Re_D Pr D \tag{2.2}$$

Depending on the tube or channel length the flow can be thermally and hydrodynamically developing (i.e. simultaneously developing), developing (thermally or hydrodynamically), or fully developed thermally and hydrodynamically.

For thermally developing hydrodynamically developed flow in circular tubes flow under constant surface temperature boundary condition, Hausen proposed the following correlation for predicting the average Nusselt number in circular tubes (adapted from [54]).

$$Nu = 3.66 + \frac{0.0668(D/L)Re_D Pr}{1 + 0.04[(D/L)Re_D Pr]^{2/3}} \tag{2.3}$$

where D and L are the tube diameter and length respectively. The Hausen equation is also valid for simultaneously developing flow if $Pr \gtrsim 5$. The first term in Eqn. 2.3 is 3.66, which is the Nusselt number for fully developed flow in circular tubes under constant surface temperature boundary condition.

For laminar flow with simultaneously developing flow conditions; Sieder and Tate proposed (adapted from [54]) the following correlation for predicting the heat transfer in circular tube under constant surface temperature boundary condition.

$$Nu = 1.86 + \left(\frac{Re_D Pr}{L/D_h}\right)^{1/3} \left(\frac{\mu_b}{\mu_{wall}}\right)^{0.14} \tag{2.4}$$

The Sieder and Tate correlation is valid for $0.0044 \lesssim \left(\frac{\mu_b}{\mu_{wall}}\right)^{0.14} \lesssim 9.75$ and $0.6 \lesssim Pr \lesssim 5$. All properties are evaluated at the average temperature except

for μ_{wall} which evaluated at the wall temperature. The correlation of Hausen and Sieder and Tate are recommended for use in the simultaneously developing regime in order to account for hydrodynamic entrance effects and fluid property variation [55].

In the turbulent flow regime, the experimental data are typically compared to the second Petukhov equation [56]

$$Nu_D = \frac{(f/8)RePr}{1.07 + 12.7(f/8)^{1/2}(Pr^{2/3} - 1)} \tag{2.5}$$

valid for $2 \leq Pr \leq 2000$ and $10^4 \leq Re \leq 5 \times 10^6$. The Petukhov correlation was modified by Gnielinski to improve its accuracy for lower Reynolds numbers. Experimental Nusselt numbers for minichannels and microchannels in the turbulent flow regimes are also compared to Gnielinski's correlation [57]

$$Nu_D = \frac{(f/8)(Re_D - 1000)Pr}{1 + 12.7(f/8)^{1/2}(Pr^{2/3} - 1)} \tag{2.6}$$

The correlation is applicable for smooth tubes for both uniform temperature and heat flux boundary conditions. The correlation is valid for $0.5 \leq Pr \leq 2000$ and $3000 < Re < 5 \times 10^6$.

The term f, in Eqn. 2.5 and Eqn. 2.6, is the friction factor for smooth tubes in the turbulent regime. Its value is given by the first Petukhov [56] which is valid for $3000 < Re < 5 \times 10^6$.

$$f = (0.79 \ln Re - 1.64)^{-2} \tag{2.7}$$

The pressure drop for internal flows in channels is a function of the friction factor. The total pressure drop due to wall friction can be calculated using the following equation,

$$\Delta P_{friction} = f \frac{L}{D_h} \frac{\rho V^2}{2} \tag{2.8}$$

where f is the Darcy friction factor. In the laminar regime, the friction factor is dependent on the channels geometry. For a square channel ($\beta = 1$) and a

round tube the friction factors are given by the equations below (taken from [51]).

$$f = \frac{56.92}{Re} \tag{2.9}$$

$$f = \frac{64}{Re} \tag{2.10}$$

For the simultaneously developing regime inside channels, the apparent friction factor, f_{app}, should be used because it combined the effects of wall shear and the pressure drop associated with the developing velocity profile. Shah [58] proposed the following correlation for calculating the apparent fanning friction factor (f_{app}^*). f_{app}^* is the mean value of the apparent friction factor averaged over the channel length.

$$f_{app}^* = \frac{3.44}{Re\sqrt{L^*}} + \frac{(f_{FD}^* Re) + \frac{K(\infty)}{4L^*} - \frac{3.44}{\sqrt{L^*}}}{Re\left(1 + \frac{C}{L^{*2}}\right)} \tag{2.11}$$

where L^*=(L_{ch}/ReD_h) is a dimensionless channels length. The constant C in Eqn. 2.11 is dependent on the channel's aspect ratio β. The values of C for different channel aspect ratios can be found in Shah [58]. $K(\infty)$ is the fully developed Hagenbach factor and it is given by the following equation [59].

$$K(\infty) = 0.6611 + 1.1182\beta + 2.1758\beta^2 - 5.8322\beta^3 + 4.4683\beta^4 - 1.553\beta^5 \tag{2.12}$$

In this study, the Darcy friction factors will be used to describe the frictional losses in the channels. The Darcy friction factor f_{app} is equal to $4 \times f_{app}^*$.

The turbulent flow regime friction factors can be obtained using the Moody diagram. Alternatively, Blasius equation (presented in [60]), given by equation 2.13, can be used for determining the turbulent friction factors for $Re \leq 10^5$.

$$f = \frac{0.316}{Re^{0.25}} \tag{2.13}$$

2.3. Thermal and Hydrodynamic Behavior of a Axisymmetric Single Submerged Impinging Jets

This section contains literature review regarding the thermal and hydrodynamic performance of single-phase, axisymmetric submerged jet. The term axisymmetric refers to a jet emerging from a circular geometry jet nozzle as opposed to any other nozzle geometries.

2.3.1. Hydrodynamics and Flow Regions of a Single Jet

The following geometrical parameters are usually used to describe the impinging jet configuration. The jet-to-target spacing is the distance between the jet nozzle and the heated plate and it is given by H/D_j. The nozzle aspect ratio is defined as the length of the jet plate divided by the jet diameters, l/D_j. The distance away from the stagnation point is typically described in a dimensionless form r/d, where r is the local distance from the jet's stagnation point and d is a characteristic length of the impingement plate. The jet's Reynolds number (Re) is calculated using jet diameter (D_j) as the characteristic length.

An impinging jet is typically discharged from a nozzle onto a heated wall. In submerged jet impingement, the jet discharges into a fluid that is often the same as the jet itself. For a single jet impinging downwards on a heated surface, there are four main flow regions that characterize the jet flow. These flow regions are illustrated in Figure 2.5.

As the liquid jet emerges from the jet nozzle its outer fluid layer starts to interact with the surrounding fluid. The outer jet layer is known as the mixing region. In the potential core region, the fluid velocity at the centre of the impinging jet remains undisturbed for some distance below the jet outlet. Reynolds number is known to have a strong effect of the length of the potential core [25]. In the deflection region, the jet slows down and deflects

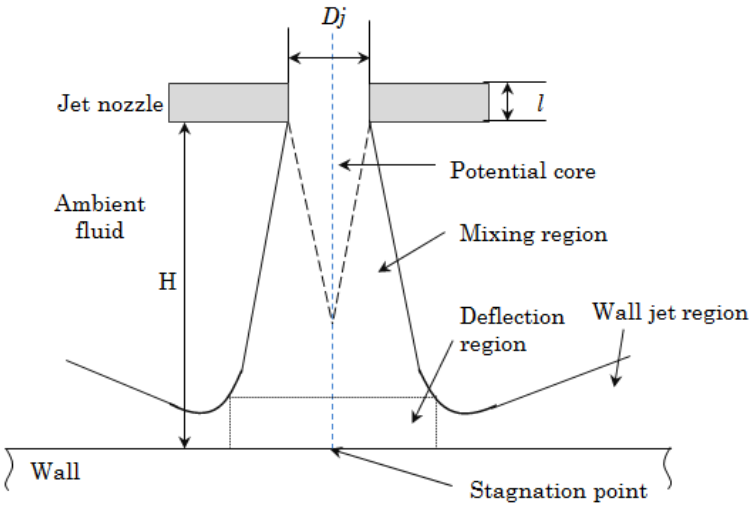

Figure 2.5. Flow regions of a single impinging jet (adapted with modifications from [61]).

side-ways due the presence of the solid wall. As a result, the static pressure near the wall increases due to the deceleration of the fluid. The increase in static pressure causes the formation of thin (in order of micrometers) thermal and hydrodynamic boundary layers. These thin boundary layers are responsible for establishing very high heat transfer coefficients obtained [62]. The fluid then starts to move parallel to the wall. This region is denoted as the wall jet region. In the wall jet region, the thermal and hydrodynamic boundary layers start to grow causing the heat transfer performance to degrade noticeably compared to the deflection region.

2.3.2. Radial Variation in the Heat Transfer Performance

The local heat transfer performance of a single jet deteriorates away from the stagnation zone. The variation of the local Nusselt number as a function of the dimensionless distance from the stagnation point (r/d) is depicted in Figure 2.6. In general, Figure 2.6 indicates that for a given H/D_j the Nusselt number is maximum at the stagnation point ($r/d = 0$) and then it decreased noticeably as r/d increases. In addition, it can be noticed that for $H/D_j \gtrsim 5$,

there is only one maximum Nusselt number value and it occurs at $r/d = 0$. In contrast, for $H/D_j \lesssim 5$, the Nusselt number profile shows an additional secondary local maxima. The presence of the secondary local maxima is believed to be associated with the transition of the boundary layer flow from laminar to turbulent. This mechanism does not apply for $H/D_j \gtrsim 5$ since turbulent boundary layer flow already exists at the stagnation region [61]. The experimental results of Garimella and Rice [63] for a single jet clearly indicate the presence of the primary and secondary Nusselt number peaks.

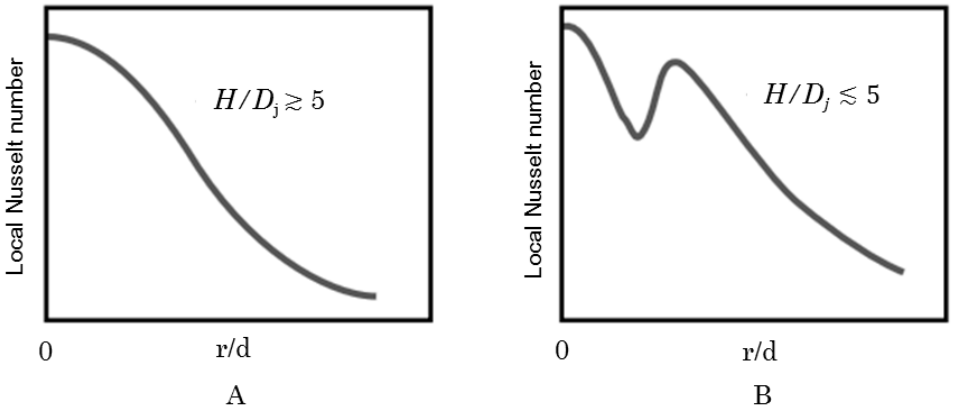

Figure 2.6. The variation of the local Nusselt number for a single jet for (A) large and (B) small jet-to-plate ratio (adapted with modifications from [54]).

2.3.3. Heat Transfer and Pressure Drop Characteristics of a Single Axisymmetric Submerged Jet

Heat transfer of free surface and submerged single jet impingement has been studied extensively. Experimental studies regarding the heat transfer in single impinging jet are reviewed and presented in Ma et al. [64] and Li and Garimella [65].

Elison and Webb [66] studied the heat transfer performance of free and submerged single, axisymmetric, water jets impinging vertically downwards. Tested jet diameters were 0.584, 0.315 and 0.246 mm. Jet Reynolds numbers

(Re) were varied from 300 to 7000 to span the laminar and turbulent flow regimes. For free and submerged jets, the experimental data showed that there is a transition from laminar to turbulent flow condition at Re = 2000. Correlations were formulated for the stagnation point and average Nusselt numbers for the jets under free and submerged working conditions. The authors focused on studying the heat transfer performance alone without quantifying the pressure drop required for the single jets.

Garimella and Nenaydykh [67] experimentally studied the effect of jet diameter and the aspect nozzle ratio (l/D_j) on the heat transfer performance of axisymmetric, normally impinging liquid jet using FC-77 as the working fluid. Tested jet diameters were in the range of 0.79 mm to 6.35 mm, Reynolds numbers were between 4000 and 23000. The nozzle aspect ratio was between 0.25 to 12. Heat transfer results indicated that larger D_j yield larger Nusselt numbers for fixed values of Re, l/D_j and H/D_j. It is believed the larger diameter jets generate larger turbulence intensity leading to higher Nusselt numbers. However, the stagnation and average heat transfer coefficient decreased as D_j increased (for fixed values of $/D_j$, H/D_j and Re). Additionally, the heat transfer coefficients are highest for l/D_j < 1. This behavior was attributed to the effect of the flow separation and reattachment on the jet exit velocity profiles. The effect of l/D_j on the heat transfer performance became less noticeable as H/D_j increased. Regarding fluid flow, the authors did not report the pressure drop required for the single submerged jet.

The thermal performance of free and submerged liquid jets was experimentally studied by Womac et al. [25]. Four different jets diameters ranging from 0.978 mm to 6.55 mm impinging on a square heater, water and FC-77 were used as the working fluids. Results indicated the heat transfer coefficient of submerged jets is highest for small separation distances (H/D_j =

4). In addition, for $Re \gtrsim 4000$ submerged jets achieved higher heat transfer coefficients compared to free jets. This behavior is attributed to the turbulence generated in the shear layer (i.e. mixing region) of the submerged jet. The pressure drop for the free and submerged jets was not measured.

Brignoni and Garimella [68] experimentally studied the effect of nozzle-inlet chamfering on pressure drop and heat transfer of confined air jets. Two jet nozzles with different chamfer angles were compared with a square-edged (unchamfered) jet nozzle. The experimental results indicated that chamfering the jet nozzle inlet decreased the pressure drop noticeably while slightly reducing the heat transfer coefficient. Chamfering the jet nozzle inlet removed the sharp edge located at the inlet of the unchamfered jet. The removal of the sharp edge (at the nozzle inlet) reduced the jet inlet pressure losses which caused a reduction in the jet's total pressure drop. Although pressure drop was measured, correlations for predicting it were not developed.

Regarding the pressure drop of a single jet, most studies have focused on characterizing the heat transfer of a single jet without quantifying the required pressure drop. Correlations capable of accurately predicting the pressure drop required for a single jet have not been developed yet. This is partially due to the strong dependence of the pressure drop required for a single jet on the jet nozzle geometry and configuration. From a design point of view, quantifying the pressure drop is important because it can be used along with the flow rate to determine, or at least estimate, the pumping power required for the jets. Estimating the pumping power required is a critical when designing and optimizing thermal load management systems.

2.3.4. Heat Transfer and Pressure Drop Performance Correlations for Single Axisymmetric Submerged Jet

Correlations are available for predicting the average and stagnation point Nusselt numbers for submerged jets. The heat transfer correlations were developed using different working fluids flowing through various jet nozzle shapes. A comprehensive summary of correlations regarding the heat transfer of free surface and submerged jets is presented by Molana and Banooni [69].

The heat transfer correlations dealing with single, submerged, circular liquid jets will be reviewed here. Table 2.2 includes various correlations for predicting the stagnation point Nusselt number, Nu_0, and the average Nusselt number, Nu, for single submerged circular liquid jets impinging vertically on a heated surface.

Regarding the jet's hydrodynamic behavior, correlations capable of predicting the pressure drop required for a single jet are not readily available in the literature.

Table 2.2. Correlations for the stagnation point and average Nusselt numbers for single, submerged, liquid impinging jet.

Study	Range of validity		Jet geometry	Fluid	Correlation
Garimella and Nenaydykh [67]	Re H/D_j l/D_j D_j	4000 - 23000 1 - 5 0.25 - 12 1.59 - 6.35 mm	Circular	FC-77	$Nu_0 = 0.492Re^{0.858}Pr^{0.4}\left(\frac{H}{D_j}\right)^{0.024}\left(\frac{l}{D_j}\right)^{-0.09}$
Garimella and Rice [63]	Re H/D_j l/D_j D_j	4000 - 23000 1 - 5 0.25 - 12 1.59 - 6.35 mm	Circular	FC-77	$Nu = 0.160Re^{0.695}Pr^{0.4}\left(\frac{H}{D_j}\right)^{-0.11}\left(\frac{l}{D_j}\right)^{-0.11}$
Li and Garimella [65]	Re H/D_j l/D_j D_j Pr D_e	4000 - 23000 1 - 5 0.25 - 12 1.59 - 25.2 0.7 - 25.2 11.28 - 22.56 mm	Circular	Air Water FC-77	$Nu_0 = 1.427Re^{0.496}Pr^{0.444}\left(\frac{l}{D_j}\right)^{-0.058}\left(\frac{D_e}{D_j}\right)^{-0.0272}$ $Nu = 1.179Re^{0.504}Pr^{0.441}\left(\frac{l}{D_j}\right)^{-0.071}\left(\frac{D_e}{D_j}\right)^{-0.0283}A_r + 1.211Re^{0.637}Pr^{0.441}\left(\frac{D_e}{D_j}\right)^{-1.062}(1-A_r)$ $D_e = \left(\frac{4A_h^2}{\pi}\right)^{0.5}$, $A_r = \left(\frac{1.9D_j}{D_e}\right)^2$

Table 2.2. (Continued)

Study	Range of validity		Jet geometry	Fluid	Correlation
Elison and Webb [66]	Re H/D_j D_j	3000 - 7000 <8 0.584 mm	Circular	water	$Nu_0 = \left[\left(Nu_{0,lam}\right)^p + \left(Nu_{0,turb}\right)^{-p}\right]^{1/p}$ where, $Nu_{0,lam} = 0.345Re^{0.697}$ and $Nu_{0,turb} = 1.5Re^{0.491}$ p =9
Sitheramayya and Raju [70]	Re H/D_j d_h/D_j D_j	2000 - 40000 1 - 7.1 8 - 58 1.74 - 12.65 mm	Circular	water	$Nu = Pr^{\frac{1}{3}}\left(\frac{D_j}{d_h}\right)^2 [32.49Re^{0.523} + 0.266\left(\frac{d_h}{D_j} - 8\right) \times Re^{0.828}]$
Yamamoto et al. (presented in [64])	Re H/D_j D_j	1000 - 8000 in potential core 3 mm	Circular	water	$Nu_0 = (0.6 - 0.8)Re^{0.5}Pr^{0.4}$ $Nu = 0.39Re^{0.5}Pr^{0.4}$

The local variation in the Nusselt number (Nu_x) is significantly influenced by r/D_j, H/D_j, Re and the nozzle configuration [61]. Therefore, Nu_x is difficult to predict and correlate accurately. Jambunathan et al. [61] introduced the following correlation for predicting the local Nusselt number, Nu_x,

$$Nu_x = kRe^a \tag{2.14}$$

where k and a are constants which depend on various geometrical parameters. The parameters $k = \mathrm{f}\left(\frac{r}{D_j}, \frac{H}{D_j}, n\text{ozzle configuarion}\right)$ and $a = \mathrm{f}\left(\frac{r}{D_j}, \frac{H}{D_j}\right)$. The parameter a can be found explicitly by using an equation given in [61]. However, k has to be determined graphically using figures presented in reference [61]. As it stands, the local Nusselt number correlation (Eqn. 2.14) is only applicable for the specific jet geometries studied in Jambunathan et al. [61]. Typically, local temperature measurements of the heated surface are performed when the local jet Nusselt numbers are required.

2.3.5. Single Jets and Jet Arrays

The variation of the heat transfer performance of a single jet along the heated surface directly affects the wall temperature distribution as seen in Figure 2.6. The wall temperature increases noticeably further away from the stagnation zone. For some electrical components such maldistribution in the surface temperature cannot be tolerated because it can cause failure or performance degradation. To remedy the temperature maldistribution issue, multiple jets arranged in an array can be used, instead of a single jet. A jet array produces evenly distributed heat transfer coefficient which in turn leads to more uniform temperature distribution [23].

Liquid jet arrays have not received the same amount of attention as single impinging jets [71]. A literature review regarding the heat transfer and fluid flow of liquid submerged jet arrays is discussed below. Few correlations have been proposed for predicting the heat transfer and the friction factors of submerged liquid jet arrays, these correlations are presented in Table 2.3.

Table 2.3. Correlations for predicting the Nusselt numbers and the friction factors for submerged jet arrays.

Study	Range of validity		Jet geometry	Fluid	Correlation
Womac et al. [72]	D_j	0.5133 mm and 1.02 mm	Circular	Two fluids tested, water and FC-77	$\frac{Nu_L}{Pr^{0.4}} = 0.509Re^{0.5}\left(\frac{L}{D_j}\right)A_r + 0.0363Re^{0.8}\left(\frac{L}{L^*}\right)(1 - A_r)$ L is the heater length. L^* is the average distance associated with the wall jet region. $L^* = \frac{1}{4}(\sqrt{2}+1)L_e - (0.91D_j)$ A_r is the effective area of the impingement regions to the total area of the heated surface $A_r = N_j\pi(1.9D_j)^2/L^2$
Robinson and Schnitzler [71]	Re D_j	1000 - 8000 1 mm	Circular	water	$Nu = 1.485Re^{0.46}\left(\frac{S}{D_j}\right)^m\left(\frac{H}{D_j}\right)^n Pr^{0.4}$ For $2 \le \frac{H}{D_j} \le 3$ and $3 \le \frac{S}{D_j} \le 7$: $m = -0.442$ and $n = -0.00716$ For $5 \le \frac{H}{D_j} \le 20$ and $3 \le \frac{S}{D_j} \le 7$: $m = -0.121$ and $n = -0.427$ $f = 0.51 + \frac{229.9}{Re}$

Womac et al. [72] conducted experimental studies on free and submerged jets arrays using water and FC-77 as working fluids. 2 × 2 and 3 × 3 jet arrays of circular jets were studied, jet diameters ranged from 0.513 mm to 1.02 mm. Results showed that heat transfer of a jet array is unaffected by jet-to-target spacing (H) for the range of $2 \leq H/D_j \leq 4$. However, the heat transfer performance degraded for small ($H/D_j < 2$) and large ($H/D_j \geq 10$) jet-to-target separations. The maximum average heat transfer coefficient was found to occur at $H/D_j \approx$ 3 to 4. In addition, it was noticed that, for similar operating conditions, submerged jets performed equally or better when compared to free jets. The authors also investigated the effect of the jet-to-jet (S/D_j) on the heat transfer of the jet array. For the 2 × 2 array two S/D_j configurations (S/D_j = 6.22 and 9.96) were tested. Results indicated that the heat transfer performance of the jet array with S/D_j = 6.22 was better compared to the jet array with S/D_j = 9.96. The authors attributed this behavior to smaller heated area being covered by the wall jet region, and the interactions between the jets before impingement region which were believed to induce turbulence leading to enhanced heat transfer performance. The pressure drop requirements for the jet array were not discussed.

Robinson and Schnitzler [71] studied the heat transfer and pressure drop of free and submerged jets experimentally. The jet arrays had 21, 45 and 121 jets with 1 mm jet diameter. Jet-to-jet spacing was 3, 5 and 7 mm jet diameters. Tested jet Reynolds numbers were between 650 to 6400. Experimental results for the impinging jet arrays showed that the heat transfer performance was independent of jet-to-target spacing (H/D_j) when the jets were in close proximity to the target ($2 \leq H/D_j \leq 3$). However, for larger jet-to-plate separation ($5 \leq H/D_j \leq 20$) the heat transfer performance deteriorated. The results also indicated that for a fixed jet Reynolds number

and H/D_j, submerged liquid jet arrays with smaller S/D_j offer better heat transfer performance compared to jet arrays larger S/D_j. Increasing the spacing between adjacent jets increased the distance between the regions of high heat transfer of the jet array, which resulted in a decrease in the heat transfer performance of the whole jet array.

Robinson and Schnitzler [71] determined the friction factors and the pumping power requirements for the tested jet arrays. Results indicated that, for a given heat transfer coefficient, submerged liquid jet arrays with closely spaced jets require the smallest pumping power compared to other array configurations.

Robinson [55] analytically studied the thermal and hydrodynamic performance of a submerged jet array and microchannel heat sinks aimed at electronics cooling. Both heat sinks were designed to cool a 20 mm × 20 mm heated area. Various configurations of minichannels and jet arrays were studied. Results indicated that although microchannels have lower heat transfer coefficients compared to jet arrays, the thermal resistance of microchannels was either the same or lower when compared to the thermal resistance of the jet array studied. The lower thermal resistance of microchannels was attributed to the larger heat transfer area of the microchannels compared to the heat transfer area of the impinging jet arrays.

Jet impingement arrays have been used, so far, for designing and building small size heat sinks for cooling electrical components. Whelan et al. [73] have designed a submerged jet array heat exchanger (D_j = 1 mm) with a cooling area of 824 mm^2 (28.7 mm × 28.7 cm) for CPU cooling. Similarly, the impinging jet array heat sink (D_j = 0.5 mm) studied by Lou and Liu [74] was designed for cooling an LED array with a substrate area of 225 mm^2 (15 mm × 15 mm). The projected heat transfer area of the jet array systems, studied to date, is smaller compared to the area of a typical TEG module which is 40

mm × 40 mm. As they stand, such jet array designs are not suitable for implementation in waste heat recovery systems due to their small cooling area.

2.4. Heat Exchanger Designs Integrated with TEG Systems

Researchers have studied the performance of a small scale heat exchangers integrated into the cold side of a single TEG for heat dissipation. These small size heat exchangers typically use air or water as the working fluid. For example, Hsu et al. [75] designed and tested low–temperature waste heat harvesting system to recover the thermal energy from the exhaust gases of an automobile. The removal of the excess thermal energy from the TEG's cold side was achieved by utilizing an electrical fan forcing air through an aluminum plane-fin mounted on the cold side of a single TEG. The waste heat recovery system had 24 individual heat sinks with one heat sink per TEG module which was 52 mm × 52 mm.

Rezania et al. [76] studied the effect of coolant flow rate on the power generated by one TEG module integrated with a 56 mm × 56 mm microchannel heat sink (D_h = 0.93 mm). Test results indicated that as the coolant flow rate is increased, the pumping power required and the electrical power generated by the TEG increase as well. However, the pumping power increased with a greater rate compared to the increase in electrical power generated. It also was found that for a given ΔT across the TEG, there is a specific coolant flow rate that gives the maximum net power generated by the system.

The studies of Hsu et al. [75] and Rezania et al. [76] are few examples of cold side heat exchangers integrated into the cold side of a single TEG module. However, waste heat recovery systems typically implement multiple TEGs for electrical energy generation. For such systems, larger size cold side

heat exchangers are required for dissipating the thermal energy from multiple TEG modules simultaneously.

Other studies have focused on designing and implementing larger scale cold side heat exchangers capable of cooling multiple TEG modules simultaneously. However, these studies did not focus on the thermal and hydrodynamic performance of the cold side heat exchangers implemented in the waste heat recovery system. For instance, Niu el al. [77] designed and studied the performance of a waste heat recovery system using thermoelectric generators. The system utilized a total of 56 thermoelectric modules sandwiched between four layers of hot and cold heat exchangers. A mixture of water/glycol was used as the working fluid which circulated through the cold side heat exchanger. The cold side heat exchanger utilized was made from a single rectangular aluminum passage 40 mm × 8 mm in cross section and 600 mm long. The heat exchanger was designed to cool 14 TEG modules arranged in one row.

The heat recovery system designed and tested by Dai et al. [78] utilized water flowing through plate-type heat exchanger made from aluminum. The heat exchanger dimensions were 270 mm × 100 mm × 16 mm and it was designed 10 TEG modules 50 mm × 50 mm. The heat exchanger utilized forced convection through two parallel 8 mm in diameter passages machined along the length of the cold plate.

The shortcoming of the studies of Niu et al. [77] and Dai et al. [78] is that they did not characterize the thermal and hydrodynamic performance of the cold side heat exchangers. In addition, the effect of the heat exchanger performance on the total power generated was not studied. As mentioned before, the design of the cold and hot side heat exchanger could affect the total electrical power generated significantly. Thus, when designing waste heat recovery systems the thermal and hydrodynamic performance of the cold

and hot side heat exchanger requires further investigation. The thesis is a first attempt of many aimed at broadening the research regarding the design and characterization of flat-plate cold side heat exchangers, capable of cooling multiple TEG modules simultaneously for implementation in waste heat recovery systems.

3. Heat Exchanger Prototypes

This chapter discusses the expected performance and the design features of each different heat exchanger prototype investigated in this thesis. The heat exchanger prototypes are designed to dissipate the thermal load of 14, 40 mm × 40 mm TEG modules simultaneously. The heat exchangers are designed to dissipate a thermal load of approximately 50 – 60 kW/m^2 per single TEG module.

3.1. The Minichannels Heat Exchanger Prototype

The minichannels heat exchanger prototype utilizes the concept of forced convection fluid flow through minichannels as a heat removal technique.

3.1.1. Selecting a Minichannel Configuration and Predicting the Thermal and Hydrodynamic Performance

The minichannels heat exchanger prototype is designed to cool 14 TEG modules. The TEGs will be arranged in two rows located side by side with 7, 40 mm × 40 mm TEGs per row. Based on the TEG arrangement, the length of the "cooling area" must be at least 280 mm in order to accommodate 7 TEG in series. The width of the cooling area was chosen to be 90 mm in order accommodate 2 TEGs side by side with some spacing between the rows.

The idea is to use multiple minichannels arranged in parallel in which the cooling water will flow and remove the thermal energy from the heated surface. Regarding the channel geometry, the channel width (W_{ch}) and the fin thickness (t_{fin}) are designed to have equal dimensions, since this configuration is found to offer the minimum thermal resistance for a microchannel heat sink [26]. The channel height (H_{ch}) was chosen to be equal to the channel width (i.e. aspect ratio, β=1) such that square channels are formed. To find the optimum minichannel size, the performance of 5

minichannel sizes was studied thermally and hydrodynamically using analytical correlations. The details of the analytical studies are presented below.

As discussed in Section 1.3.1, the TEG's heat flux is q'' = 52.1 kW/m^2. Given that there are 14 TEGs modules, 40 mm × 40 mm, the total thermal energy, Q, that must be dissipated is,

$$Q = q'' A_{TEG} \times N_{TEGs} \tag{3.1}$$

where A_{TEG} is the TEG projected area, and N_{TEGs} is the number of TEGs. Using equation 3.1, Q was found to be 1.167 kW. For testing purposes, purified water was chosen as the working fluid because of its availability, cost effectiveness and well known transport properties. To reduce the surface temperature distribution, the temperature rise through of the water (ΔT_{water}) was limited to 5 °C only. Based on these constraints the required coolant mass flow rate ($\dot{m}$) can be found using Eqn. 3.2.

$$Q = \dot{m} C_p (\Delta T_{water}) \tag{3.2}$$

where C_p is the specific heat capacity of water. Assuming the average water temperature (T_{avg}) is 25 °C then the value of C_p is 4180 kJ/kg·K. Using the values of Q and C_p in Eqn. 3.2, the required coolant mass flow rate is 0.06 kg/s. The number of minichannels (N_{ch}) and minichannel size (W_{ch} and H_{ch}) will dictate the heat transfer performance. Various minichannel configurations were studied analytically to choose the most appropriate minichannel design.

Heat transfer from the minichannels is quantified by the following equation,

$$Q = \eta_{fin} h A \, \Delta T_{LM} \tag{3.3}$$

where h is the heat transfer coefficient, A is he heat transfer area and ΔT_{LM} is the log-mean temperature difference between the cooling water and the heat exchanger surface. For a given thermal energy transferred to the heat

exchanger (Q_{HX}) higher thermal conductance (hA) is desired in order to reduce ΔT_{LM} leading to better system performance. For an adiabatic tip boundary condition, the fin efficiency, η_{fin}, can be calculated using the following equation,

$$\eta_{\text{fin}} = \frac{\tanh \text{m}L}{\text{m}L} \tag{3.4}$$

where m is a constant and L is the fin length. The value of constant m can be found using the following equation.

$$\text{m} = \sqrt{\frac{2h}{kD_h}} \tag{3.5}$$

where k, in equation 3.5, is the thermal conductivity of minichannel material which is aluminum in this design. The heat transfer coefficient, h, can be calculated using the Nu and the hydraulic diameter (D_h) of the minichannel.

$$h = \frac{NuD_h}{k} \tag{3.6}$$

where k is the thermal conductivity of the water. Given the specified mass flow rate and the minichannel length it is expected that the flow regimes in the minichannel will be simultaneously developing. To predict the Nusselt number (Nu) for the each minichannel configuration, the Hausen correlation (Eqn. 2.3) is used because it is capable of predicting Nu in the simultaneously developing regimes.

$$Nu = 3.66 + \frac{0.0668(D_h/L)Re_D\text{Pr}}{1 + 0.04[(D_h/L)Re_DPr]^{2/3}}$$

The parameter L is the minichannels length which was chosen to be 90 mm, Pr is the Prandtl number for water and Re_D is the Reynolds for a single minichannel.

$$Re = \frac{\rho V_{ch} D_h}{\mu} \tag{3.7}$$

where ρ and μ are the water density and viscosity, respectively. All the thermophysical properties of water including Pr were evaluated at an average water temperature of 25 °C. The parameter D_h is the minichannel hydraulic diameter which is a function of the minichannels flow area (A_{flow}) and its perimeter (P) as shown below,

$$D_h = \frac{4A_{flow}}{P} \tag{3.8}$$

The flow area (A_{flow}) is the cross sectional area for a single minichannel where the coolant flows and it is given by,

$$A_{flow} = W_{ch} \times N_{ch} \tag{3.9}$$

The parameter V_{ch} in Eqn. 3.7 is the coolant flow velocity inside a single channels, V_{ch} can be calculated by,

$$V_{ch} = \left(\frac{\dot{m}}{N_{ch}\rho A_{flow}}\right) \tag{3.10}$$

Upon selecting a minichannel geometry (i.e. W_{ch} and H_{ch}), the number of minichannels can be determined. Then, the minichannel Reynolds number is calculated based on the mass flow rate which was 0.06 kg/s and the minichannel configuration. The minichannel geometrical dimensions along with Re and Pr are used in the Hausen correlation to find Nu. Once Nu was found, h was calculated and the thermal conductance hA for that particular minichannel was determined.

The pressure drop associated with the minichannel is due to the wall friction, and inlet and outlet minor losses at the inlet and outlet of the minichannels, as illustrated in Figure 3.1.

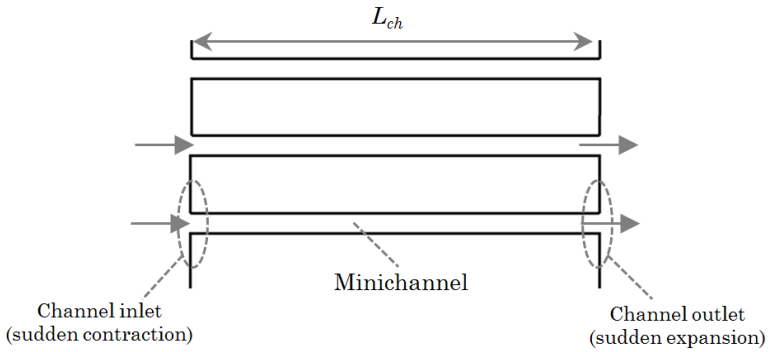

Figure 3.1. A schematic drawing illustrating the minichannels arrangement and the different pressure drop components associated with the arrangement.

The pressure drop required[2] for the minichannels heat exchanger can be determined using Eqn. 3.11.

$$\Delta P = f_{app}\frac{L_{cl}}{D_h}\frac{\rho V_{ch}^2}{2} + \left(K_c\frac{\rho V_{ch}^2}{2}\right)_{channel\ inlet} + \left(K_e\frac{\rho V_{ch}^2}{2}\right)_{channel\ outlet} \quad (3.11)$$

Since the flow inside the minichannels is expected to be laminar and simultaneously developing, the apparent friction factor has to be used. The laminar apparent Darcy friction factors, f, were calculated based on Eqn. 3.12.

$$f_{app} = 4\left[\frac{3.44}{Re\sqrt{L^*}} + \frac{(f_{FD}^* Re) + \frac{K(\infty)}{4L^*} - \frac{3.44}{\sqrt{L^*}}}{Re\left(1 + \frac{C}{L^{*2}}\right)}\right] \quad (3.12)$$

The value of $(f_{FD}^* Re)$ depends on the channels aspect ratio (β). By design the minichannels have an aspect ratio equal to 1. Thus the value of $(f_{FD}^* Re)$ was found to be 14.227 for β = 1 [58]. The constant C is also a function of β. Its value is equal to 0.00029 for β=1 [58]. The Hangenback factor $K(\infty)$ was calculated using Eqn. 2.12, for β = 1 and the value of $K(\infty)$ was 1.43.

K_c and K_e, in Eqn. 3.11, are the sudden expansion and contraction loss coefficients and are strong function of the flow area geometry. The cross

[2] The calculated pressure drop is for the minichannels only; it does not include any other losses that are typically present in any heat exchanger design (ex. fitting and manifold pressure losses).

sectional area of the minichannels was smaller than the inlet and outlet area (A_{ch}/A_{inlet} and $A_{ch}/A_{outlet} \approx 0$). Based on the area ratios, K_c and K_e values were found using Figure 3.2 to be 0.5 and 1 respectively. The values of f, K_c, and K_e were calculated and used in Eqn. 3.11 in order to determine the value of the pressure drop, ΔP.

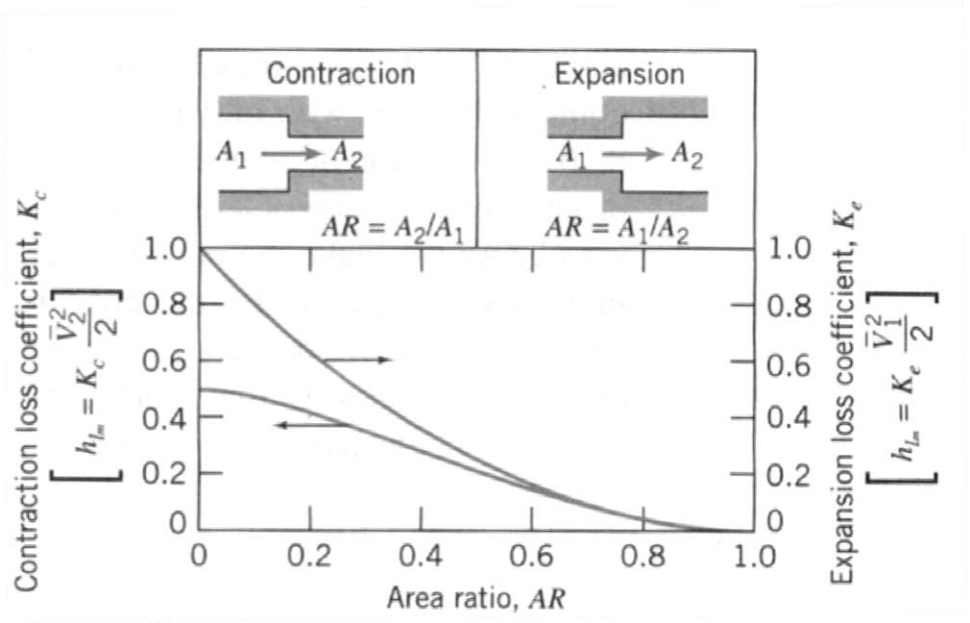

Figure 3.2. Expansion and contraction loss coefficients due to sudden change in flow area [60].

The calculated pressure drop along with the density and mass flow rate were used to calculate the required hydraulic pumping power, P_p.

$$P_p = \frac{\dot{m}\,\Delta P}{\rho} \tag{3.13}$$

The actual required pumping power, P_E, will depend on the pump efficiency; for this calculation the pump efficiency (η) will be assumed to be 80%.

$$P_E = \frac{P_P}{\eta} \tag{3.14}$$

Five different minichannel configurations were studies analytically with D_h ranging from 0.5 mm to 3 mm. The thermal and hydrodynamic performance of each minichannel configurations is presented in Table 3.1.

Table 3.1. Analytical study results for five different minichannel configurations.

D_h (mm)	N_{ch}	hA (W/K)	ΔT_{LM} (°C)	ΔP (kPa)	P_E (W)
0.5	280	207.9	5.6	33.936	2.6
0.75	186	149.5	7.8	4.774	0.4
1	140	119.6	9.7	1.243	0.1
2	70	72.5	16.1	0.072	0.006
3	46	55.1	21.1	0.020	0.002

As seen in Table 3.1, hA and P_E increase as D_h decreases and vice versa. The thermal conductance of the minichannels with $2 \leq D_h \leq 3$ mm is relatively low ($hA \leq 75$ W/K) which leads to ΔT_{LM} greater than 15 °C. Due to the low hA, implementing these minichannel configurations in the heat exchanger design is not appealing, even though the pumping power required is much less than 0.01 W. For the minichannels configurations with $0.5 \leq D_h \leq 0.75$ mm, the hA is high which resulted in $\Delta T_{LM} < 8$ °C which is very appealing from a heat transfer point of view. However, machining such minichannels sizes using conventional machining methods is complicated which makes them difficult to implement in the minichannels heat exchanger. In addition, the pumping power required is significantly larger compared to the other minichannel configurations. Due to the aforementioned arguments, minichannels with $0.5 \leq D_h \leq 0.75$ mm were not selected for making the minichannels heat exchanger prototype.

On the other hand, minichannels with $D_h = 1$ mm offer good thermal performance ($\Delta T_{LM} \approx 10$ °C) with moderate pumping power requirements compared to the other minichannels configurations. Due to the good thermal performance and the relative ease of machining, minichannels with $D_h = 1$ mm were selected for making the minichannels heat exchanger prototype.

The detailed design of the minichannels heat exchanger is presented in the following section.

3.1.2. Minichannels Heat Exchanger Design and Fabrication

The minichannels heat exchanger consists of two main parts a heat transfer plate and a heat exchanger body. The minichannels were machined on the bottom surface of the heat transfer plate using high precision CNC milling centre (Matsuura LX-1). The minichannels heat exchanger prototype is shown in Figure 3.3. Aluminum (6061-T6) was chosen as the material for the heat exchanger surface because it has several desired characteristics such as ease of machining, good thermal conductivity (177 W/ m·K at 23 °C [20]) and its cost effectiveness.

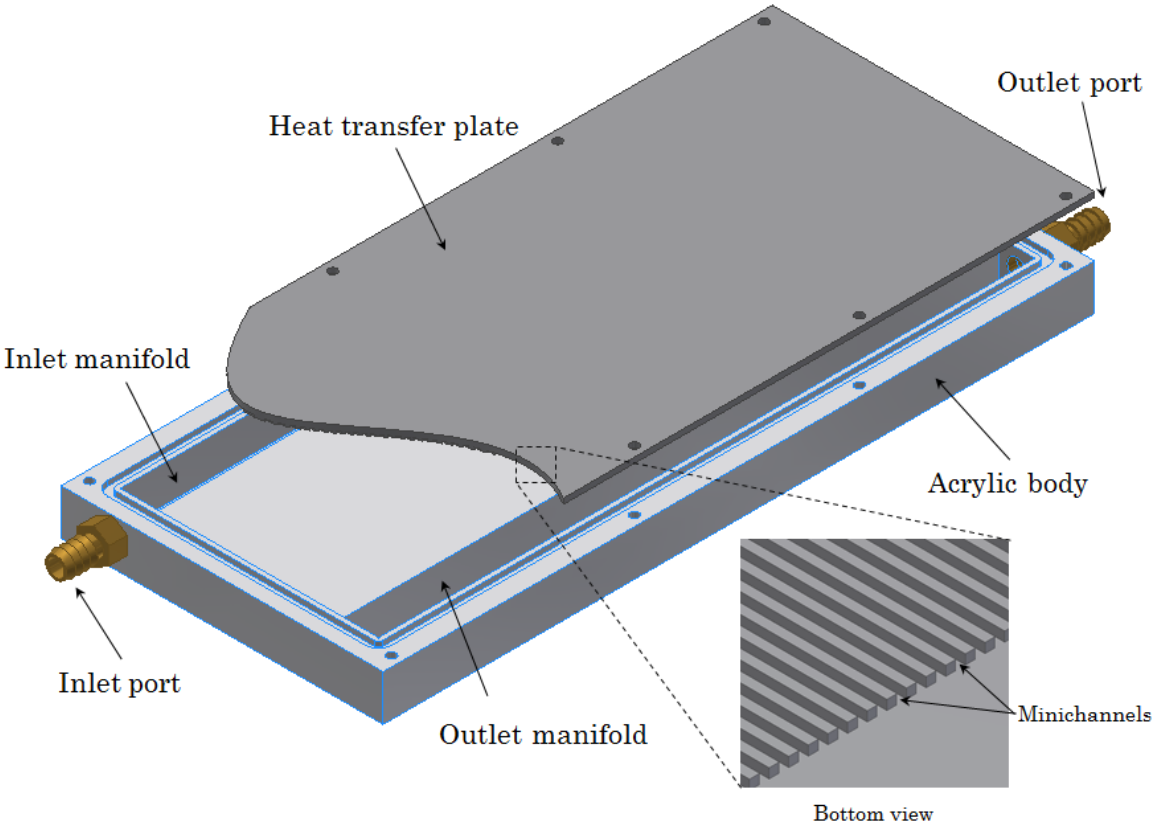

Figure 3.3. A CAD model showing the minichannels heat exchanger design.

As discussed in the previous section, 1 mm × 1 mm square shaped minichannels, 90 mm long are utilized by minichannels heat exchanger. This minichannel configuration allowed for 140 parallel minichannels to be machined on the heat transfer plate. The minichannel configuration (140 minichannels, 1 mm × 1 mm) allowed for laminar flow conditions inside the minichannels. In laminar flow, the pressure drop required is linearly proportional to the flow velocity ($\Delta P \propto V$). In comparison the pressure drop in the turbulent regime is proportional to the flow velocity squared ($\Delta P \propto V^2$). To reduce the required pressure drop, the system was designed to operate within the laminar regime under normal operating conditions.

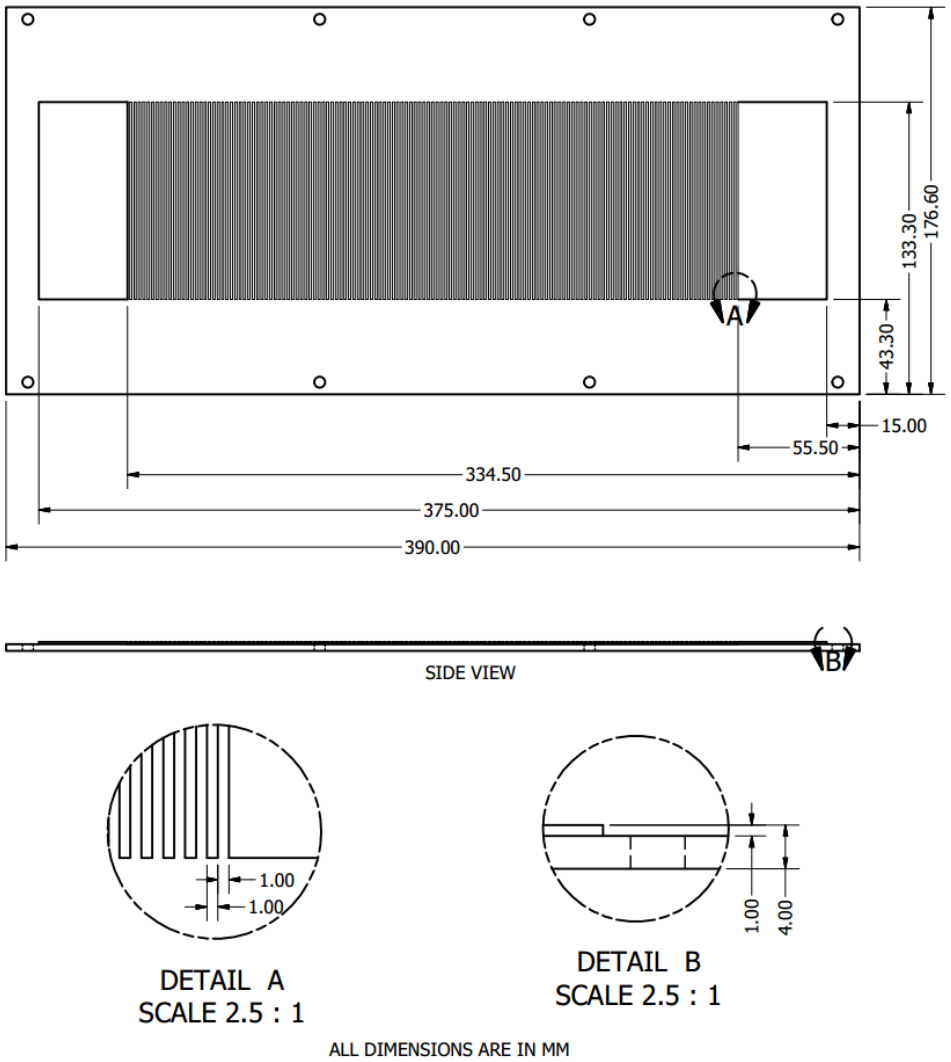

Figure 3.4. A CAD drawing showing the overall dimensions of the heat transfer plate. Details A and B illustrate the minichannels design.

The purpose of the heat transfer plate is to transfer the applied thermal loads to the cooling water flowing through the heat exchanger. The heat transfer plate is 390 mm long × 176.6 mm long × 4 mm thick. Figure 3.4 shows the design features of the minichannel heat transfer surface. Details (A) and (B) show the minichannel width, depth and wall thickness.

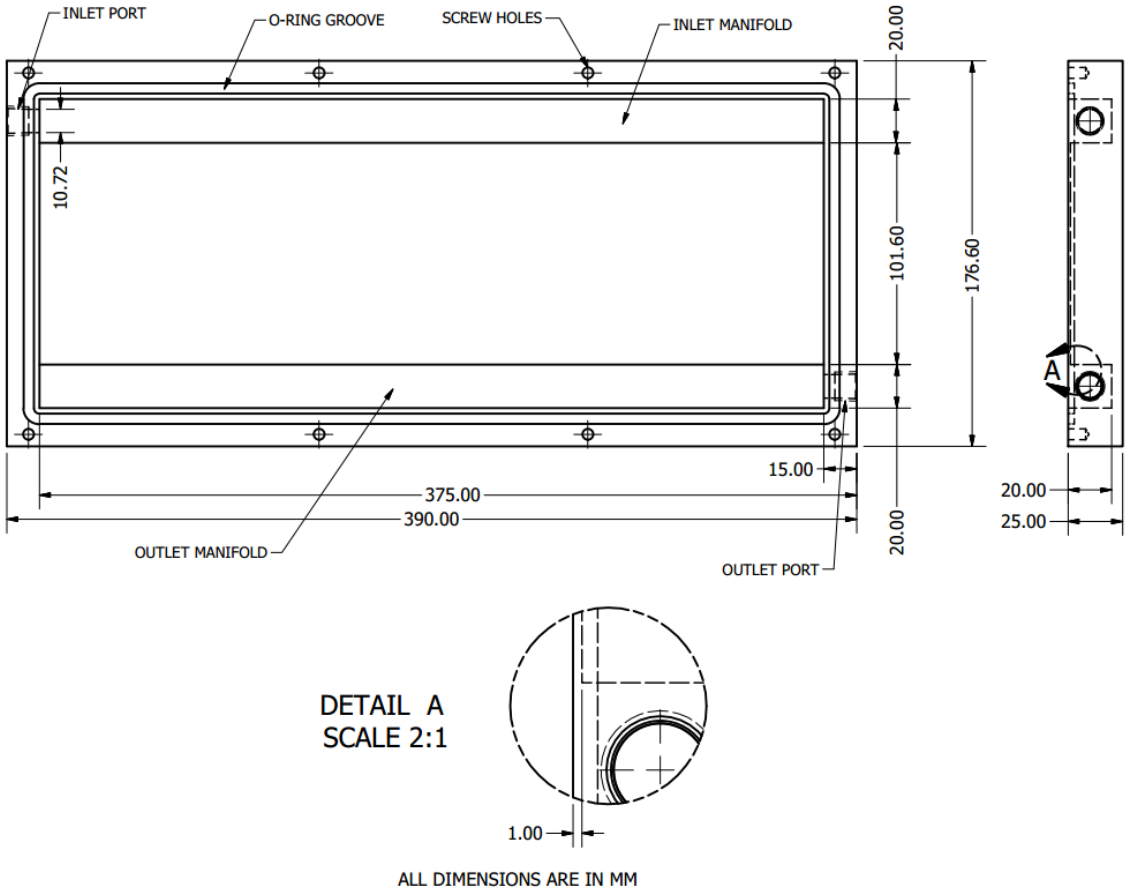

Figure 3.5. A CAD drawing showing acrylic base dimensions. Detail A shows the undercut surface for accommodating the minichannels.

The heat exchanger body, fabricated using acrylic glass, was designed to deliver the cooling water to and from the minichannels via inlet and outlet manifolds and to insulate the minichannels walls tip. As illustrated in Figure 3.3, each manifold is connected to a 1/4" NPT to 1/2" hose fittings such that coolant can be supplied and removed from the heat exchanger. Figure 3.5 shows a CAD drawing for the acrylic heat exchanger body. Note that the inlet and outlet hose fitting (seen in Figure 3.3) are not included.

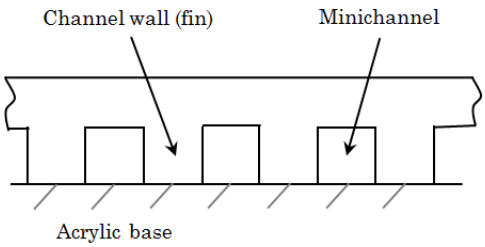

Figure 3.6. A schematic showing the minichannels with the insulated tip boundary condition.

The heat transfer plate containing the minichannels is mounted on top of the acrylic base as illustrated in Figure 3.6. Thus, the minichannel walls are modelled as fins with insulated tip boundary condition since the thermal conductivity of the acrylic (≈ 0.2 W/m·K at 25 °C [21]) is smaller than the aluminum, which means little or no heat will transfer from the fins tip.

3.2. The Impinging Jets Heat Exchanger Prototype

The impinging jets heat exchanger prototype utilizes submerged liquid jets travelling upwards and impinging on a surface as the heat removal technique.

3.2.1. Selecting a Submerged Jet Configuration and Predicting the Thermal and Hydrodynamic Performance

The basic idea of the impinging jets heat exchanger is to use a single jet to dissipate the thermal from one TEG. The impinging jets heat exchanger is designed to cool 14 TEGs. Therefore the number of required jets is 14. The heat transfer plate must be at least 280 mm long × 80 mm wide. The submerged impinging jets will thermally interact with a flat plate for which the heat transfer area (A) is equal to 0.0224 m^2, which is equivalent to the projected area of 14, 40 mm × 40 mm TEGs modules.

The next step is to determine a suitable jet diameter based on the identical design conditions used in the Section 3.1.1 which are Q = 1.167 kW

and $\dot{m}$ of 0.06 kg/s. Multiple circular jet diameters ranging from 1.7 mm to 4 mm are analytically studied to identify the appropriate jet diameter for the impinging jets heat exchanger. The details of the analytical study are presented below.

The heat transfer due to convection inside the impinging jets heat exchanger can be calculated using the following equation,

$$Q = hA\Delta T_{LM} \tag{3.15}$$

The convection area, A, is specified to be 0.0224 m^2. To find the heat transfer coefficient, the Nusselt number for the impinging jets must be found first. The correlation by Sitheramayya and Raju [70] was to predict the Nu for the submerged jets.

$$Nu = Pr^{\frac{1}{3}}\left(\frac{D_j}{d_h}\right)^2 [32.49Re^{0.523} + 0.266\left(\frac{d_h}{D_j} - 8\right) \times Re^{0.828}] \tag{3.16}$$

The term d_h is the diameter of the heated area for a single jet. For this particular case the heated area for a single jet is equal to the TEG area. Therefore the parameter d_h was taken to be 40 mm since the TEGs used are 40 mm × 40 mm. Re is the jet's Reynolds number which was calculated using Eqn. 3.7 using the jet diameter (D_j) as the characteristic length instead of D_h. All the thermophysical properties of water and the Pr were evaluated at an average water temperature of 25 °C. The calculated values of Re and Pr were used in Eqn. 3.15 to predict the jet Nusselt number which was later used to calculate h and subsequently the thermal conductance, hA for each jet configuration.

As discussed previously in the literature review, correlations capable of predicting the pressure drop for a single jets are not available in the literature. Therefore pressure drop losses have to be determined a different method. A single jet typically has a sudden area contraction at the inlet and a

sudden expansion the outlet; a typical jet configuration is schematically depicted in Figure 3.7.

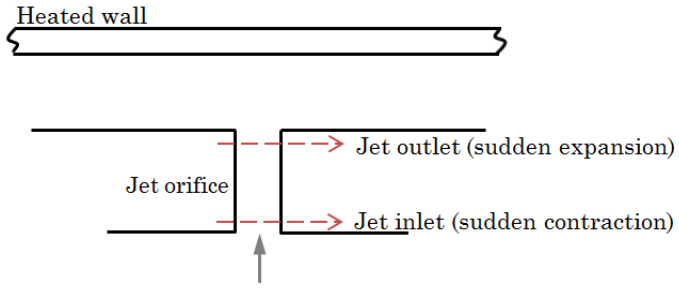

Figure 3.7. A schematic showing the sudden expansion and contraction at the inlet and outlet of a single jet respectively.

The pressure drop associated with the sudden expansion and can be calculated using Eqn. 3.17. The calculated pressure drop will be lower than the actual pressure drop for the heat exchanger prototype. This analysis is only sufficient for making qualitative observations.

$$\Delta P = \left(K_c \frac{\rho V_j^2}{2}\right)_{jet\ inlet} + \left(K_e \frac{\rho V_j^2}{2}\right)_{jet\ outlet} \tag{3.17}$$

The ratio of the jet flow area compared to the inlet and outlet area is very small ($\approx$ 0), therefore the values of the expansion and contraction loss coefficients, K_c and K_e, were found to be 0.5 and 1 respectively (refer to Figure 3.2). The parameter V_j is the jet velocity and it can be calculated by using the following equation.

$$V_j = \left(\frac{\dot{m}}{N_{jets}\rho A_{flow}}\right) \tag{3.18}$$

where A_{flow} is the flow area for a single jet which and it is given by,

$$A_{flow} = \frac{\pi D_j^2}{4} \tag{3.19}$$

The calculated pressure drop for each jet configuration was used to estimate the pumping power required (P_E) using Eqn. 3.14. The thermal and

hydrodynamic performance results for each jet configuration are presented in Table 3.2.

Table 3.2: Analytical study results for the different impinging jet configurations.

D_j (mm)	A (m^2)	hA (W/K)	ΔT_{LM} (°C)	ΔP (kPa)	P_E (W)
1.7	0.0224	158.5	7.4	2.667	0.2
2	0.0224	143.8	8.1	1.397	0.1
3	0.0224	118.1	9.9	0.276	0.02
4	0.0224	108	10.8	0.087	0.01

The study results indicate that smaller jet diameters have higher thermal conductance (hA) and also higher pumping power. Although their thermal conductance is $40 - 50\%$ better, jet configurations with $1.7 \leq D_j \leq 2$ mm had a minimal effect on ΔT_{LM} and require approximately one order of magnitude higher pumping power compared to jet configurations with $3 \leq D_j \leq 4$ mm. Due to the higher pumping power required, jet diameters $1.7 \leq D_j \leq 2$ mm with were not selected for designing impinging jets heat exchanger. The jet configurations with $3 \leq D_j \leq 4$ mm have lower pumping power requirement ($P_E << 0.1$ W). However the thermal performance of the 3 mm jet configuration is approximately 10% higher compared to the 4 mm jet configuration. Due to their good thermal performance and relatively low pumping power requirements, 3 mm diameter jets were selected for designing the impinging jets heat exchanger prototype. The detailed design of the impinging jets heat exchanger is reviewed in the next section.

3.2.2. Impinging Jets Heat Exchanger Design and Fabrication

The impinging jets heat exchanger has three main parts a heat transfer plate, a heat exchange body, and the bottom base plate. A CAD model illustrating the design of the impinging jets heat exchanger is shown in

Figure 3.8. Aluminum (6062-T6) alloy was used to machine the three heat exchanger parts due to good thermal properties and cost effectiveness.

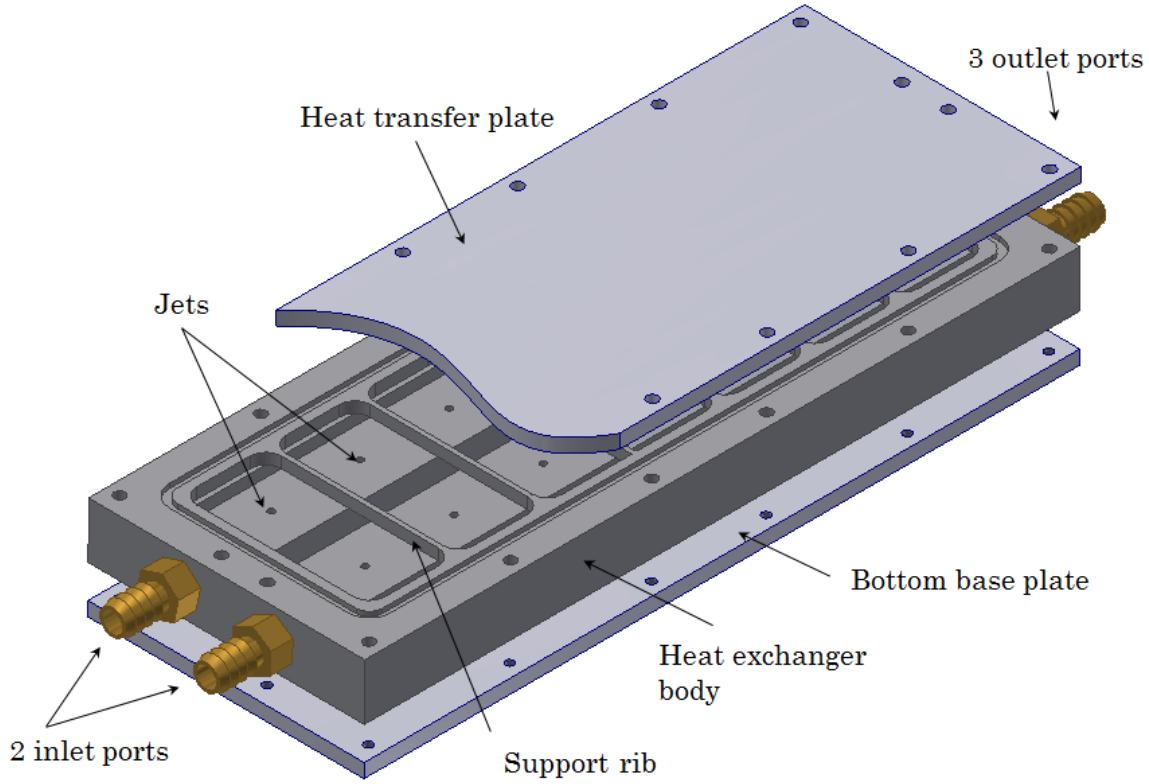

Figure 3.8. A 3D CAD model showing the design of the impinging jets heat exchanger.

The heat transfer plate (depicted in Figure 3.8) has dimensions of 324 mm long × 125 mm wide × 6 mm thick and it is made from flat aluminum plate. The heat exchanger body housed the impinging jets, inlet/outlet ports and their respective manifolds, as seen in Figure 3.9. The jets are arranged in two rows 42.50 mm apart. Each jet row contains 7 jets spaced 40.29 mm apart. All the jets operate in parallel and they are spaced such that the jets do not interact with each other which means that the performance of one jet does not affect the performance of a neighbouring jet. Pipe type (i.e. square-edged) jet nozzles with 3 mm jet diameter are machined in the heat

exchanger body, as illustrated in Figure 3.9. Features such as the cooling sections are machined on the top surface of the heat exchanger surface (Figure 3.9), while other features such as the inlet and outlet manifolds are machined on the bottom surface of the heat exchanger body (Figure 3.10).

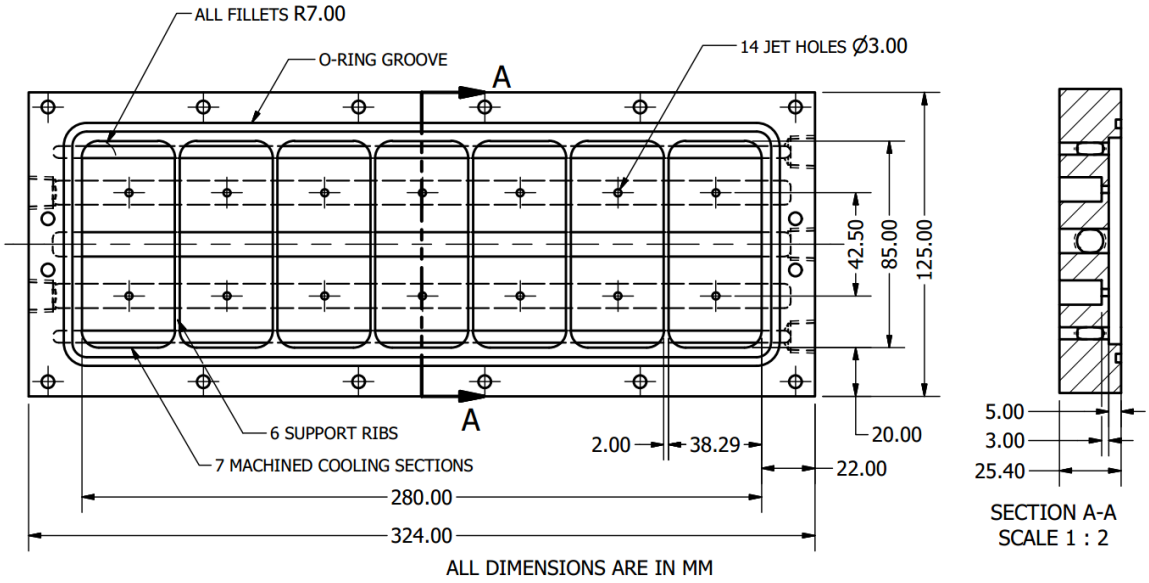

Figure 3.9. A CAD drawing showing the design features on the top surface of the heat exchanger body.

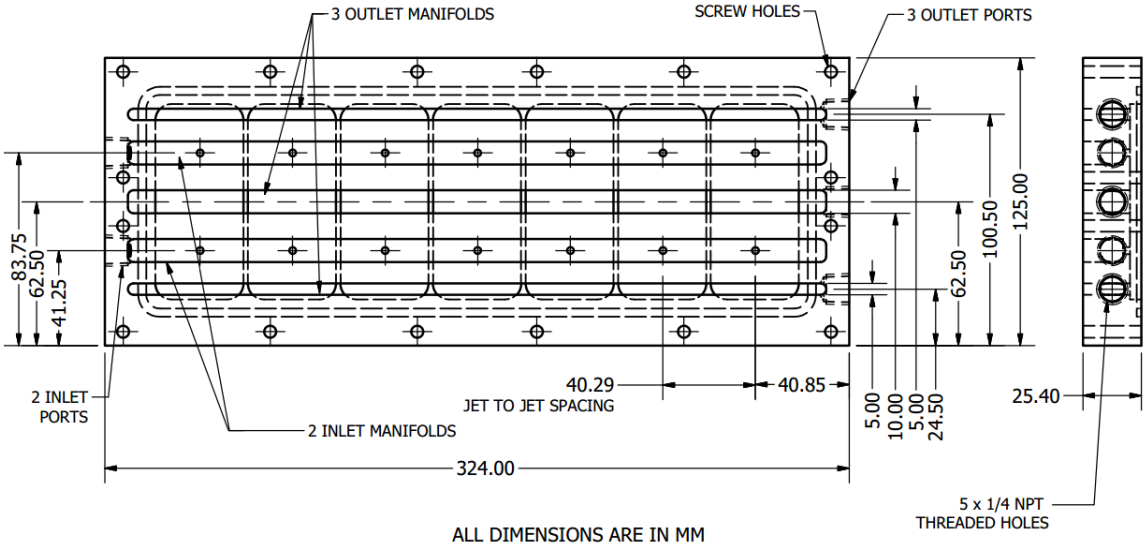

Figure 3.10. A CAD drawing showing the design features on the heat exchanger body's bottom surface.

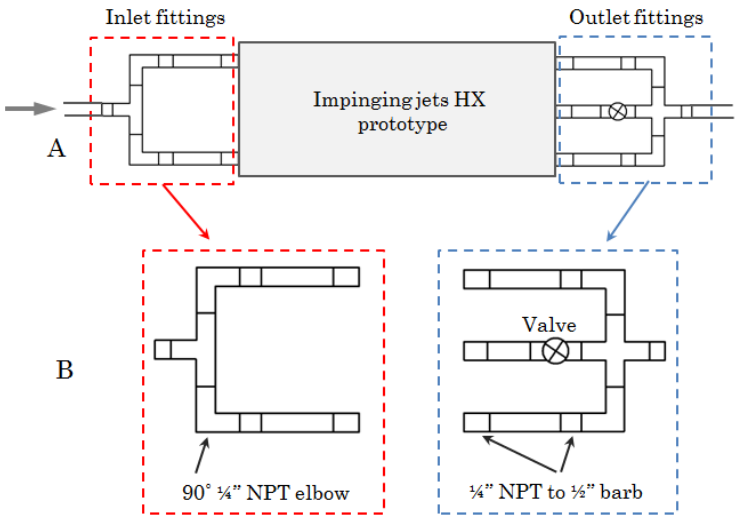

Figure 3.11. A schematic diagram depicting the impinging jets heat exchanger and its inlet and outlet fittings (A), (B) is a detailed schematic showing the design of the inlet and outlet fittings**.**

The jet-to-plate spacing is 5 mm. Support ribs are formed by leaving 2 mm gap between the adjacent pockets. The purpose of the support wall is to provide structural support for the heat exchanger plate and to prevent it from bending when clamping pressure is applied to the heat exchanger.

Coolant is supplied to the jets via two inlet manifolds located underneath each jet row. After impinging on the heat exchanger surface, the coolant exited the heat exchanger via three outlet manifolds, two located on the sides and one located at the middle of the heat exchanger body. Refer to Figure 3.10 for details. Each manifold has a threaded port on one of its sides such that a 1/4" NPT-1/2" hose barb fitting can be connected to the manifold to deliver coolant in/out from the manifold.

The middle outlet manifold (seen in Figure 3.10) receives coolant from both jet rows. Therefore, it is designed to be twice as wide as the side manifolds, which received coolant from only one jet row. Ideally, the coolant flow rate exiting the middle outlet manifold should be equal to the total coolant flow rate exiting both side manifolds. Upon preliminary testing, it

was observed that the flow rate in the middle manifold was slightly greater than the sum of the side manifolds. A ball valve was added to the middle manifolds to correctly adjust the flow distribution in the middle manifold and make it equal to the sum of the flow rate exiting the side manifolds. This configuration is depicted in Figure 3.11 (A). The coolant is delivered to heat exchanger using inlet and outlet fittings the design of which is shown in Figure 3.11 (B).

A summary of the main design features for the minichannels heat exchanger and the impinging jets heat exchanger is presented in Table 3.3.

Table 3.3. A comparison of the main features for both heat exchanger prototypes.

	Minichannels heat exchanger	Impinging jets heat exchanger
Cooling technique	Flow through minichannels	Jet impingement on a flat surface
Heat transfer area	0.0378 m^2	0.0224 m^2
Number of jets, jet diameter	N.A	14 jets D_j = 3 mm
Number of minichannels, D_h	140, D_h = 1 mm	N.A
Overall heat exchanger dimensions	390 × 176 × 29 mm^3	324 × 125 × 38 mm^3
Heat transfer plate material, plate thickness	Aluminum, 4 mm	Aluminum, 6 mm
Heat exchanger body material	Acrylic	Aluminum
Number of inlet fitting(s), fitting type	1, 1/4" NPT to 1/2" hose barb	2, 1/4" NPT to 1/2" hose barb
Number of outlet fitting(s), fitting type	1, 1/4" NPT to 1/2" hose barb	3, 1/4" NPT to 1/2" hose barb

4.Experimental Methodology

This chapter presents a detailed description of the experimental facility, procedures, data reduction methods and experimental uncertainties for the results obtained.

4.1. The Experimental Facility

The experimental facility was designed and built to be able to test the different heat exchanger designs thermally and hydrodynamically. The primary function of the experimental facility was to supply a known amount of thermal energy to the heat exchanger prototype and remove that thermal energy using cooling water flowing through the heat exchanger. By quantifying the amount of energy transferred to the cooling water, surface temperature of the heat exchanger and the cooling water mass flow rate, thermal parameters for that particular heat exchanger were calculated. These parameters were thermal conductance, heat transfer coefficient and the Nusselt number for the heat exchanger. The calculated parameters gave insight into the thermal performance of the heat exchanger. Thus, they were used for comparing the different heat exchanger prototypes.

A detailed schematic of the experimental facility is shown in Figure 4.1. The experimental facility is composed of a copper spreader, a stainless steel block (SS block), cooling loop, clamping mechanism in addition to several measurement instrumentations. Flexible thermal insulation was added to the test section to reduce the thermal losses from/to the test section.

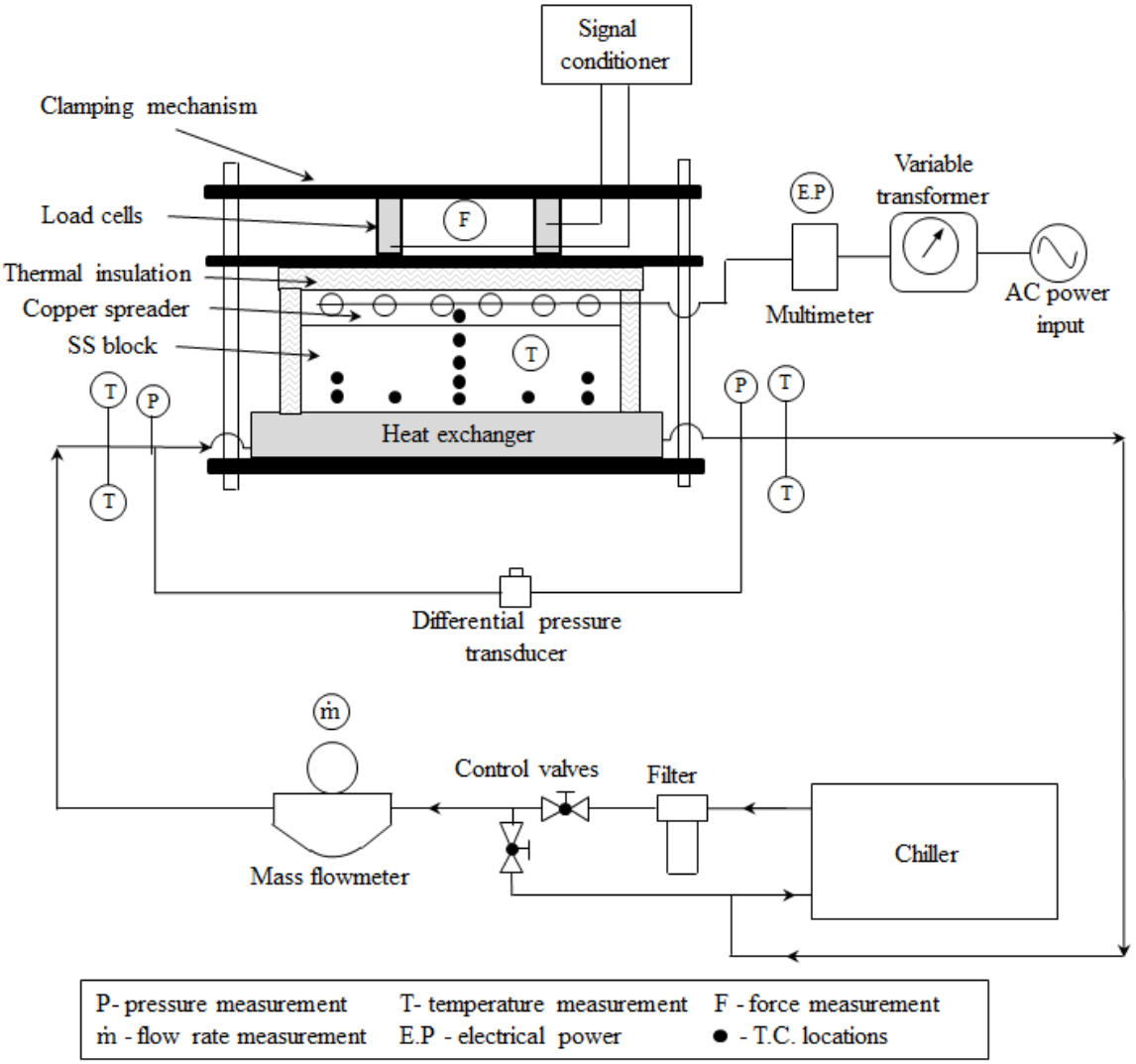

Figure 4.1. Schematic of the experimental facility used to test the different heat exchanger prototypes.

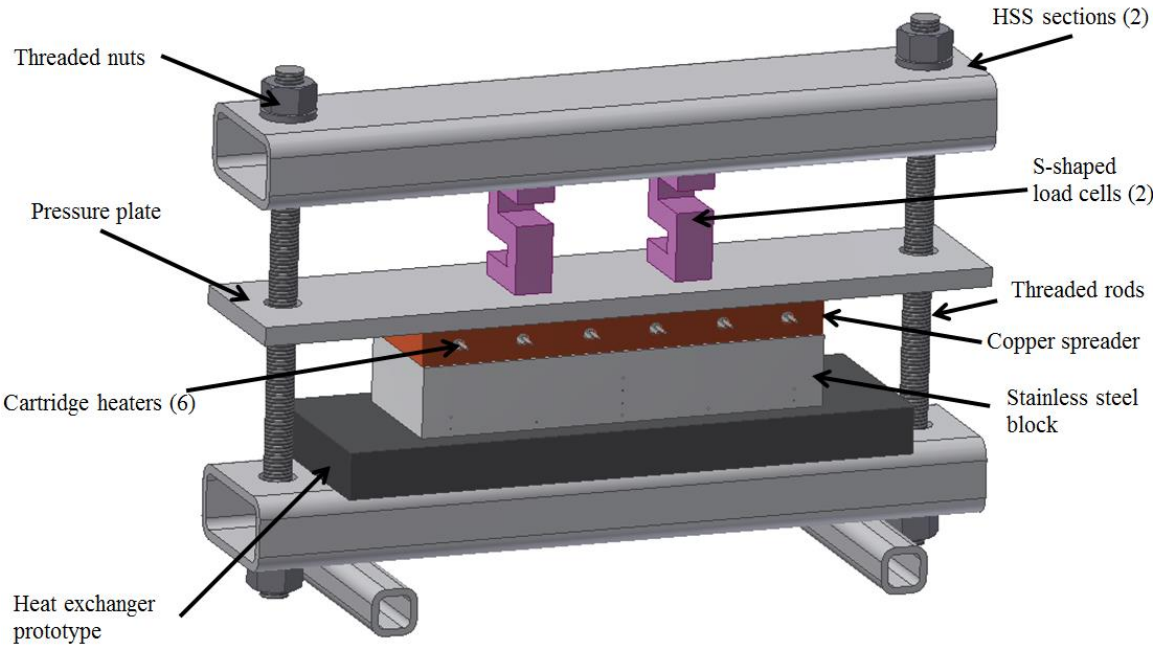

Figure 4.2. 3D CAD model of the test section showing the different components and the position of the heat exchanger prototype.

4.1.1. The Copper Spreader

Copper (C110) was chosen as a housing material for the electrical heaters to insure that a uniform temperature distribution boundary condition was established at the top surface of the SS block. A detailed CAD drawing for the copper spreader is shown in Figure 4.3. The copper spreader dimensions were 280 mm long × 84 mm wide × 25.4 mm in height. Six 300 W electrical cartridge heaters (Omega CSH-2023001/120) were embedded in the copper spreader. Five socket screws were used to attach the copper spreader to the top surface of the SS block.

The electrical power supplied to the heaters was controlled using a variable transformer (Staco 3PN1010). A true RMS multimeter (Extech 382860) connected after the transformer and before the electrical heaters was used to measure the amount of electrical power supplied to the heaters. The thermal energy generated by the electrical heaters is denoted $Q_{heaters}$.

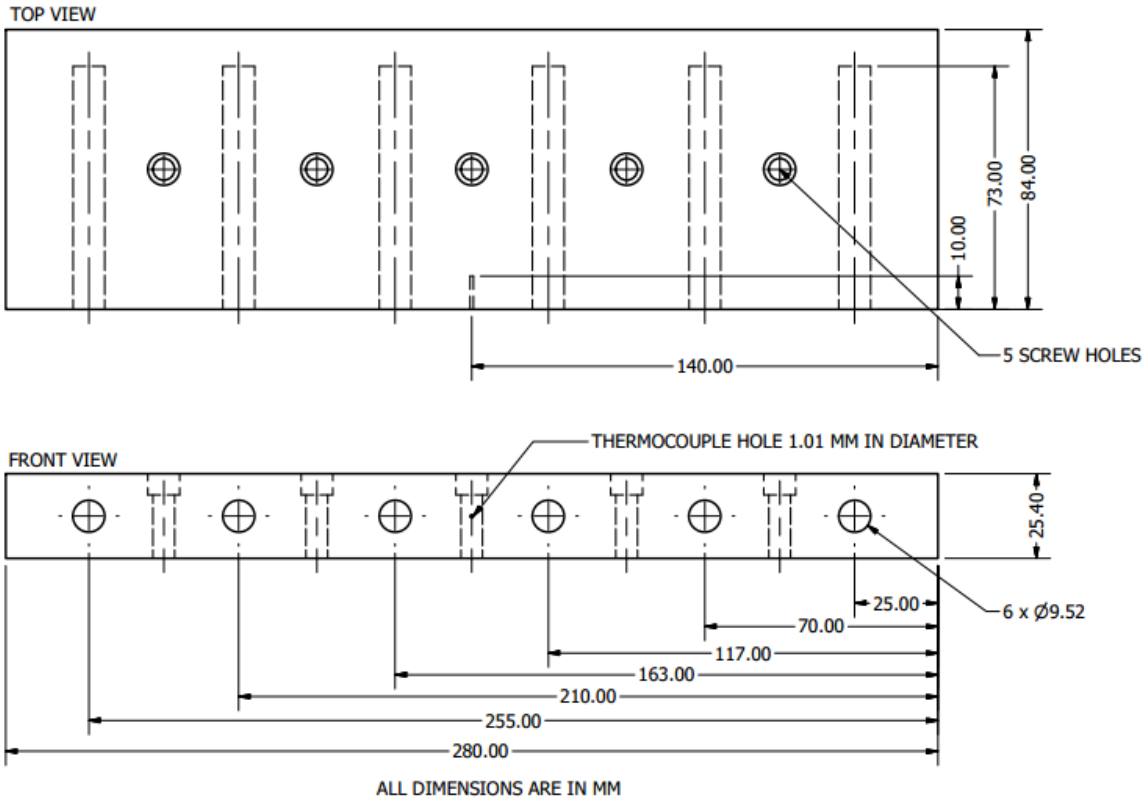

Figure 4.3. Detailed drawing of the copper spreader showing the design and dimensions, shown top and front view.

The temperature of the copper spreader was measured at one location, for reference, using E-type thermocouple (Omega EMQSS-040-G-6). The sides of the copper block were wrapped with 5 layers of flexible thermal insulation 3 mm thick (FiberFrax Ceramic Fiber Paper 970, k = 0.06 W/m·K at mean temperature of 600 °C [79]). In addition, multiple layers of thermal insulation (FiberFrax) with total thickness of 42 mm were added between the top surface of the copper block and the pressure plate. It was calculated that adding insulation to the copper block reduced the thermal losses to about 12 W ($Q_{heaters}$= 855 W).

4.1.2. The Stainless Steel Block (SS block)

To assess the heat exchanger performance, the energy input to the heat exchanger and its surface temperature must be known. The design of the SS block was based upon ASTM D5470 where well-characterized metal bars and thermocouples are used for quantifying the heat flux and the surface temperature values.

As shown in Figure 4.4, the cross sectional area of the SS block is 90 mm × 280 mm. This is equivalent to two rows of seven, side by side, 40 mm × 40 mm TEGs, with some spacing between the two rows. The height of the SS block is such that the thermal resistance of the SS block is equivalent to the thermal resistance of TEG modules. The SS block is made from AISI 304 stainless steel alloy. The relatively low thermal conductivity yields a large temperature gradient across the SS block thus allowing for accurate estimation of the surface temperature.

Ten E-Type thermocouples (Omega EMQSS-040-G-6) were used to measure temperature of the stainless steel block at various locations. Thermocouple arrangement, shown in Figure 4.4, allowed for determining the temperature distribution near to the bottom surface of the SS block and the temperature gradient at the centerline and the edges of the SS block. The top and the bottom surface of the stainless steel block were finished using surface grinding technique to yield a flat (surface tolerance ≈ ±0.05 mm) and smooth surface (estimated roughness ≈ 8 μm), which was essential for reducing the contact resistance. A layer (≈ 0.05 mm thick) of thermal paste (Arctic Silver 5, k = 9 W/m·K [80]) was applied to the top surface of the SS block in order to reduce the thermal contact resistance between the SS block and the copper spreader. The estimated interface thermal resistance became 2.2E-4 °C/W which is smaller compared to the thermal resistance of the SS block (0.12 °C/W). The SS block was wrapped with multiple layers of flexible thermal

insulation (FiberFrax) with total thickness of 15 mm. It was calculated that the insulation reduced the thermal losses from the SS block to approximately 10 W (@ $Q_{heaters}$ = 855 W).

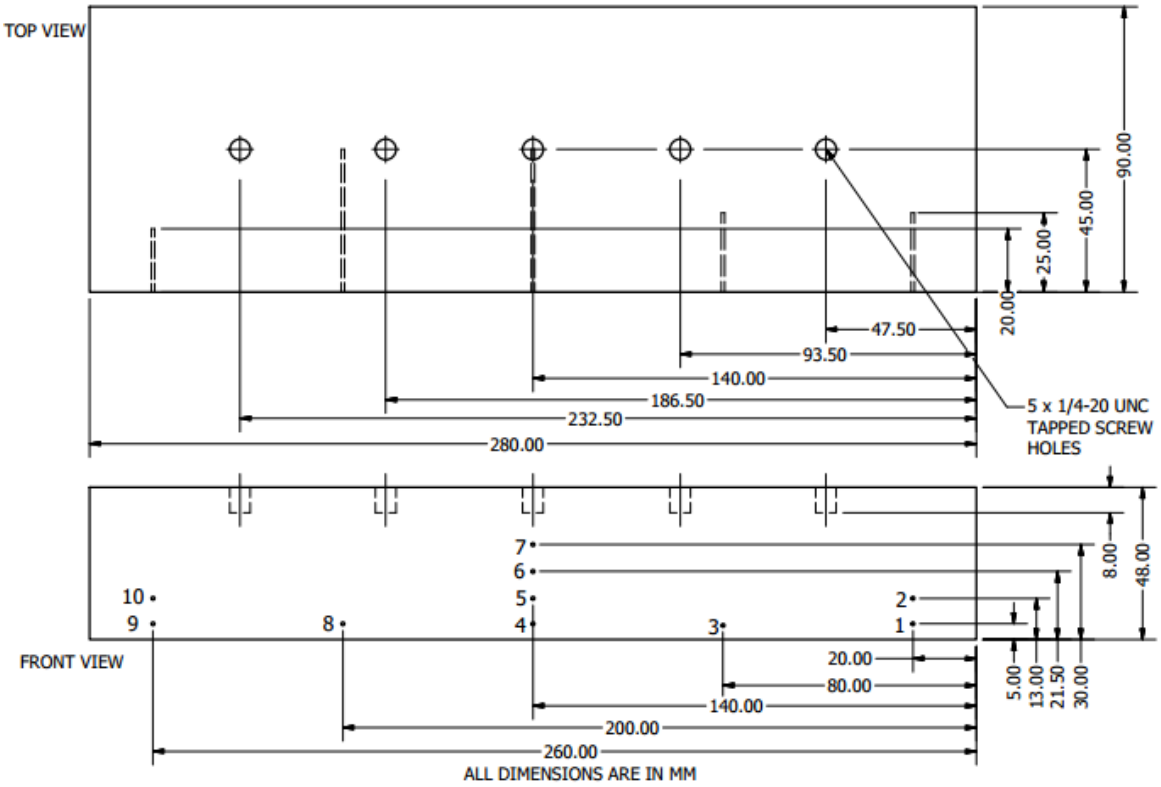

Figure 4.4. Detailed drawing of the SS block showing the block dimensions and thermocouples locations and their numbers.

4.1.3. The Cooling Loop

Purified water was pumped and maintained at a constant temperature by using a chilling unit (Lytron RC045). A Coriolis effect mass flow meter (Endress+Hauser Proline Promass 80E) is used for accurately measuring the mass flow rate of the water. Four T-type-thermocouples (Omega TMQSS-040-G-4) were used to measure the water inlet/outlet temperatures to the heat exchanger (two thermocouples at the inlet and two at the outlet). This thermocouple arrangement was chosen in order to improve measurement

accuracy by reducing the effect of the coolant's thermal boundary layer. In addition, using two thermocouples at the same location to measure the inlet and outlet coolant temperatures results in a lower measurement uncertainty. The readings from the inlet and outlet thermocouples were averaged to find an average inlet and average outlet water temperatures. These measured parameters along with water properties were used to calculate the thermal energy transferred to the water.

The flexible hoses and inlet and outlet fittings, used to deliver the water to and from the heat exchanger, were wrapped with flexible thermal insulation in order to reduce any thermal gains or losses from the surroundings. Typically, the temperature difference between the coolant and the ambient air was about 3 °C to 6 °C.

Pressure drop across a heat exchanger is measured using a differential pressure transducer (Validyne DP15 with a 34 kPa, 5 PSI, pressure diaphragm). A signal conditioner (Validyne CD23) was used to condition the signal from the pressure transducer before it was read by the DAQ system. The differential pressure transducer was calibrated using high accuracy pressure calibrator (Crystal is33).

4.1.4. The Clamping Mechanism

The clamping mechanism provided the necessary clamping force needed to reduce the contact resistance between the heat exchanger and the SS block. The SS block was positioned on the cooling surface of the heat exchanger and the entire assembly was clamped using the clamping mechanism as illustrated in Figure 4.2.

The clamping mechanism is made from two rectangular HSS (Hallow Structural Sections) 50.8 mm high × 101.6 mm wide × 355.6 mm long (2" high × 4" wide × 14" long). A steel plate denoted as "pressure plate" with

dimensions of 12.7 mm high × 101.6 mm wide × 355.6 mm long (1/2" thick × 4" wide × 14" long) is used to distribute the clamping force (transferred through the load cells) evenly along the top surface copper spreader. Two high strength threaded rods with matching nuts were utilized for applying the desired value of clamping force. Two load cells (Interface SSM-AJ-10kN) were calibrated and embedded between the top HSS section and the pressure plate to measure the value of the applied clamping force as seen in Figure 4.2. A signal conditioning amplifier (Vishay Precision Group, model 2360B 4-channel enclosure) is used to amplify the signal from the load cells.

4.1.5. Data Acquisition System

Data measured using the experimental facility is acquired using the following National Instruments cards,

- NI 9213 (16-Channel Thermocouple Input Module, 1200 S/s, ±78.125 V)
- NI9219 (4-Channel 24-Bit Universal Analog Input, 100 S/s, ±60 V)

The NI cards are housed in a NI CompactDAQ 8-Slot USB Chassis which is connected to a dedicated Data Processing Computer. LabVIEW program was installed on the Data Processing Computer and used to display and record the raw data. After saving the raw data, appropriate calibration curves were applied to the raw data. All the data post-processing and data reduction calculations were performed using Microsoft Excel.

The SS block temperatures were used to determine whether or not the system was at steady state conditions. For testing purposes, the system was deemed to be at steady state if the temperature fluctuations in the SS block thermocouples were less than 0.1 °C over a period of 5 minutes. Once the system was at steady state conditions, a LabVIEW program was used to

record 120 samples for the next minute. The various parameters measured in the experimental facility are outlined in Table 4.1.

Table 4.1. Measured parameters using the experimental facility.

Symbol	Measured Parameters
$T_{SS:1,2,3,4,5,6,7,8,9,10}$	Temperatures of the SS block at locations 1, 2, 3, 4, 5, 6, 7, 8, 9 and 10
T_{copper}	Temperature of the copper spreader
$T_{W\_in:1,2}$	Temperatures of the inlet water (two locations)
$T_{W\_out:1,2}$	Temperatures of the outlet water (two locations)
$\dot{m}$	Mass flow rate of the cooling water
F_{LFC}	Force measured by the left load cell
F_{RFC}	Force measured by the right load cell
$Q_{heaters}$	Electrical power supplied to the cartridge heaters
ΔP	Pressure drop for the heat exchanger

4.2. Data Reduction

The rate of energy flow through the SS block, Q_{ss}, is calculated based on the average temperature gradient using Eqn. 4.1.

$$Q_{ss\_avg} = k_{ss} \times A_{ss} \times \left(\frac{dT}{dx}\right)_{SS\_avg} \tag{4.1}$$

The variation k_{ss} with temperature for AISI 304 stainless steel is adapted from Ho and Chou [81]. The average temperature gradient $\left(\frac{dT}{dx}\right)_{ss\_avg}$ was the arithmetic average of $\left(\frac{dT}{dx}\right)_{ss\_CL}$, $\left(\frac{dT}{dx}\right)_{ss\_Right}$ and $\left(\frac{dT}{dx}\right)_{ss\_left}$ as shown in the equation below,

$$\left(\frac{dT}{dx}\right)_{ss\_avg} = \frac{\left(\left(\frac{dT}{dx}\right)_{ss\_CL} + \left(\frac{dT}{dx}\right)_{ss\_Right} + \left(\frac{dT}{dx}\right)_{ss\_left}\right)}{3} \tag{4.2}$$

The equation for temperature gradient at a specific location is given by,

$$\left(\frac{dT}{dx}\right) = \frac{n\sum x_i T_i - \sum x_i \sum T_i}{n\sum x_i^2 - \left(\sum x_i\right)^2} \tag{4.3}$$

where T_i is the temperature measured by the thermocouple, and x_i is the location of the thermocouple from the bottom surface of the SS block, as seen in Figure 4.4. Thermocouples 4, 5, 6, and 7 were used in Eqn. 4.3 to calculate $\left(\frac{dT}{dx}\right)_{ss\_CL}$, 1 and 2 were used to determine $\left(\frac{dT}{dx}\right)_{ss\_Right}$, and finally 9 and 10 were used to determine $\left(\frac{dT}{dx}\right)_{ss\_Left}$.

Q_{water} is calculated using Eqn. 4.4. The specific heat capacity, C_p, of water is a function of temperature. It was evaluated at the average water temperature.

$$Q_{water} = \dot{m} \times C_p \times (\overline{T}_{w\_out} - \overline{T}_{w\_in}) \tag{4.4}$$

The average temperatures of the water at the inlet and the outlet were obtained by averaging the inlet thermocouples reading.

$$\overline{T}_{w\_in} = \frac{(T_{w\_in1} + T_{w\_out2})}{2} \tag{4.5}$$

$$\overline{T}_{w\_out} = \frac{(T_{w\_out1} + T_{w\_out2})}{2} \tag{4.6}$$

4.2.1. Calculating Heat Transfer and Fluid Flow Parameters

The amount of heat transfer by the heat exchanger is governed by,

$$Q_{HX} = h \times A \times \Delta T_{LM\_CL} \tag{4.7}$$

Q_{HX} is the heat transferred from the heat exchanger to the cooling water. It was assumed to be equal to Q_{water}. Rearranging Eqn. 4.7, the following equation was obtained for calculating hA,

$$hA = \frac{Q_{water}}{\Delta T_{LM\_CL}} \tag{4.8}$$

where A is area over which the forced convection occurs. Each heat exchanger prototype has its unique value of A. The convection area (A) is dependent on the design of the heat exchanger.

The heat transfer coefficient, h, is calculated by dividing both sides of Eqn. 4.8 by A to get,

$$h = \frac{Q_{water}}{A \times \Delta T_{LM\_CL}} \tag{4.9}$$

where the log mean temperature difference ΔT_{LM_CL} is given by,

$$\Delta T_{LM\_CL} = \frac{\left(T_{s\_CL} - \bar{T}_{w\_out}\right) - \left(T_{s\_CL} - \bar{T}_{w\_in}\right)}{\ln\left(\frac{T_{s\_CL} - \bar{T}_{w\_out}}{T_{s\_CL} - \bar{T}_{w\_in}}\right)} \tag{4.10}$$

where $\bar{T}_{w\_in}$ and $\bar{T}_{w\_out}$ are calculated before using Eqn. 4.5 and 4.6 respectively. T'_{s_CL} was calculated by extrapolating $\left(\frac{dT}{dx}\right)_{ss\_CL}$ to the interface between the heat exchanger and the SS block.

$$T'_{s\_CL} = \bar{T} - \left(\frac{dT}{dx}\right)_{ss\_CL} \bar{x} \tag{4.11}$$

where $\bar{T}$ is the average temperature read by the thermocouples in the SS block and $\bar{x}$ thermocouple locations respectively.

The parameter $\left(\frac{dT}{dx}\right)_{ss\_CL}$ is calculated using four temperature measurements. Therefore its value is more accurate than that of $\left(\frac{dT}{dx}\right)_{ss\_Rigth}$ and $\left(\frac{dT}{dx}\right)_{ss\_Left}$ which are calculated using only two temperature measurements. Note that T'_{s_CL} is the temperature at the interface between the SS block and the aluminum plate. The thermal resistance of the aluminum plate is small, but nevertheless, it is taken into account when calculating the temperature at the aluminum plate-water interface which is T_{s_CL}. Then the values of T_{s_CL} is used in Eqn. 4.10 to calculate ΔT_{LM_CL}.

Nusselt number is defined by the following equation,

$$Nu = \frac{hD}{k_w} \tag{4.12}$$

where D is characteristic diameter. For the minichannels heat exchanger prototype (square shaped minichannel 1 mm × 1 mm) D is equivalent to D_h which is equal to 1 mm. For the impinging jets heat exchanger D is equal to the jet diameter which is 3 mm.

Reynolds number, Re, for the water flow fluid flow is a function of water density and viscosity, flow velocity and hydraulic diameter, as shown by the following equation,

$$Re = \frac{\rho_w V D}{\mu_w} \tag{4.13}$$

For the minichannels heat exchanger, V is the water velocity in a single minichannel. Likewise, for the impinging jets heat exchanger, V is the velocity for a single jet. V is a function of the water flow rate, water density and the flow area. Each heat exchanger prototype has its unique flow area, A_{flow}. The flow velocity is calculated as

$$V = \frac{\dot{m}}{\rho_w \times A_{flow}} \tag{4.14}$$

For the minichannels heat exchanger A_{flow} was equal to the cross sectional area of a single minichannel. For the impinging jets heat exchanger A_{flow} was equal the cross sectional area of a single jet.

The hydraulic pumping power required to circulate the water through the heat exchanger is a function of the total pressure drop across the heat exchanger (ΔP) and the coolant flow rate flowing ($\dot{\forall}$) through it, as shown in Eqn. 4.15,

$$P_p = \dot{\forall} \times \Delta P = \left(\frac{\dot{m}}{\rho_w}\right) \times \Delta P \tag{4.15}$$

4.3. The Energy Balance

A comparison between the different energies flowing through the test section is presented in Figures 4.5 – 4.7. The figures include the energy balance results for all the heat transfer tests for the different heat exchanger prototypes.

As seen in Figures 4.5-4.7, differences exist between the three energy flows through the test section. The differences in the energy balance can be attributed to many factors such as possible energy losses from the copper spreader and the SS block due to natural convection. Moreover, energy gains from the surrounding air to the heat exchanger are also possible, since the cooling water temperature was 20 °C which was slightly lower than the room temperature which was typically at 23 °C.

The maximum energy balance deviation for all the heat transfer tests was found to be ± 8.3%.

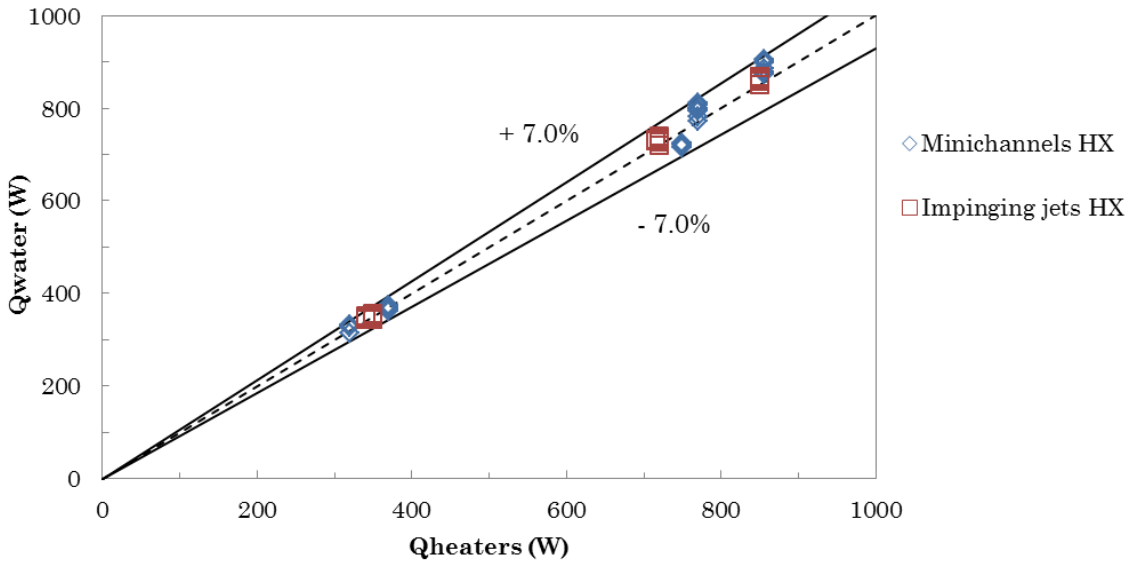

Figure 4.5. Energy balance between the input energy to the test section ($Q_{heaters}$) and the energy removed by water (Q_{water}).

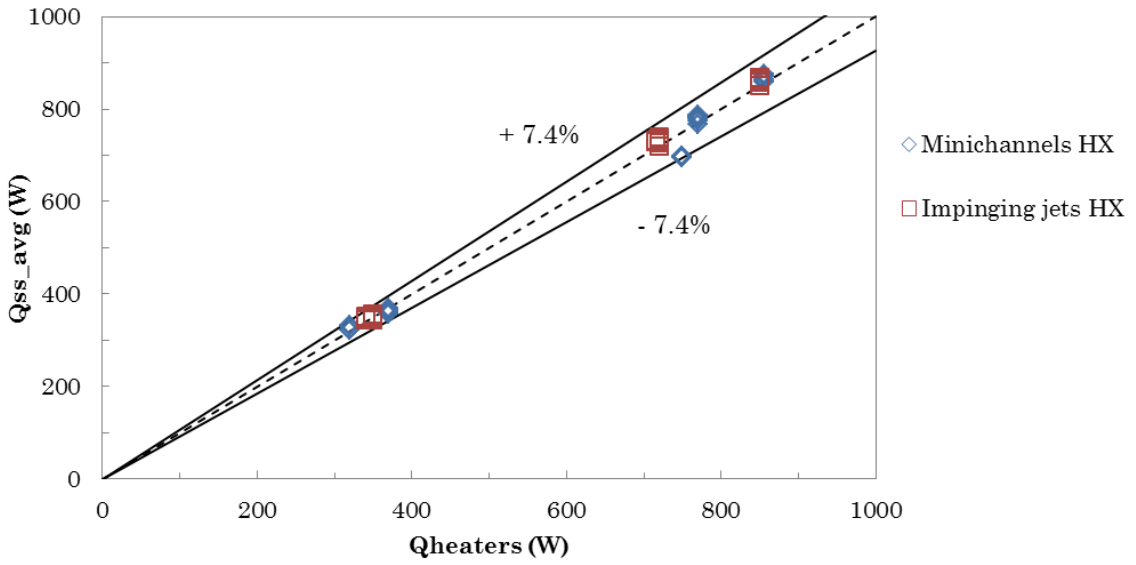

Figure 4.6. Energy balance between the input energy to the test section ($Q_{heaters}$) and energy flow through the SS block (Q_{ss_avg}).

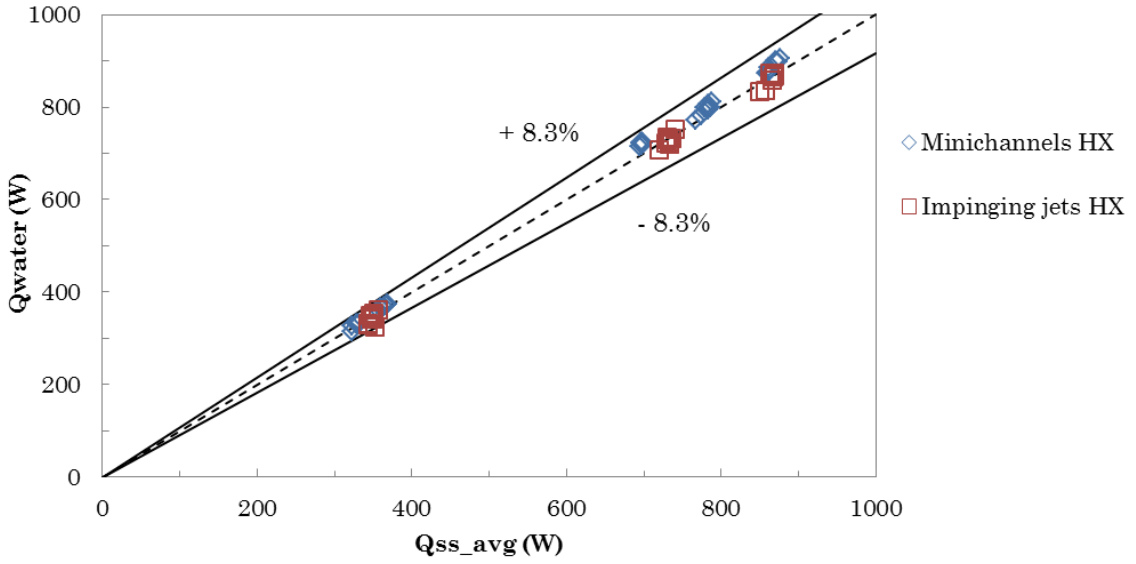

Figure 4.7. Energy balance between the energy flow through the SS block (Q_{ss_avg}) and the energy removed by water (Q_{water}).

4.4. Effect of Clamping Pressure

To ensure the accuracy of the experimental results, the effect of the contact resistance between the SS bock and the heat exchanger prototype must be minimized. This can be achieved by increasing the clamping force applied to the test section. Figure 4.8 shows the effect of increasing the clamping pressure on the temperature at location 4 (T.C 4) located 5 mm from the bottom surface of the SS block. All these tests were performed with $Q_{heaters}$ = 350 W and water mass flow rate $\dot{m}$ = 0.06 kg/s.

For the minichannels heat exchanger, the temperatures remain constant when the applied pressure is greater than 200 kPa, indicating that the effect of the contact resistance is minimized if the clamping pressure is greater than 200 kPa. The temperatures start to increase gradually as the clamping pressure is reduced to values lower than 200 kPa.

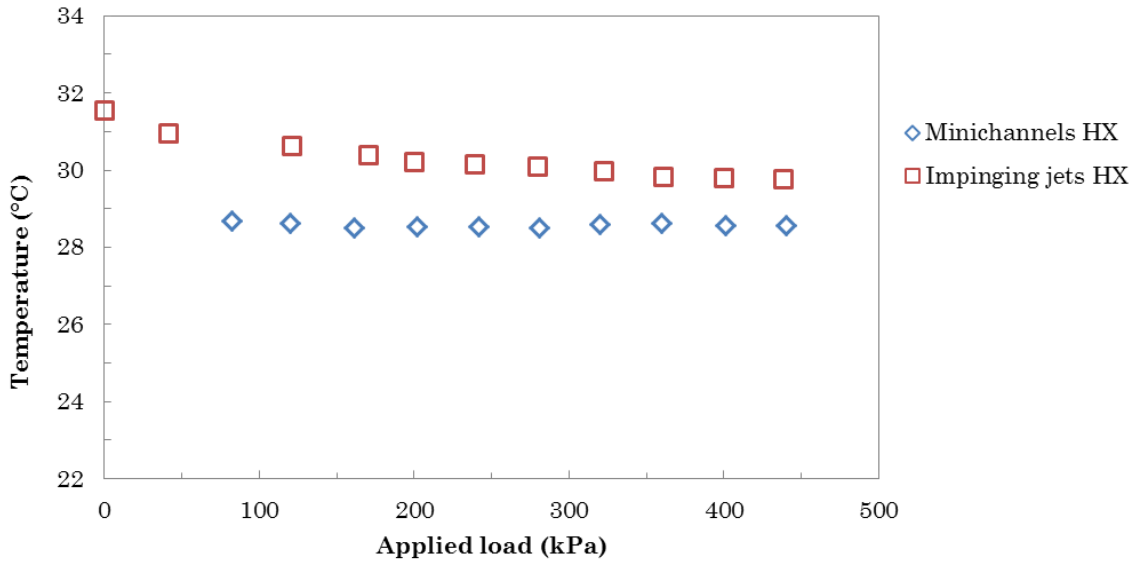

Figure 4.8. The effect of clamping on the temperature T.C. 4 for the tested heat exchanger prototypes.

For the impinging jets heat exchanger, it can be observed that an increase in the clamping force results in a decrease in the surface temperature, due to better contact between the SS block and the heat exchanger surface. However, increasing the clamping pressure beyond 300 kPa results in a little or no effect on the temperatures, which means the effect of the contact resistance, is minimized if the applied clamping pressure is greater than 300 kPa. Also note that the temperatures noticeably increase as the value of the clamping force in reduced to zero.

4.5. Experimental Procedures

Two types of tests were conducted for each heat exchanger, a heat transfer test and a pressure drop test. The cooling loop was equipped with instrumentations to perform both test types. The heat transfer and the pressure drop tests were performed separately to improve the measurement accuracy. Both experimental procedures are presented below.

4.5.1. Experimental Procedure for the Heat Transfer Tests

Before performing the heat transfer tests, the location of the thermocouple fittings, which were used to measure the inlet and the outlet water temperature, were connected as close as possible to the heat exchanger inlet and outlet. The pressure taps were closed and moved further away from the heat exchanger inlet and outlet, since they were not used to measure the pressure drop, refer to Figure 4.9.

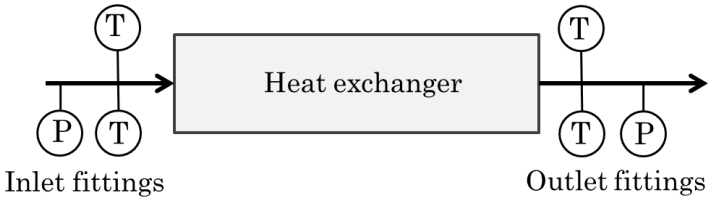

Figure 4.9. A schematic showing the measurement instrumentation setup used for the heat transfer tests.

This particular fitting setup was chosen because it brought the thermocouples closer to the heat exchanger prototype, thus reducing the chance of possible heat gains or losses from the water to the surrounding air. Below are the steps followed when performing the heat transfer tests,

1- The bottom surface of the stainless steel block was cleaned and then a thin (≈ 0.05 mm) layer of thermal paste (Arctic Silver 5) was applied evenly on the surface.

2- The top surface of the heat exchanger was cleaned to remove any dirt, dust and older thermal paste residue. Then the heat exchanger prototype was placed on the test section.

3- The SS block was placed on top of the heat exchanger then clamping pressure of ≈ 410 kPa was applied to the set-up. To ensure that no air gaps were present between the SS block and the heat exchanger surface, the set-up was disassembled to check for air gaps. If air gaps were actually present, then a thin layer of thermal paste was added locally. This step was repeated several times until proper contact between the SS block and the heat exchanger surface was achieved, i.e. no air gaps were present.

4- The heat exchanger prototype was connected to the chilling loop.

5- The desired clamping pressure of ≈ 410 kPa was applied to the test section by turning the threaded nuts. Fine nut adjustments were needed to ensure that the reading from both load cells were approximately equal.

6- Air bubbles were purged from the heat exchanger body by allowing the cooling water to flow at a high flow rate for several minutes.

7- Once all bubbles were purged from the system, the desired water mass flow rate was set using the control valves in the chilling loop. The chiller set point was set to 20 °C.

8- The variable transformer was used to supply appropriate electrical energy to the heaters as required for testing needs. Note that the variable transformer controlled the voltage input to the heaters, the current was dependent on the heater's resistance.

9- The system was allowed to reach steady state working conditions (depending on the test conditions transient time was between 40-80 minutes starting from room temperature).

10- When the system had attained steady state condition, 120 data samples were recorded and saved to a text file.

11- The electrical and the thermal conditions were changed in order to achieve the next desired data point. These caused the system to deviate from steady conditions. Therefore, the procedure was started again from step 6. However the system did not take as long to achieve the new steady state conditions.

4.5.2. Experimental Procedure for the Pressure Drop Tests

Prior to conducting the pressure drop tests the arrangement of the inlet and outlet measurement fittings was modified, such that the pressure taps were located as close as possible to the inlet and outlet bard fittings of the heat exchanger. The fittings holding the thermocouples were moved further away from the pressure taps as seen in Figure 4.10. This configuration was chosen because it prevented measuring the pressure drop associated with the thermocouple yielding a more accurate pressure drop measurement for the heat exchanger.

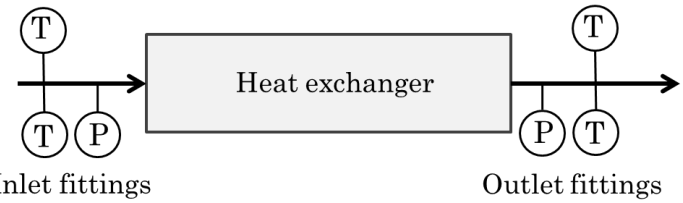

Figure 4.10. A schematic showing the measurements instrumentation used for the pressure drop tests.

The following steps were taken when conducting the pressure drop tests,

1- The differential pressure transducer was connected to the pressure tap before and after the heat exchanger using fixable hoses.

2- Air bubbles were purged from the heat exchanger, pressure hose lines and the pressure transducer body.

3- The temperature of the chiller was set to 20 °C.

4- The desired water mass flow rate was set using the control valves.

5- The system was allowed to stabilize and then the pressure measurements were recorded and saved to text file using the LabView program.

6- Steps 2 and 3 were repeated until the full range of the water flow rates was tested for that particular heat exchanger prototype.

The pressure drop tests took shorter time to perform since the pressure change in the system happened almost instantly.

The pressure drop associated with the inlet and outlet fittings was experimentally measured separately. This was done by removing the heat exchanger, seen in Figure 4.10, such that the inlet and the outlet heat exchanger fitting were connected together in series. The fitting assembly was connected to the cooling loop to measure its pressure drop. The same procedure was used to measure the total pressure drop and the fittings pressure drop for each heat exchanger prototype.

4.6. Uncertainty Analysis

Uncertainty analysis was conducted using the method proposed by Kline and McClintock [82]. The uncertainty analysis calculation steps and the errors associated with each measurement device used in the experimental facility are discussed in detail in Appendix A.

For a measured variable the uncertainty is a result of two components, fixed error (bias error) and a random error (precision error). Bias error is a property of the measurement device. The precision error is a function of the variation of the measured quantity over a period of time. The total uncertainty value, δx_i, is given by the following equation,

$$\delta x_i = \sqrt{(B_i)^2 + (P_i)^2} \tag{4.16}$$

where B_i and P_i are the bias and precision errors respectively. Bias errors were either obtained from documentation provided by the manufacturer or from calibration curves. The calibration curves were established by performing the calibration process in the lab. Precision errors were evaluated statistically using the 95% confidence interval for the 120 samples recorded by the DAQ system for each data point. Bias and precision errors were calculated for the various parameters of each heat exchanger prototype. The results are presented in Table 4.2. Note that $Q_{heaters}$ was not measured using the DAQ system and therefore the precision error associated with it could not be quantified.

The uncertainty of the measured parameters will propagate to the calculated (i.e. dependent) parameters. The uncertainty of such dependent function, R, is estimated by the square root of the sum of the squared uncertainty of each contributing element.

$$\delta R = \sqrt{\sum_{i=1}^{n} \left(\frac{\partial R}{\partial x_i} \, \delta x_i \right)^2} \tag{4.17}$$

where R represents any function that depend on the independent arguments x_1 to x_n.

$$R = f(x_1, x_2, x_3, \ldots, x_n) \tag{4.18}$$

The relative error in R can be found by dividing the uncertainty in the measurement δR by the value of the measurement as shown below.

$$\frac{\delta R}{R} = \sqrt{\sum_{i=1}^{n} \left(\frac{\delta x_i}{x_i}\right)^2} \tag{4.19}$$

Table 4.2. Maximum relative uncertainties for the calculated parameters for the three different heat exchanger prototypes.

Calculated parameter	Maximum relative error	
	Minichannels heat exchanger	Impinging jets heat exchanger
$\dot{m}$ (kg/s) (@ 0.01 kg/s)	± 2%	± 2%
ΔP (kPa)	± 21.1% (@ 0.479 kPa)	± 12.7% (@ 0.797 kPa)
Energy transferred to the water, Q_{water} (W)	± 11.3%	± 11.6%
Log-mean temperature difference, ΔT_{LM_CL} (°C)	± 11.8%	± 10.2%
Thermal conductance, hA (W/K)	± 13.8%	± 15.5%
Heat transfer coefficient, h (W/m^2·K)	± 13.9%	± 16.0%
Nusselt number, Nu	± 14%	± 16.3%
Reynolds number, Re	± 7.6%	± 8.3%
Pumping power, P_p (W)	± 20.3%	± 12.7%

5. Results and Discussion

In this chapter the results of the heat transfer and pressure drop experiments will be presented and discussed.

5.1. Experimental Results for the Minichannels Heat Exchanger

5.1.1. Heat Transfer Results

The experimental Nusselt numbers for the minichannels heat exchanger are plotted in Figure 5.1 against the Reynolds number; which is based on the D_h of a single minichannel. In general, it is observed that as the Reynolds number increases the Nusselt number increases. In addition, a clear change in slope can be observed at around $Re \approx 150$ and 1000. Therefore Figure 5.1 is divided to three regions, Region 1 is located below $Re \lesssim 150$. In this region, the Nu does not seem to be changing noticeably as Re increases. In Region 2, $150 < Re < 1000$, Nu increases as Re increases. Region 3 is the region where $Re \gtrsim 1000$ in which the Nu increases increase at a faster rate compared to Region 2.

To explain these observations, the thermal and hydrodynamic entrance lengths were calculated to identify the flow regimes inside the minichannel. The hydrodynamic and the thermal entry lengths for laminar flow regimes are given by Eqn. 5.1 and 5.2 respectively (from [20]).

$$L_{hy} \approx 0.0575\, Re_D D \tag{5.1}$$

$$L_{th} \approx 0.0575\, Re_D PrD \tag{5.2}$$

For Region 1, entry hydrodynamic entrance length over the minichannel length (L_{hy}/L_{ch}) were found to be between 4% and 8%. Whereas the thermal entry length over the minichannel length (L_{th}/L_{ch}) was 24.6% and 49% respectively. Therefore, the data points in Region 1 are considered

to be hydrodynamically developed but thermally developing flow regime. All the water properties and the Pr were evaluated at the average water temperature.

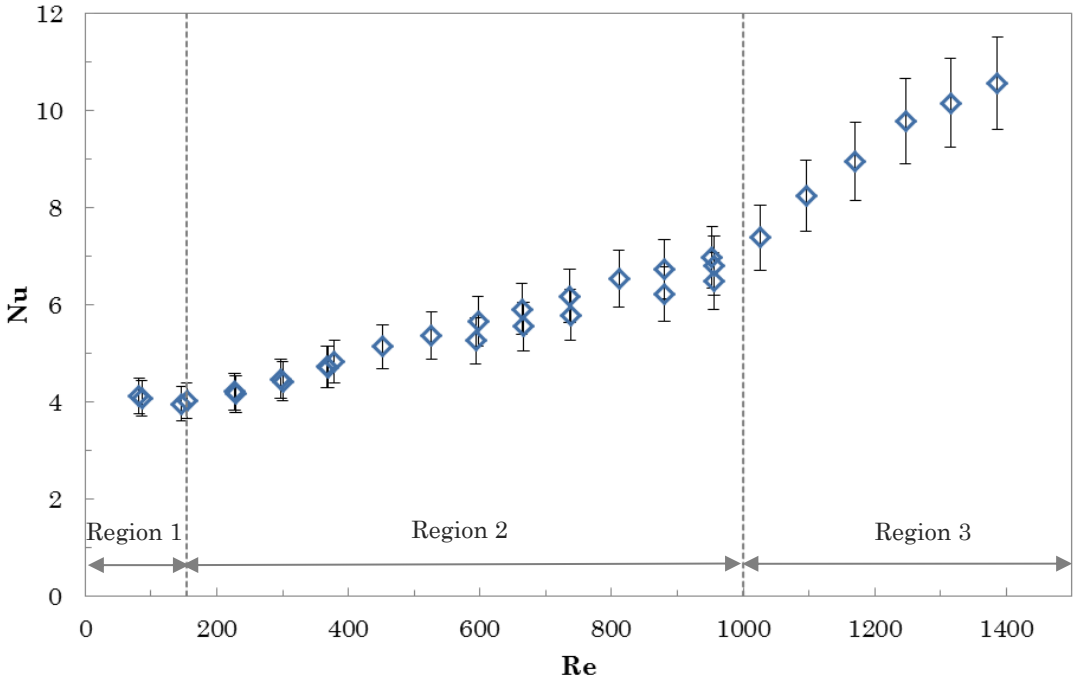

Figure 5.1. Experimental average Nu numbers obtained for the minichannels Heat exchanger as a function of the minichannel Re.

The experimental results are compared with conventional flow correlations in Figure 5.2. Region 1 results are compared to the fully developed Nu number of circular tubes which is 3.66 for uniform surface temperature boundary condition [20]. In addition, the data in Region 1 are also compared with the fully developed Nu of square-channel, with three heated sides, which is 3 for a constant surface temperature boundary condition [51]. Figure 5.2 shows the comparison of the fully developed Nusselt in Region 1 with the fully developed conventional flow Nusselt numbers. The experimentally obtained Nu in region 1 is about 4 which is higher than the fully developed Nusselt numbers. This behavior is expected

since the thermal boundary layer is still developing for a significant portion of the minichannel resulting in higher Nu.

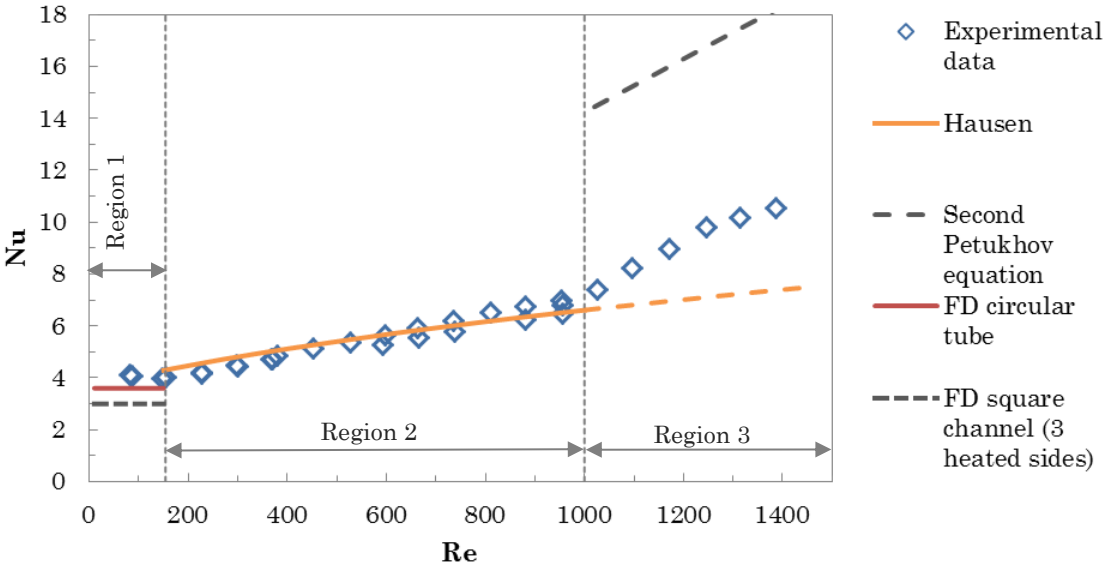

Figure 5.2. Average Nusselt numbers for the minichannels heat exchanger compared with conventional flow correlations.

It is expected that the data points located at Re = 154 have a higher Nu compared to the data points located at Re = 81 because the thermal developing length is smaller (L_{th}/L_{ch} =24.6% to 49%). However, the experimental results do not clearly show this trend. Instead, the Nu at Re at 28 and 154 are ≈ 4. The Hausen correlation (Eqn. 2.3) estimated the theoretical Nu which to be 4.0 and 4.3 at Re 81 and 154, respectively. The maximum difference between the experimental and theoretical Nu (in Region 1) is 7% which is within the experimental uncertainty of the experiments which were about 10%.

In Region 2, depicted in Figure 5.1, it is observed that as Re increases Nu increases. The Reynolds number is between 154 and 1000, L_{hy}/L_{ch} ranged from 8% to 57% while L_{th}/L_{ch} varied from 49% to 347%. Thus, in Region 2, the flow regime inside the minichannel is considered to be thermally and

hydrodynamically developing (simultaneously developing) flow. For simultaneously developing flows the Nusselt number increases as Reynolds increases. In Figure 5.2, the experimental data in Region 2 are compared with the Hausen correlation (Eqn. 2.3) which is applicable for simultaneously developing flow. The Hausen correlation agrees very well with the experimental Nusselt numbers obtained. Therefore it can be used to predict the performance of the minichannels heat exchanger in the when operating in the simultaneously developing flow regime.

Region 3 seen Figure 5.1, shows that for $Re \gtrsim 1000$ Nu increases more rapidly compared to the other regions. The rapid increase in the Nusselt numbers is believed to be the result of early transition from laminar flow conditions inside the minichannel. A small but noticeable change in slope of the curve can be noticed at $Re \approx 1000$ indicating that the flow regime inside the minichannel is starting to transition from laminar conditions.

For circular tubes with a rounded inlet section, uniform velocity profile and steady state entry flow, the critical Reynolds number is 2300 [20]. The critical Re observed for the minichannel is lower than the critical Reynolds number for circular tubes. Early transition from laminar flow conditions in minichannels and microchannels is affected by the inlet manifold design [36] and channel roughness [83]. Geometrical parameters such as hydraulic diameter, ratio of channel height to channel width and channel centre to centre spacing, also have a significant influence on the flow regimes and heat transfer [47]. The early transition from laminar flow conditions inside minichannels and microchannels was also observed by several investigators. For instance, Harms et al. [36] found that the transition Re was around 1500, Roa and Khandekar [84] found the critical Re to occur between 800 to 1500. Moharna et al. [53] observed that the laminar to turbulence transition

commenced at $Re \approx 1500$, Pfund et al. [50] found that the transition from laminar flow conditions occurred at Reynolds numbers between 1700 to 2000.

Experimental Nusselt numbers for minichannels and microchannels in the turbulent flow regimes are frequently compared to Gnielinski's correlations given by (adapted from [54]).

$$Nu_D = \frac{(f/8)(Re_D - 1000)Pr}{1 + 12.7(f/8)^{1/2}(Pr^{2/3} - 1)} \tag{5.3}$$

However, since the critical Reynolds number for the minichannels was 1000 the correlation could not be used. At Re values around 1000 the term $(Re_D - 1000)$ would be small, leading to unrealistic Nusselt numbers. Hence, the correlation could not be used for comparing the data. The experimental data are compared with the second Petukhov equation which is applicable for $10^4 \leq Re \leq 5 \times 10^6$ extrapolated down to $Re \approx 1000$.

$$Nu_D = \frac{(f/8)(Re_D)Pr}{1.07 + 12.7(f/8)^{1/2}(Pr^{2/3} - 1)} \tag{5.4}$$

In addition, the Hausen correlation is extended into Region 3 in order to compare it with the experimental Nusselt numbers. The extrapolated portion of the correlation is shown by the dashed line in Figure 5.2.

Figure 5.2 shows that the experimental data are higher than the Nu values predicted by the Hausen correlation. The Hausen correlation is able to predict the Nu in the laminar flow. However in Region 3 the transition from laminar flow conditions occurs leading to higher Nu compared to the laminar flow regimes (Regions 1 and 2). In addition, the experimental Nu are lower compared to the second Petukhov correlation which is capable of predicting the Nu in the turbulent flow for a circular tube. It is expected that the experimental Nu would be lower because the flow conditions inside the minichannels are not fully turbulent. Instead they could be in the transitional flow regime. Note the second Petukhov equation is being used outside its range in this case.

5.1.2. Pressure Drop Results

The coolant flow path inside the minichannels heat exchanger is illustrated in Figure 5.3. The total pressure drop for the minichannels heat exchanger can be divided to following components,

$$\Delta P_{total} = \Delta P_{fittings} + \Delta P_{ports} + \Delta P_{ch} + \Delta P_{friction} \quad (5.5)$$

where:

- ΔP_{total} and $\Delta P_{fittings}$ are the total pressure drop and the pressure losses due to the inlet and outlet fittings. Both quantities were experimentally measured.
- ΔP_{ports} is the summation of the pressure drop due to the inlet/outlet ports. The inlet/outlet ports are threaded holes machined in the minichannels heat exchanger body. Refer to Figure 3.5 for details regarding port the location and size.
- ΔP_{ch} is the pressure drop associated sudden contraction an expansion at the minichannel inlet and outlet respectively.
- $\Delta P_{friction}$ is the pressure drop due to wall friction and it is equal to $f \frac{L_{ch}}{D_h} \frac{\rho V_{ch}^2}{2}$.

For the minichannels heat exchanger, it is desired to calculate the friction factor for a single minichannel and compare it to appropriate conventional friction factor correlations for each flow regime. In order to calculate the friction factor the values of ΔP_{ports} and ΔP_{ch} (in Eqn. 5.5) must be calculated first.

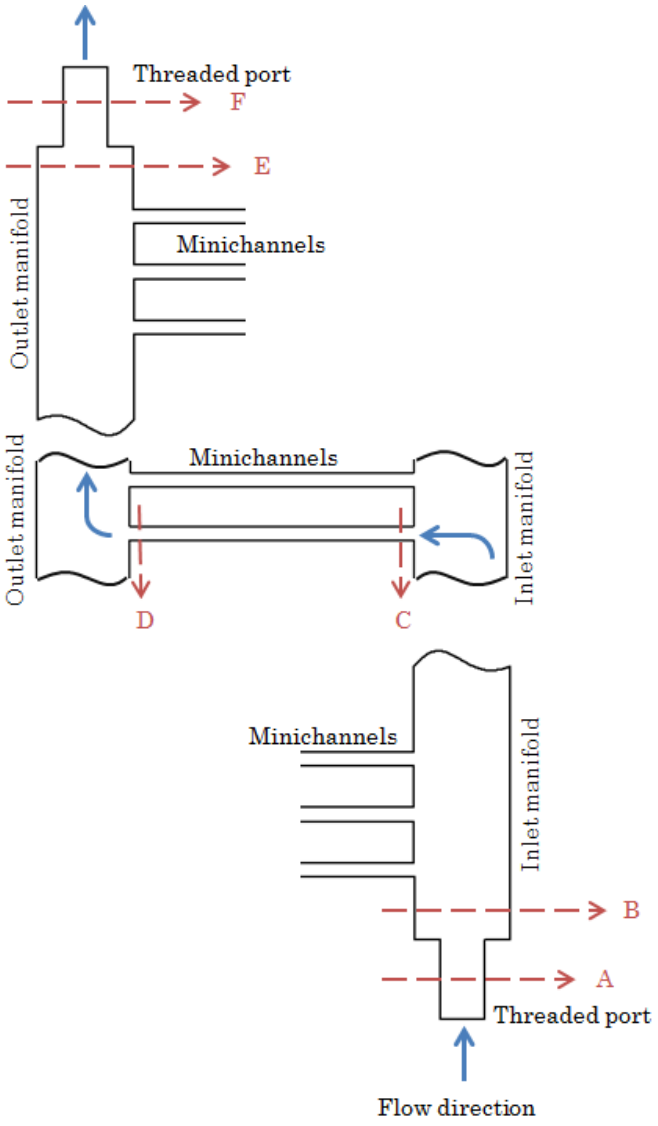

Figure 5.3. Coolant flow path inside the minichannels heat exchanger.

To calculate the values of ΔP_{ports} and ΔP_{ch}, the associated loss coefficients are dependent on the sudden expansion and contraction in the flow path which must be evaluated. The area ratios and the loss coefficient associated with each sudden expansion and contraction (Figure 5.3) were calculated. The results are presented in Table 5.1. Note that the loss coefficients K_c and K_e were obtained using Figure 3.2.

Table 5.1. The area ratios and the corresponding loss coefficients associated with the various expansions and contractions in the Minichannels heat exchanger.

Cross section area	Area value (mm^2)	Area ratio, location	Loss coefficient	flow velocity used
A_A	90.56	A_A/A_B = 0.226, inlet port	K_e=0.6	V_A
A_B	400			
A_C	1	$A_c/A_{manifold} \approx 0$, channel inlet	K_c=0.5	V_{ch}
$A_{manifold}$	>>1			
A_D	1	$A_C/A_{manifold} \approx 0$, channel outlet	K_e=1	V_{ch}
$A_{manifold}$	>>1			
A_E	400	$A_F/A_E \approx 0.226$, outlet port	K_c=0.4	V_F
A_F	95.56			

The pressure drop associated with the inlet/outlet ports (ΔP_{ports}) is given by,

$$\Delta P_{ports} = \left(K_e \frac{\rho_w V_A^2}{2}\right)_{inlet\ port} + \left(K_c \frac{\rho_w V_F^2}{2}\right)_{outlet\ port} \quad (5.6)$$

Based on the area ratio K_e and $K_c$were found to be 0.6 and 0.4, respectively (refer to Table 5.1). Using these loss coefficients in Eqn. 5.6 and noting that $V_A = V_F$, Eqn. 5.6 becomes,

$$\Delta P_{ports} = \frac{\rho_w V_A^2}{2} \quad (5.7)$$

Likewise, the pressure drop associated with the inlet and outlet of a minichannel (ΔP_{ch}) is given by,

$$\Delta P_{ch} = \left(K_c \frac{\rho_w V_{ch}^2}{2}\right)_{channel\ inlet} + \left(K_e \frac{\rho_w V_{ch}^2}{2}\right)_{channel\ outlet} \quad (5.8)$$

where K_c and K_e were found to be 0.5 and 1, respectively based on the area ratios given in Table 5.1. Using the calculated loss coefficients in Eqn. 5.8, ΔP_{ch} becomes,

$$\Delta P_{ch} = 1.5 \frac{\rho_w {V_{ch}}^2}{2} \quad (5.9)$$

Using the estimations of ΔP_{ch} and ΔP_{ports} in Eqn. 5.5, the Darcy friction factors for a minichannel can be calculated by,

$$f = \frac{D_h}{L_{ch}} \frac{2}{V_{ch}^2} \left[\frac{\left(\Delta P_{total} - \Delta P_{fittings}\right)}{\rho_w} - \frac{1 * V_{ports}^2}{2} - \frac{1.5 * V_{ch}^2}{2} \right] \qquad (5.10)$$

Experimental friction factors were calculated and compared with appropriate conventional correlation. For the simultaneously developing laminar flow regime, the apparent friction factor, f_{app}, should be used because it combined the effects of wall shear and the pressure drop associated with the developing velocity profile. The experimental friction factor results are compared to the correlation developed by Shah [58] given in Eqn. 5.11 for β = 1. The different constants in the correlation were previously determined and discussed (for β = 1) in Section 3.1.1.

$$f_{app} = 4 \left[\frac{3.44}{Re\sqrt{L^*}} + \frac{14.227 + \frac{1.43}{4L^*} - \frac{3.44}{\sqrt{L^*}}}{Re\left(1 + \frac{0.00029}{L^{*2}}\right)} \right] \qquad (5.11)$$

In addition, the experimental friction factors, in the laminar flow regime, are also compared to the fully developed laminar friction factors for a square channels (from [20]) given by,

$$f = \frac{56.92}{Re} \qquad (5.12)$$

The experimental friction factors in Region 3 are compared to the Blasius equation (adapted from [60]) applicable for $Re \leq 10^5$.

$$f = \frac{0.316}{Re^{0.25}} \qquad (5.13)$$

The experimental friction factors are plotted and compared with conventional correlations in Figure 5.4. For Re < 700, the friction factors are lower than what is predicted by correlations. This behavior could be linked to the estimation of loss coefficients in Eqn. 5.6 and Eqn. 5.8. Examining Eqn. 5.10, it can be concluded that if ΔP_{ports} and ΔP_{ch} are overestimated, $\Delta P_{friction}$

would decrease resulting in lower f values. One possible cause of overestimating ΔP_{ports} and ΔP_{ch} could be the expansion and contraction loss coefficients being different than they should at low Reynolds numbers. For Re > 700, the experimental data agrees well with the frictions factors predicted by conventional laminar and turbulent correlations.

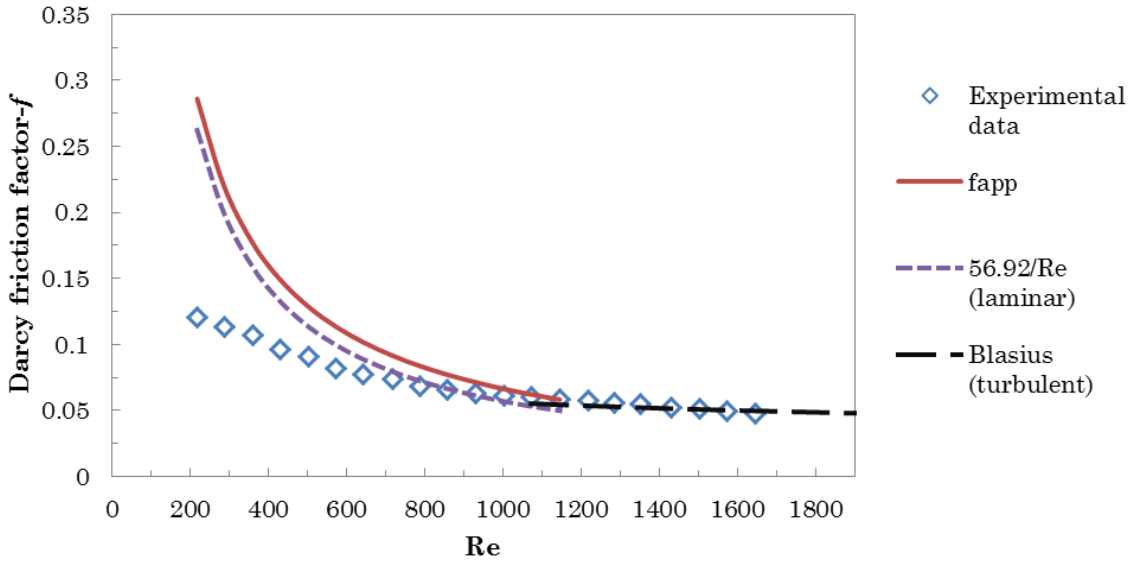

Figure 5.4. Experimental friction factors for the minichannels heat exchanger compared to conventional friction factors correlations.

The total pressure drop and the pressure drop associated with the inlet and outlet fittings were experimentally measured. The results are plotted in Figure 5.5 as a function of the minichannel Re and total mass flow rate through the heat exchanger ($\dot{m}$). The calculated values of the ports pressure drop and the minichannel inlet/outlet are also plotted in Figure 5.5. From Figure 5.5, it can be noticed that as the mass flow rate increases, all the different pressure drops plotted increase as well. On average, pressure drop associated with the inlet/outlet fitting accounted for 50% of the total pressure. The pressure drop associated with the inlet/outlet ports and the minichannels inlet and outlet accounts for 12% and 7% of the total heat

exchanger pressure drop, respectively. The pressure drop associated with fittings is higher compared to the other pressure drop sources and it accounts for 50% of the total pressure drop in the minichannels heat exchanger. Therefore there is a potential for reducing the total pressure drop for the minichannels heat exchanger if better inlet/outlet fitting design is developed.

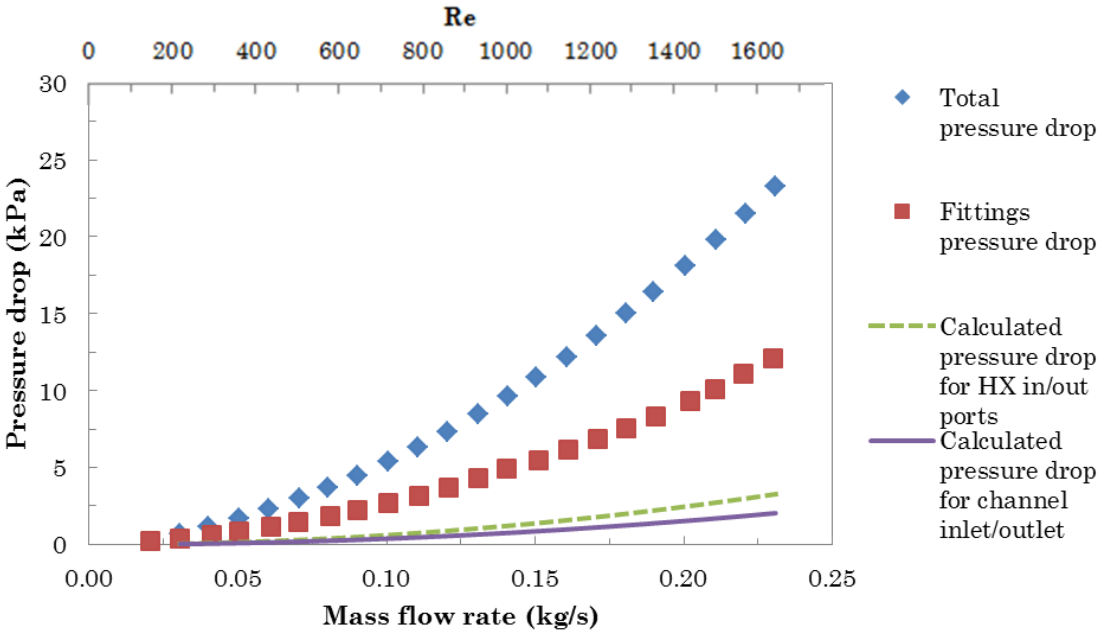

Figure 5.5. Measured and calculated pressure drop values for the minichannels heat exchanger.

To exclude the effects of the fittings on pressure drop and get better assessment on the frictional losses inside the minichannels heat exchanger, a heat exchanger loss coefficient, K_{HX}, can be defined as,

$$K_{HX} = \left(\frac{2}{V_{inlet}^2}\right)\left(\frac{\Delta P_{total} - \Delta P_{fittings}}{\rho}\right) \qquad (5.14)$$

This definition was chosen in order to account for all the pressure losses within the heat exchanger. V_{inlet} is the fluid velocity in the cooling loop hose (i.e. before the inlet heat exchanger fitting). K_{HX} for the minichannels heat exchanger is plotted versus the minichannel Re in Figure 5.6

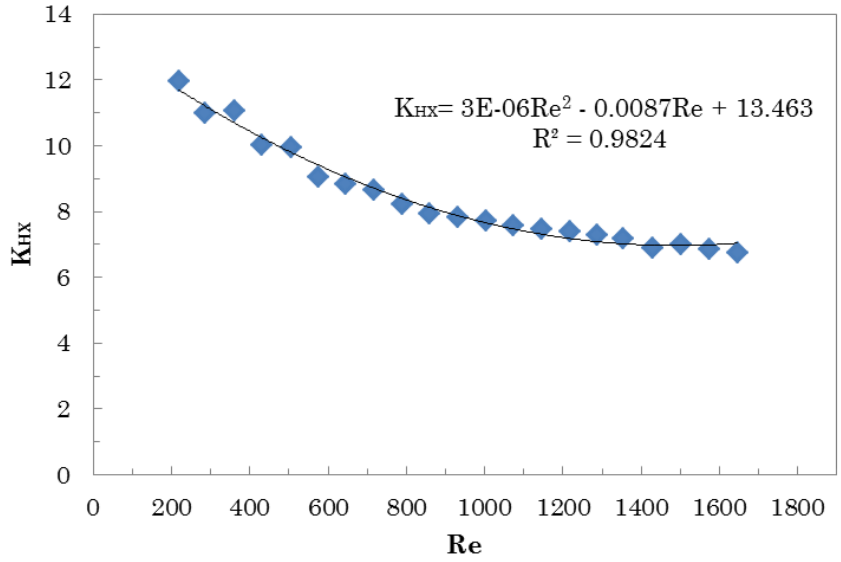

Figure 5.6. Heat exchanger loss coefficient, K_{HX}, for the minichannels heat exchanger.

In general, the loss coefficient decreases as the Reynolds number increases. A change in the slope occurs at Re around 1000. The slope of the curve for $Re < 1000$ is steeper compared to the slope for $Re > 1000$. This observation seems to be consistent with the thermal analysis which indicated that the transition from laminar flow condition occurred at $Re \approx 1000$. For $Re > 1400$ K_{HX} decreases gradually and it seems to be reaching a constant value of approximately 7. The experimental values of K_{HX} were fitted using a correlation given by $K_{HX} = 3 \times 10^{-3} Re^2 - 0.0087 Re + 13.463$.

5.2. Experimental Results for the Impinging Jets Heat Exchanger

5.2.1. Heat Transfer Results

The average Nusselt numbers for the impinging jets heat exchanger are plotted in Figure 5.7 as a function of the jet Reynolds number (based on D_j). The figure shows that the Nusselt number increases as the Reynolds number

increases. Higher Reynolds numbers result in an increase in the jet velocity which leads to better heat transfer performance. The effect of increasing Re on the increase of Nu number is less significant for $Re > 2000$. This is can be attributed to the transition from laminar flow conditions which agree with the results of Elison and Webb [66].

At around $Re \approx 2000$, some experimental data points are slightly lower. This is believed to be due to the repeatability associated with the day-to-day operations. However, the effect of the repeatability is within the limits of experimental error.

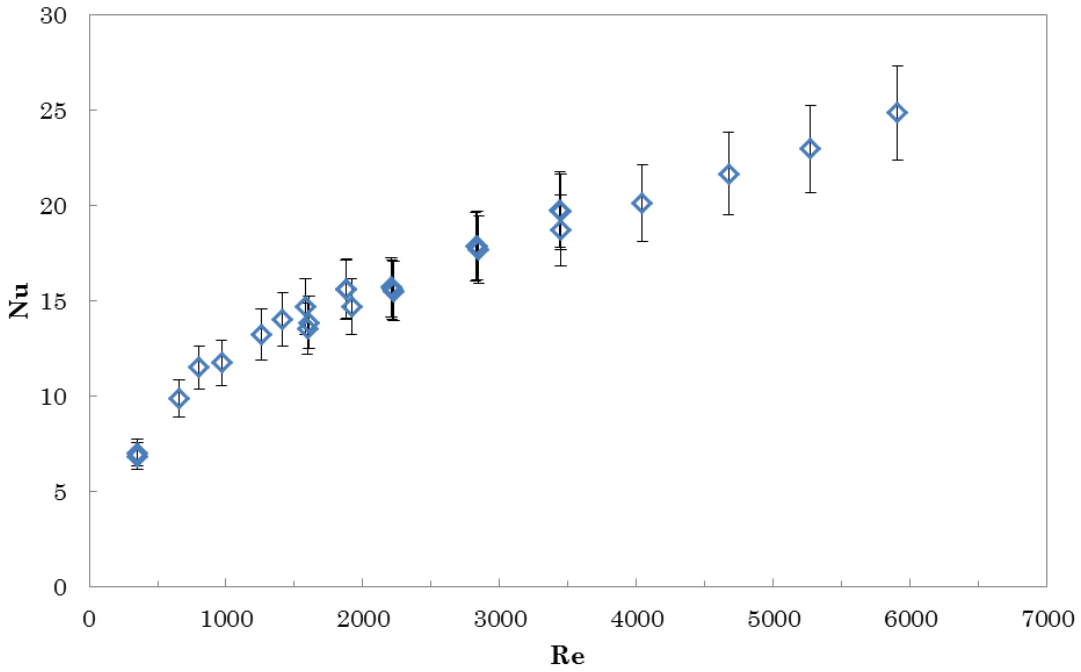

Figure 5.7. Average Nusselt number as a function of the jets Re for the impinging jets heat exchanger.

A correlation for predicting the averaged Nusselt numbers for a single water jet, impinging vertically on a horizontal flat surface, was developed by Sitheramayya and Raju [70] as presented in Table 2.2. The correlation was selected because it is valid for $2000 < Re < 40000$ which covers a good portion

of the experimental results. In addition, jet parameters such as H/D_j and d_h/D_j are 1.67 and 14 which are well within the correlation limits given in Table 2.2.

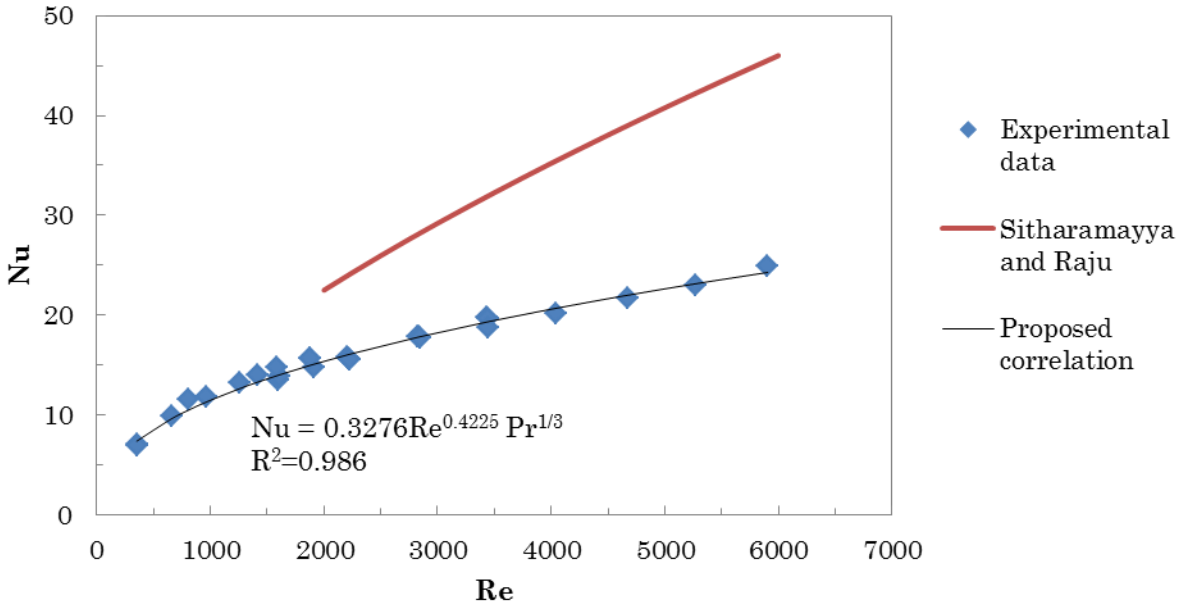

Figure 5.8. Average Nusselt number for the impinging jets heat exchanger as a function of the jet Re.

Figure 5.8 indicates that experimental Nusselt numbers are, on average, 44% lower than the Nusselt number predicted by the Sitheramayya and Raju correlation. One possible reason for the deviation could be the jet flow direction inside the impinging jets heat exchanger compared to the jet flow for the jet used to obtain the correlation. These flow directions are schematically illustrated in Figure 5.9. The experimental Nusselt numbers for the liquid jets (utilized by the impinging jets heat exchanger) were correlated by Eqn. 5.15. The proposed jet correlation is plotted in Figure 5.8.

$$Nu = 0.3276Re^{0.4225}Pr^{1/3} \qquad (5.15)$$

For the impinging jets heat exchanger, each jet nozzle was constrained by solid walls from two sides (i.e. wall-confined). Therefore, the fluid

emerging from the jet nozzle was forced to migrate towards the outlet and not in the radial direction (Figure 5.9 A). The presence of the walls altered the flow which affected the heat transfer performance of the jet.

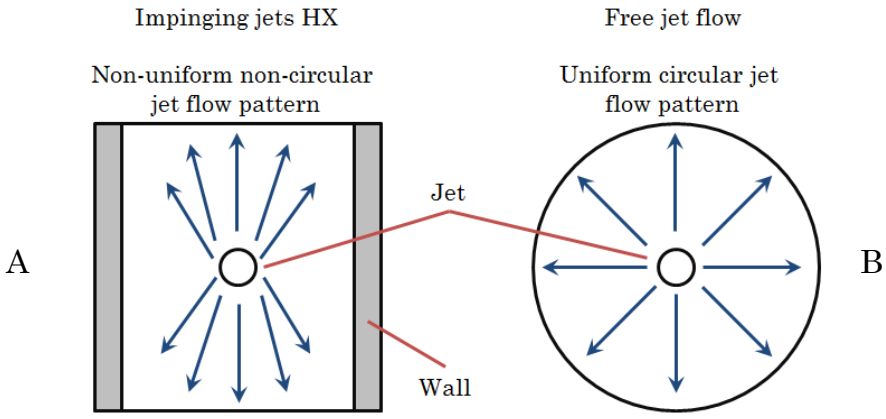

Figure 5.9. A schematic illustrating the flow direction of the impinging jets heat exchanger (A), (B) the flow direction for jet used to derive the Sitheramayya and Raju correlation (B) (top view).

As illustrated in Figure 5.9 (B), the liquid jets used to develop the correlation were not surrounded by walls. Therefore, the fluid exiting the jet orifice flowed uniformly in all directions, yielding better heat transfer performance when compared to the wall-confined jets implemented in the impinging jets heat exchanger. It is known that the presence of a wall affects the jet heat transfer due to the alteration of the flow field. The experimental results of Shoukri and Kalka [85] indicated that wall constrained impinging jets are less capable of heat dissipation compared to free (unconstrained) jets. The presence of the constrained wall induced backward rotational flow which lowered the jet's momentum and width. Also, the development of the boundary layer was slowed down due to the presence of the constrained wall. The combined effects of the former factors are believed to lower Nusselt numbers for the constrained jet.

Figure 5.8 does not mean that liquid jets have inadequate heat transfer performance and should not be used in designing cooling heat exchangers. Instead Figure 5.8 illustrates that the impinging jets heat exchanger design is not thermally performing as expected. There is a potential for improving the impinging jets heat exchanger design by making design changes. The design changes could include modifying the design of the support ribs in order to reduce their effect on the jet performance or possibly using two jets positioned closer to the walls instead of a single jet at the centre.

5.5.2. Pressure Drop Results

The total pressure drop and the inlet/outlet fittings pressure drop for the impinging jets heat exchangers were measured experimentally. The setup used for measuring the total pressure drop is shown in Figure 5.10. The impinging jets heat exchanger had 2 inlet and 3 outlet paths. This fitting configuration is denoted as the (2-3) configuration. Removing the heat exchanger was necessary for measuring the inlet and outlet fittings pressure drop. However, upon the removal of the heat exchanger, the inlet and outlet fittings could not be connected together directly since the inlet fittings has 2 flow paths and the outlet fittings has 3 flow paths.

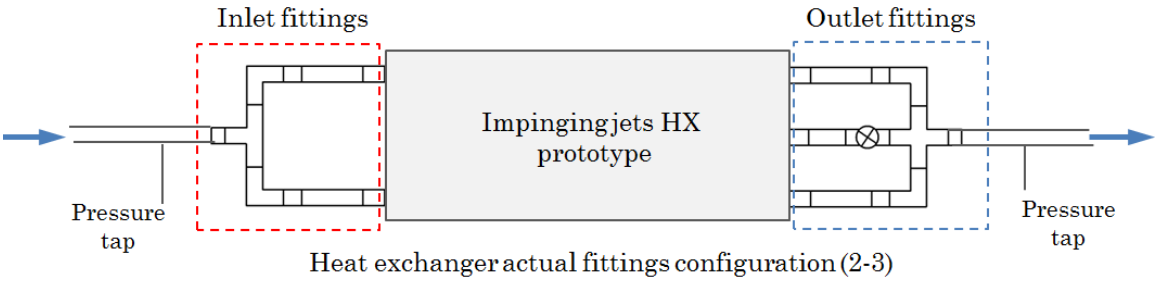

Figure 5.10. A schematic drawing illustrating how the total pressure drop for the imping jets heat exchanger was measured.

The fitting losses for the (2-3) configuration were calculated by averaging the experimentally measured fitting losses for the (2-2) configuration and (3-3) configuration. The (2-2) and (3-3) fitting configurations are schematically shown in Figure 5.11. The calculated fitting pressure drop for the (2-3) configuration and the total pressure drop are plotted in Figure 5.12 as a function of the mass flow rate through the heat exchanger.

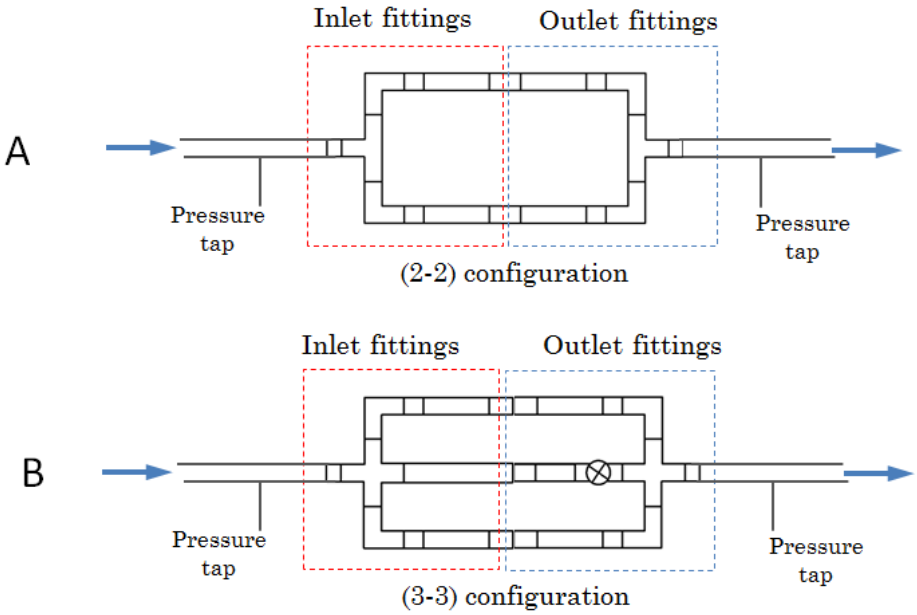

Figure 5.11. A schematic drawing depicting the (2-2) fitting configuration (A), and (B) the (3-3) fitting configuration.

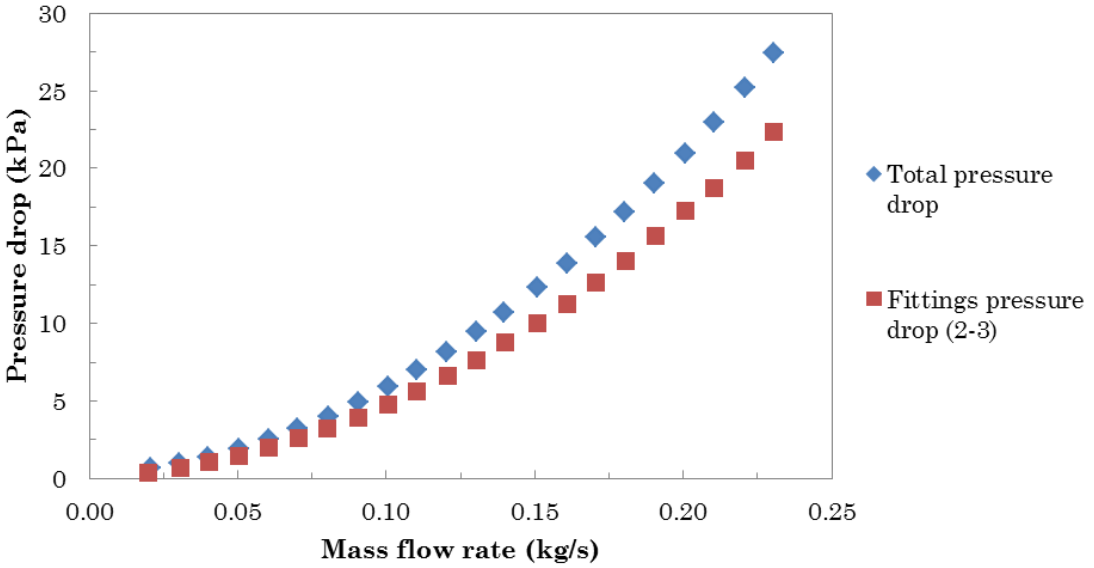

Figure 5.12. The total pressure drop for the impinging jets heat exchanger compared to the inlet/outlet fittings pressure losses.

As expected, the pressure drop increases as the mass flow rate flowing through the heat exchanger increases. On average, approximately 80% of the total pressure is attributed to fitting losses which is quite significant. At $\dot{m} <$ 0.1 kg/s, the total pressure drop is mainly due to the inlet/outlet fittings losses. The total heat exchanger pressure drop will decrease significantly if the fittings losses were to decrease. The fitting losses can be reduced by making design changes. For instant, using larger diameter fittings, if possible, could reduce the fittings losses due to the decrease in the flow velocity in the fittings.

Unlike the minichannels heat exchanger, the flow path inside the impinging jets heat exchanger was complex due to the several design features machined in the heat exchanger body, refer to Figures 3.9 – 3.10. Therefore, accurately estimating the pressure drop due to the inlet/outlet manifolds, jets, wall friction was difficult. However, the total pressure drop can be simply divided into the following components,

$$\Delta P_{total} = \Delta P_{fittings\,(2-3)} + \left(K_{HX} \frac{\rho_w V_{inlet}^2}{2} \right) \qquad (5.16)$$

where the term K_{HX} accounts for the different pressure losses within the impinging jets heat exchanger. The heat exchanger loss coefficient was calculated and values are plotted in Figure 5.13 against the jet Reynolds number.

The curve of K_{HX} can be divided into two regions. In the first region, K_{HX} decreases noticeably as Re increases. This region is characterized by Re < 3000. The values of K_{HX} inside the former region could be laminar as they decrease as the Re increases. The curve then changes slope around Re = 3000 and it becomes more flat. For Re > 3000, the values of K_{HX} remain relatively constant and reach a steady state values of 3 as Re increases. For turbulent flow regime, it is known that the loss coefficients are nearly constant. Therefore, the constant values of K_{HX} for Re > 3000 are likely to be the result of a turbulent flow conditions inside the impinging jets heat exchanger.

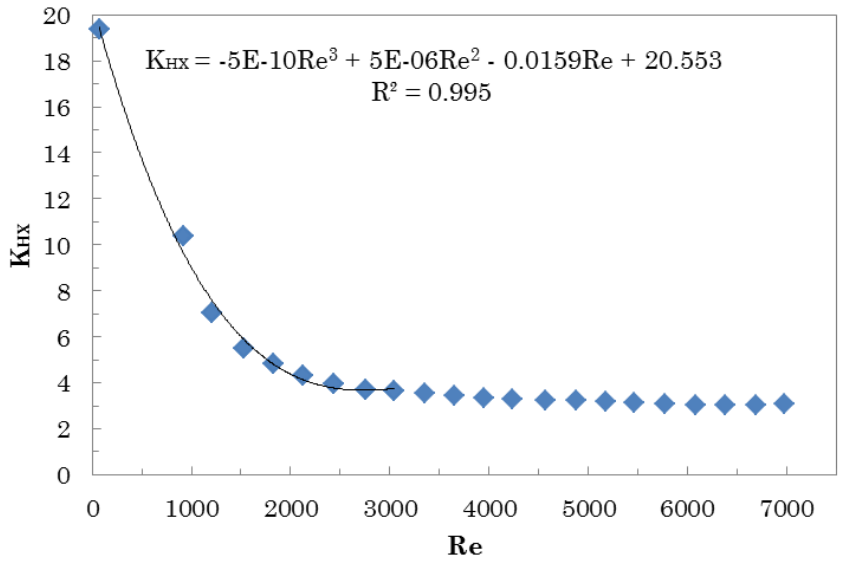

Figure 5.13. Heat exchanger loss coefficient, K_{HX}, for the impinging jets heat exchanger.

Since the transition in the K_{HX} occurs at $Re \approx 3000$, the transition is not believed to be caused by the jet transition from laminar flow conditions which normally occur at $Re \approx 2000$ [66]. Another explanation could be that the flows in the inlet manifolds (seen in Figure 3.10) could be turbulent. To investigate this claim the manifold Re must be calculated. At jet Re = 3000 the $\dot{m}$ through the heat exchanger is 0.1 kg/s, which means that the $\dot{m}$ per manifold is 0.05 kg/s. For $\dot{m}$ = 0.05 kg/s, the inlet manifold (rectangular geometry with D_h=18.4 mm) Re is 2672 which is above the critical Re for circular tube which is 2300 [20]. Therefore, for a jet Re > 3000 (Figure 5.13) the flow inside the inlet manifold has transitioned from laminar flow conditions causing the K_{HX} to remain relatively constant. For jet Re < 3000, the flow in the inlet manifolds is laminar causing the K_{HX} to decrease as jet Re increases. In this range, the values of K_{HX} are correlated by $K_{HX} = -5 \times 10^{-10}Re^3 + 5 \times 10^{-6}Re^2 - 0.0159Re + 20.553$.

5.3. Comparing the Thermal and Hydrodynamic Performance for both Heat Exchanger Designs

In this section, the thermal and hydrodynamic performance of both heat exchanger designs is compared to each other to determine which heat exchanger design has better overall performance.

5.3.1. Comparing the Thermal Performance

The Nusselt numbers for the tested heat exchanger prototypes are plotted against the Reynolds number in Figure 5.14. The Re for the minichannels heat exchanger is based on the hydraulic diameter (D_h), while it is based on the jet diameter (D_j) for the impinging jets heat exchanger.

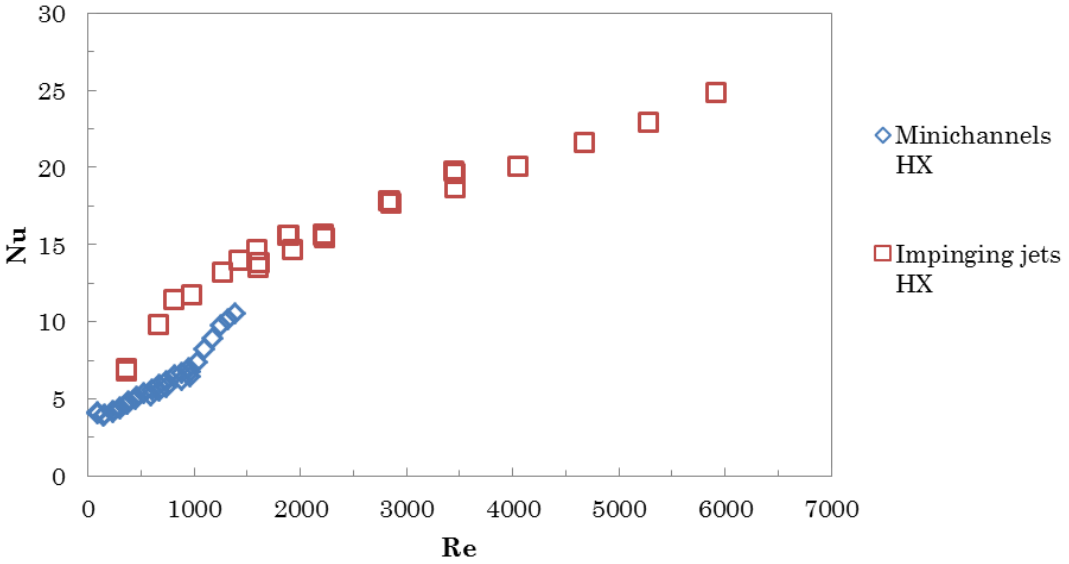

Figure 5.14. Comparing the Nusselt number results for different heat exchanger prototypes.

In general, the Nusselt numbers for the minichannels heat exchanger are lower when compared to the jets heat exchanger. However, it should be noted that Nusselt numbers and Reynolds numbers cannot be used for comparing the different heat exchanger prototypes because they are both dependent on different characteristic lengths (either D_h or D_j). In addition, there are 140 minichannels in the minichannels heat exchanger compared to 14 jets in the impinging jets heat exchanger. Therefore at a given coolant mass flow rate the flow velocity for a single minichannel will be smaller compared to the jet flow velocity. The leads to lower minichannel Reynold numbers (Figure 5.14). For better comparison between the two heat exchanger prototypes, the heat transfer coefficient (h) and the thermal conductance (hA) as a function of the coolant mass flow rates through the heat exchanger are plotted in Figures 5.15 – 5.16, respectively.

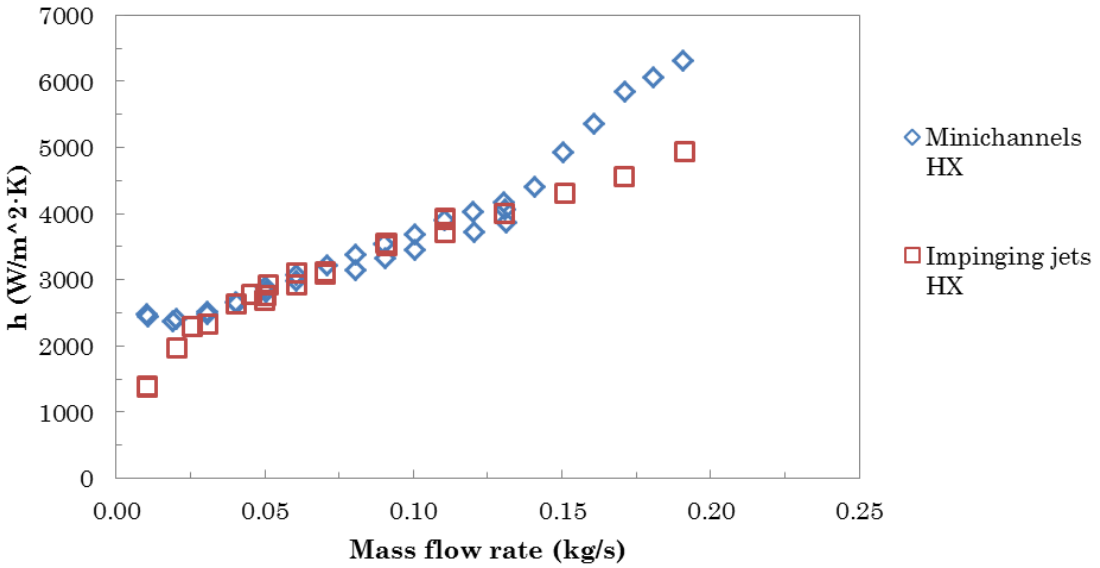

Figure 5.15. Comparing the heat transfer coefficients for the heat exchanger prototypes.

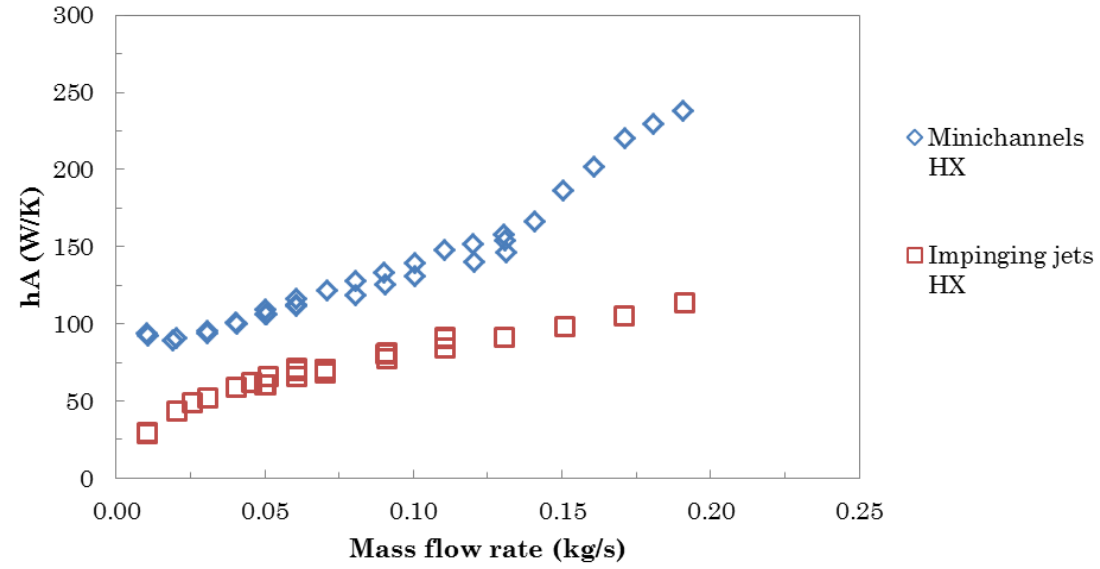

Figure 5.16. Comparing the thermal conductance, *hA*, for the different heat exchanger prototypes.

From Figure 5.15, it can be seen that both heat exchangers have equivalent heat transfer coefficients for the range of $0.02 \leq \dot{m} \leq 0.14$ kg/s. For $\dot{m} < 0.02$ kg/s, the heat transfer coefficient for the impinging jets is 42% lower than that of the minichannels heat exchanger. At $\dot{m} > 0.14$ kg/s, the maximum difference between the heat transfer coefficients for both heat exchangers is only 27%. However, Figure 5.16 shows that the hA for the minichannels heat exchanger is higher than that of the impinging jets heat exchanger for the entire range of the flow rates tested. For $0.02 \leq \dot{m} \leq 0.14$ kg/s, the thermal conductance of the minichannels heat exchanger is, on average, 50% larger compared to the jet heat exchanger. The difference becomes more significant for $\dot{m} > 0.14$ kg/s and reaches a value of 102% at the maximum flow rate tested of 0.19 kg/s. For $\dot{m} < 0.02$ kg/s the hA of the minichannels heat exchanger is about 2 times higher compared to the impinging jets heat exchanger. The better transfer performance of the minichannels heat exchanger, particularly in the region of $0.02 \leq \dot{m} \leq 0.14$ kg/s, is attributed to the larger heat transfer area. For the minichannels heat exchanger (0.0378 m^2) compared to (0.0224 m^2) for the impinging jets heat exchanger, and the negative effect of the confining wall on the heat transfer in the impinging jets heat exchanger design.

A similar observation was made by Robinson [55] who analytically compared the thermal and hydrodynamic performance of several submerged jet arrays and microchannels heat sinks. Thermal analysis results indicated that although microchannels have lower heat transfer coefficients compared to jet arrays, the thermal conductance (hA) of microchannels was either the same or higher when compared to jet array studied. The higher thermal conductance for the microchannels heat sinks was attributed to the larger heat transfer area.

5.3.2. Comparing the Hydrodynamic Performance

The total pressure drop results and the minor losses for the heat exchanger prototypes are plotted in Figure 5.17. The total pressure drop for the impinging jets heat exchanger is higher than that of the minichannels heat exchanger for the entire range of the mass flow rates tested. The maximum pressure drop for the minichannels heat exchanger is 23.3 kPa, which is slightly lower compared to the total pressure drop for the impinging jets heat exchanger which was 27.4 kPa at the same mass flow rate. In addition, for $\dot{m} < 0.1$ kg/s, the total pressure drop for both heat exchanger designs are similar.

Regarding the fitting pressure drop (Figure 5.17), it can be noticed that for a given value of $\dot{m}$, the fitting losses of the impinging jets heat exchanger are, on average, 45% higher than the fitting losses for the minichannels heat exchanger. The higher fitting losses of the impinging jets heat exchanger are attributed to the complex design of the inlet/outlet fittings manifolds. As discussed before, approximately 80% of the pressure drop of the impinging jets heat exchanger is attributed to fittings losses compared to 50% for the minichannels heat exchanger. Therefore, there is a potential for improving the fitting design for both heat exchanger design especially for the impinging jets heat exchanger.

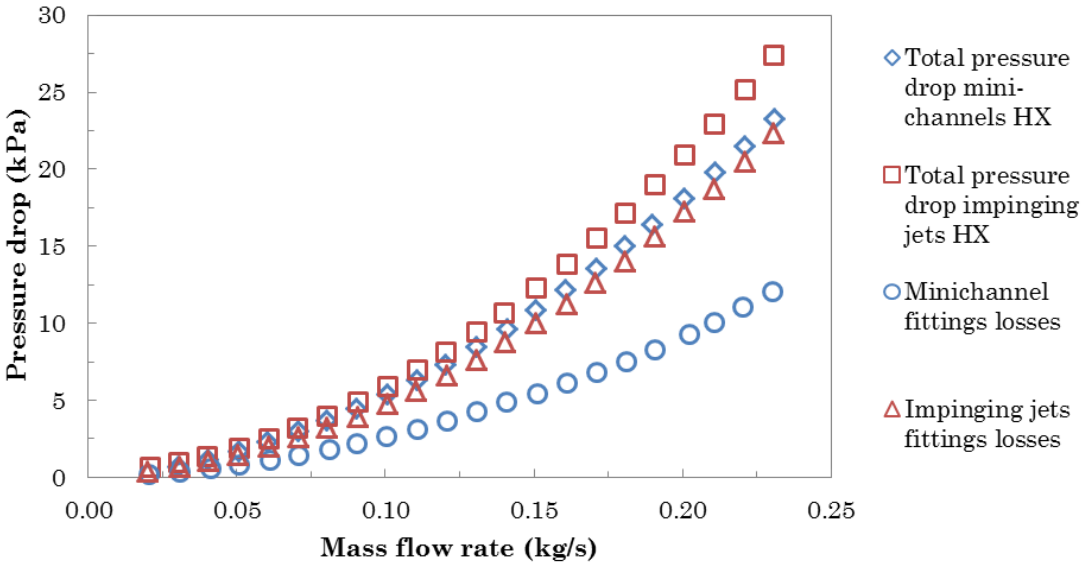

Figure 5.17. Comparing the experimental pressure drop results for the heat exchanger prototypes.

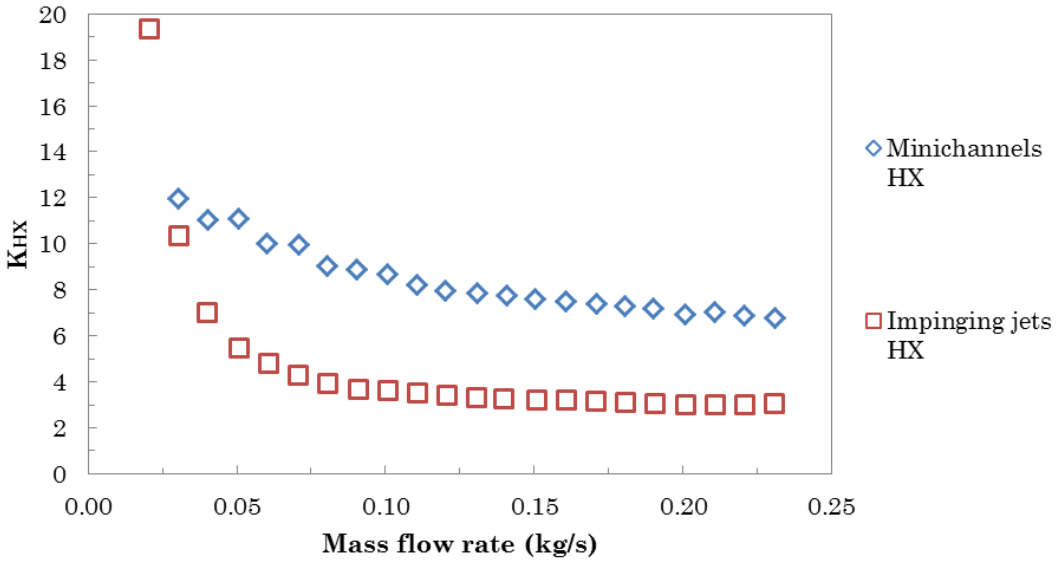

Figure 5.18. Comparing the heat exchanger loss coefficient, K_{HX}, for the heat exchanger prototypes.

The heat exchanger loss coefficient, K_{HX}, is used for comparing the pressure losses inside the heat exchanger. The results of K_{HX} are plotted, versus $\dot{m}$ instead of Re due to the different characteristic lengths. Figure 5.18

illustrates that at any given value of $\dot{m}$, K_{HX} for the impinging jets heat exchanger is 50% lower than the K_{HX} for the minichannels heat exchanger. Therefore, the frictional losses inside the minichannels heat exchanger body are higher compared to the frictional losses of inside the impinging jets heat exchanger. The steady state value of K_{HX} for the minichannels heat exchanger and the impinging jets heat exchanger is approximately 7 and 3, respectively.

The hydraulic pumping power required for the different heat exchanger prototypes were calcuated and the results are plotted in Figure 5.19. As expected, the impinging jets heat exchanger requires a higher pumping power compared to the minichannels heat exchanger, this is due to the larger total pressure drop associated with the impinging jets heat exchanger prototype. The maximum value of pumping power for the impinging jets and the minichannels heat exchanger are 6.7 W and 5.7 W, respectively. For $\dot{m} \leq$ 0.12 kg/s the pumping power required for the exchanger prototypes becomes less than 1 W.

The pumping power, plotted in Figure 5.19, is the hydrodynamic pumping power required which is not conservative since it does not include pump's electrical efficiency and other types of losses associated with pumps. Therefore, the actual electrical power required for operating the pump will be higher than the calculated hydrodynamic pumping power. Taking a typical pump efficiency of 80%, it is anticipated that parasitic pumping losses will be less than 10 W for the maximum flow rate conditions tested.

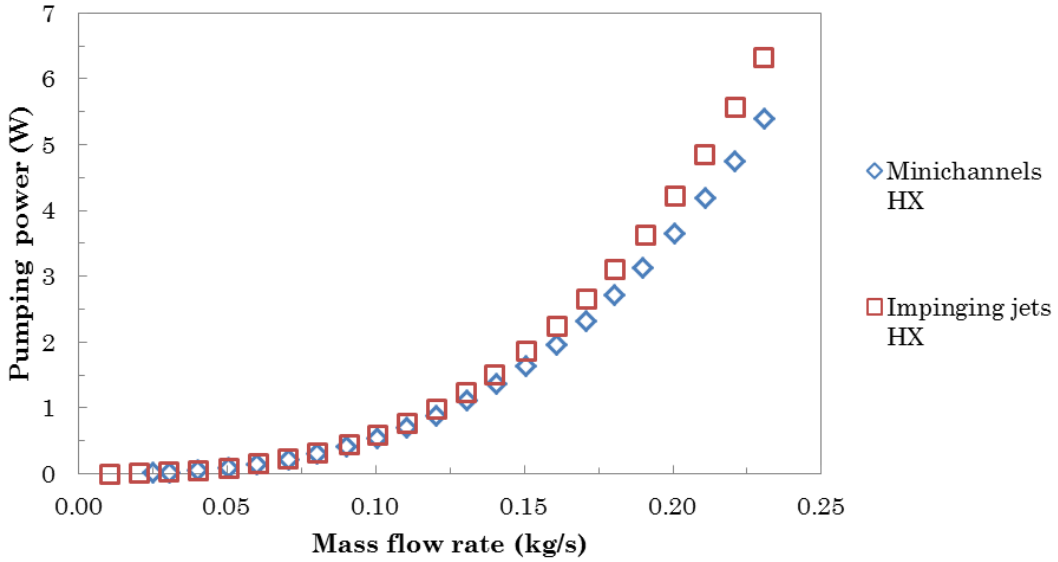

Figure 5.19. Hydraulic pumping power requirements for the heat exchanger prototypes.

5.4. Comparing Temperature Distributions

5.4.1. Longitudinal Temperature Distribution

The temperature distribution for a particular heat exchanger has two components, a longitudinal component and transverse component. For both heat exchanger prototypes, the longitudinal temperature distribution is taken to be the temperature variation along the length of the heat exchanger as shown in Figure 5.20. The temperature distribution along the width of the heat exchanger is denoted as the transverse temperature distribution.

The SS block has thermocouples distributed at various locations as previously seen in Figure 4.4. These thermocouples were used to calculate three heat exchanger surface temperatures T_{s_L}, T_{s_CL}, and T_{s_R}. The locations of the three surface temperatures for both heat exchanger prototype are illustrated in Figure 5.20 and Figure 5.21.

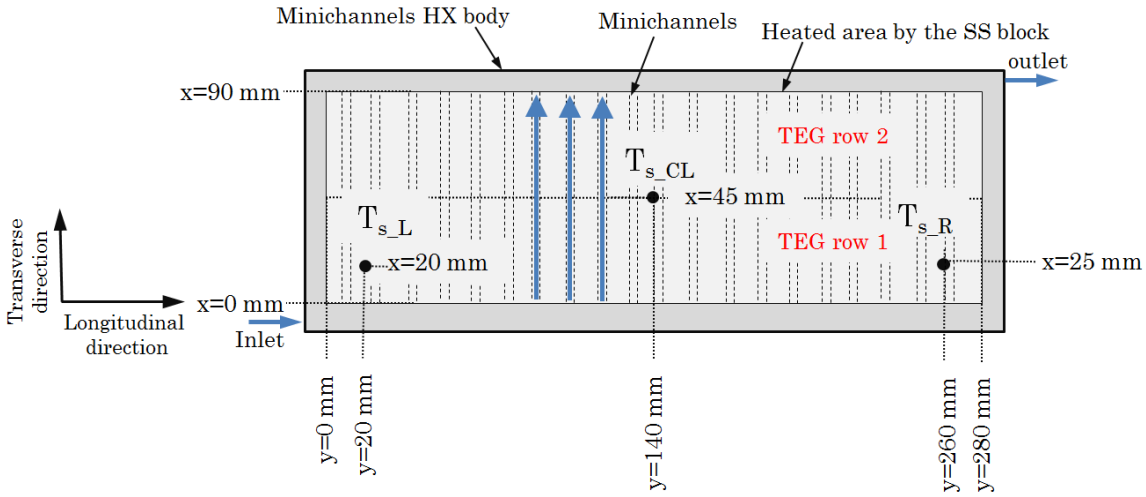

Figure 5.20. Top view schematic of the minichannels heat exchanger showing the definition of the temperature distributions, flow direction (blue arrows), and the location of the measured surface temperatures.

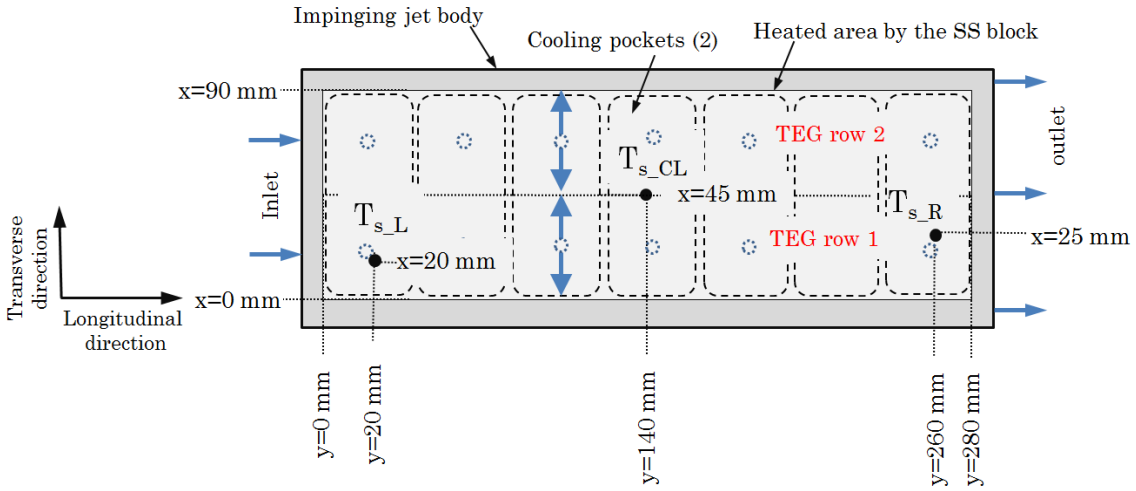

Figure 5.21. Top view schematic of the impinging jets heat exchanger showing the definition of the temperature distributions, flow direction (blue arrows), and the location of the measured surface temperatures.

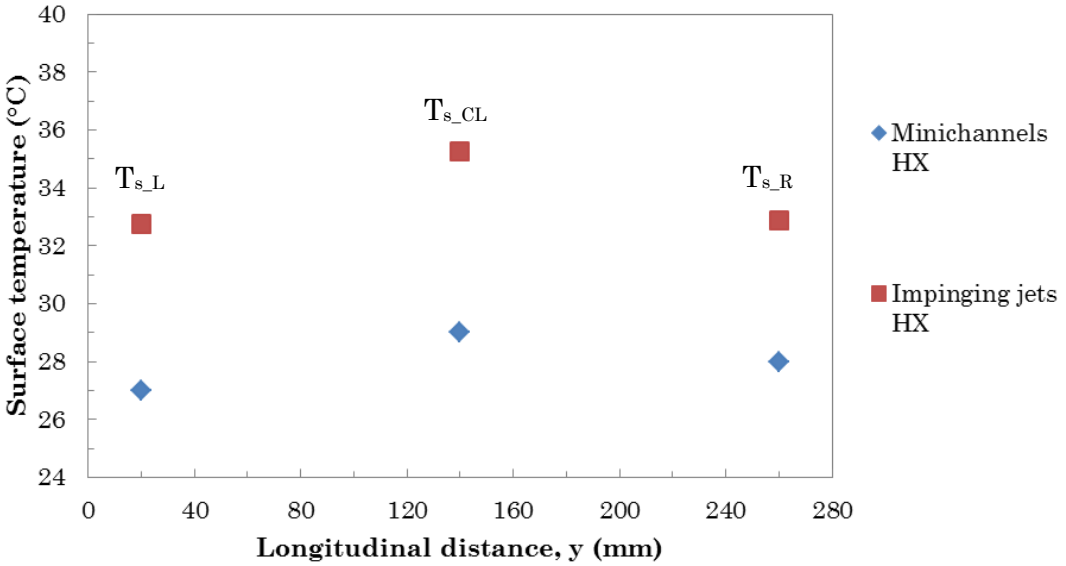

Figure 5.22. The longitudinal temperature distributions for each heat exchanger prototype.

All surface temperatures were calculated by extrapolation of the reading of a particular set of thermocouples. The surface temperature T_{s_L} was found by extrapolating the reading of thermocouples 9 and 10. T_{s_CL} was calculated by extrapolating thermocouples 4, 5, 6 and 7 and the reading of thermocouples 1 and 2 was extrapolated to obtain T_{s_R}. The transverse temperature distribution for each exchanger prototype is plotted in Figure 5.22 for the conditions of $\dot{m} \approx 0.01$ kg/s and $\dot{Q}_{heaters} \approx 340$ W.

For the minichannels heat exchanger, T_{s_CL} was higher than T_{s_R} and T_{s_L}. The maximum temperature difference was between T_{s_L} and T_{s_CL} and it was equal to 2 °C. For the impinging jets heat exchanger, the T_{s_CL} was 2.4 °C higher when compared to T_{s_R} and T_{s_L}. On average the surface temperature of the minichannels heat exchanger is approximately 6 °C lower than the surface temperature of the impinging jets heat exchanger.

As discussed previously in Section 1.2, for every 10 °C increase in the cold side surface temperature (T_{Cold}), the electrical power generated by the

TEG decreases by 12% (1.2% per 1 °C). Assume that 14 TEGs are mounted on the cooling surface of each heat exchanger. Because the average measured surface temperature of the impinging jets heat exchanger is 6 °C higher compared to the minichannels heat exchanger, the electrical power generated by the TEGs mounted on the impinging jets heat exchanger could be about 7% lower compared to TEGs mounted on the minichannels heat exchanger.

5.4.2. Transverse Temperature Distribution

The transverse temperature distribution for any heat exchanger prototypes depends on the heat input and the mass flow rate. To study the transverse temperature distribution, the total heat input to the heat exchanger surface of 340 W and total mass flow rate flowing inside the heat exchanger of 0.01 kg/s were used. These conditions are chosen such that a comparison can be made with the results of longitudinal temperature distribution.

For the minichannels heat exchanger the transverse temperature distribution will occur along the length (along the flow direction) of the minichannel (see Figure 5.20). The minichannels heat exchanger has 140, 90 mm long parallel minichannels. The transverse temperature distribution analysis is performed for a single minichannel. The analysis used and results will be the same for the other minichannels. Given the specified thermal conditions applied to the heat exchanger surface, the heat input applied to a single minichannel (Q_{ch}) was found to be 2.43 W and the mass flow rate per channel, $\dot{m}_{ch}$= 7.14E-5 kg/s corresponding to minichannel Re = 73.6. Figure 5.23, is a schematic diagram depicting a single minichannel and the boundary conditions applied to it.

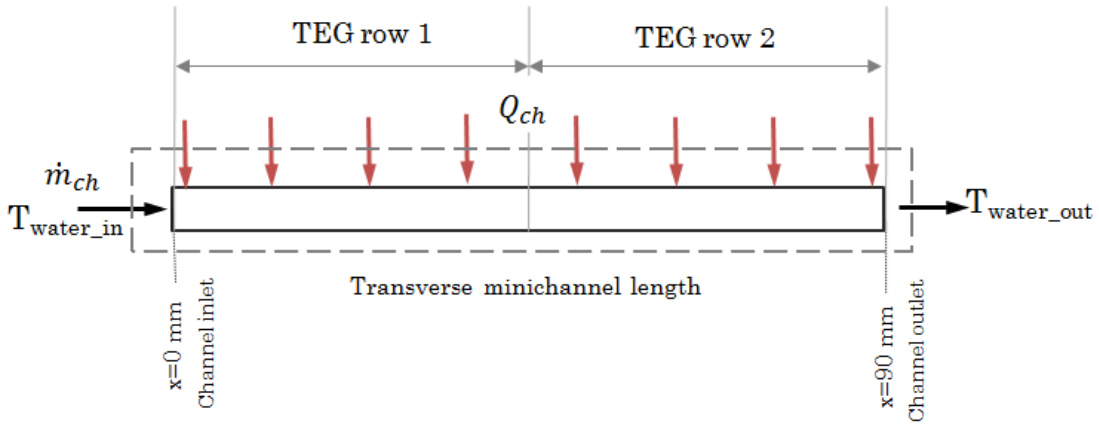

Figure 5.23. A schematic diagram depicting a single minichannel and the boundary conditions applied to it. Also shown is the arrangement of the TEGs with respect to the minichannel length.

Based on the conditions applied on a single minichannel, the increase in the water temperatures between the inlet and the outlet, ΔT_{water}, is 8 °C. The increase change in the water temperature is accompanied with an increase in the minichannel wall temperature. The change in the wall temperature is of particular interest since it will affect the performance and the power generated by the TEG rows mounted on the heat exchanger. To determine the wall temperature profile analytically, the local heat transfer coefficient must be known, i.e. the local Nusselt number (Nu_x) is required. Hausen presented the following correlation (presented in [51]) for determining the local Nusselt numbers for a circular tubes with constant surface temperature boundary condition,

$$Nu_x = 3.66 + \frac{0.0018}{\left(\frac{x/D}{RePr}\right)^{\frac{1}{3}}\left(0.04 + \left(\frac{x/D}{RePr}\right)^{\frac{2}{3}}\right)^2} \tag{5.17}$$

where x is the local distance from the minichannel inlet and all the properties were evaluated at the average water temperature. The local wall temperature (T_{wall_x}) was calculated using the input heat flux per channel

($q" = Q_{ch}/A_{s\_ch}$), the local heat transfer coefficient (h_x) and the local water temperature (T_{water_x}), as illustrated by the equation below.

$$T_{wall\_x} = \frac{q"}{h_x} + T_{water\_x} \tag{5.18}$$

The variation in the minichannel wall temperature and water temperature are plotted in Figure 5.24, x = 0 mm and x = 90 mm correspond to the inlet and the outlet for a single minichannel, respectively. Figure 5.24 shows that the wall temperature variation is not linear near the channel inlet because of the Nu_x varies due to the effect of the simultaneously developing flow. The measured surface temperatures T_{s_L}, T_{s_R}, and T_{s_CL} are in relatively good agreement with their corresponding calculated minichannel wall temperature.

Figure 5.24 shows that the wall temperature is 21 °C at the minichannel inlet and it keeps increasing until it reaches 32 °C at the minichannels outlet. As a result, the average wall temperature of TEG row 1 and TEG row 2 are not equal. The surface temperature of all the TEG modules located in TEG row 1 will change from 21 °C to 28 °C (ΔT across the TEG is 7.3 °C), resulting in an average TEG temperature of 25.5 °C. Similarly, for all the TEG modules located in TEG row 2, the surface temperature changes from 28 °C to 32 °C (ΔT cross the TEG is 4 °C) resulting in an average surface temperature of 30 °C. The difference in the average wall temperature for each row will affect the electrical power generated by the row.

The average temperature of TEG row 1 is lower by 4.5 °C compared to the average temperature of TEG row 2. Given that the electrical power generated by a TEG decreases by 1.2% per °C, then the electrical power generated from TEG row 2 will be approximately lower by 5% compared to the electrical power generated by TEG row 1. Due to the different amounts of

power generated, the electrical wiring between the each TEG row must be carefully chosen in order to maximize the net electrical power generated.

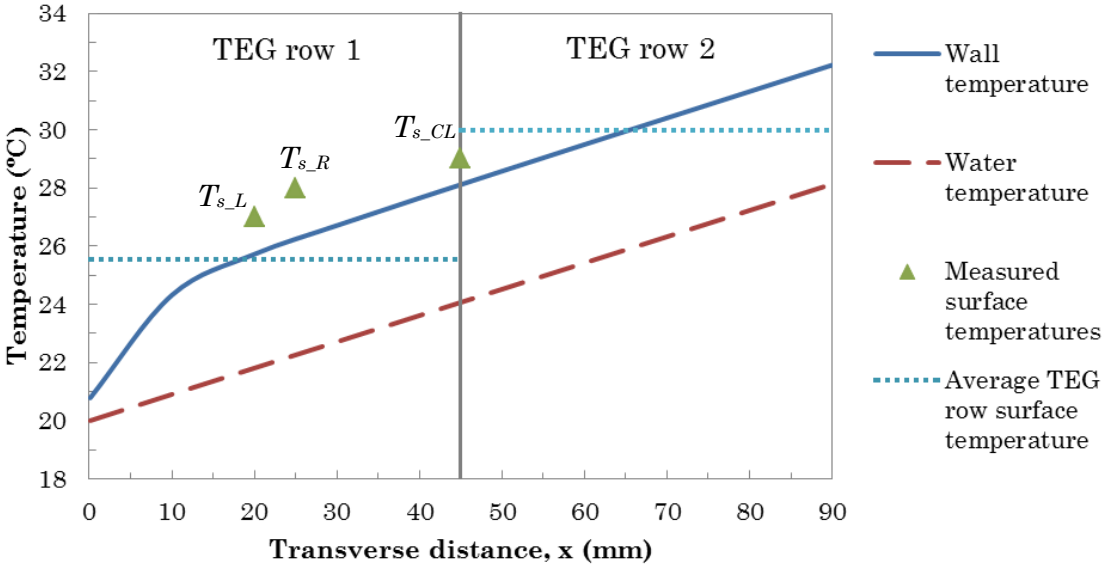

Figure 5.24. The transverse wall temperature distribution for a single minichannel and the corresponding increase in the water temperature.

The electrical power generated by an array of TEGs connected electrically in series is affected by the worst performing TEG in the array. Thus, connecting both TEG rows, mounted on the minichannels heat exchanger, electrically in series will not yield the maximum electrical power because each row is generating different amounts of electrical power. Essentially, the performance of TEG row 2 will lower than performance of TEG row 1. Each TEG row should be connected to a different electrical load in order to maximize the amount of electrical power generated. All the TEG modules located in TEG row 1 should be connected electrically in series to form one circuit. Likewise, all the TEG modules in TEG row 2 should be connected electrically in series and to a separate electrical load.

The transverse temperature distribution for the impinging jets heat exchanger was also studied for the case of total thermal energy input of 340 W and $\dot{m}$ = 0.01 kg/s. The impinging jets heat exchanger prototypes is also designed to cool 14 TEG modules arranged in two rows with seven TEGs per row (Figure 5.21). Each TEG module is cooled by a single, 3 mm diameter jet located at the centre of the TEG, as depicted in Figure 5.25. The transverse temperature distribution refers the wall temperature variation in the heated area corresponding to the location a TEG module. Location x = 22 mm refers to the centre of the jet and x = 0 and 44 mm are the edges of the heated area where the cool coolant exits, as referenced in Figure 5.25. The analysis will be performed for a single jet with its corresponding heated area (i.e. single cooling section), the same analysis can be performed for the other cooling sections in the heat exchanger. Given the specified thermal conditions applied to the heat exchanger surface, the heat input applied on a single cooling section ($Q_{section}$) was found to be 24.3 W and the mass flow rate for a single jet (i.e. per cooling section), $\dot{m}_{section}$= 7.14E-4 kg/s. A schematic of a single section and the thermal conditions applied to it is shown in Figure 5.25.

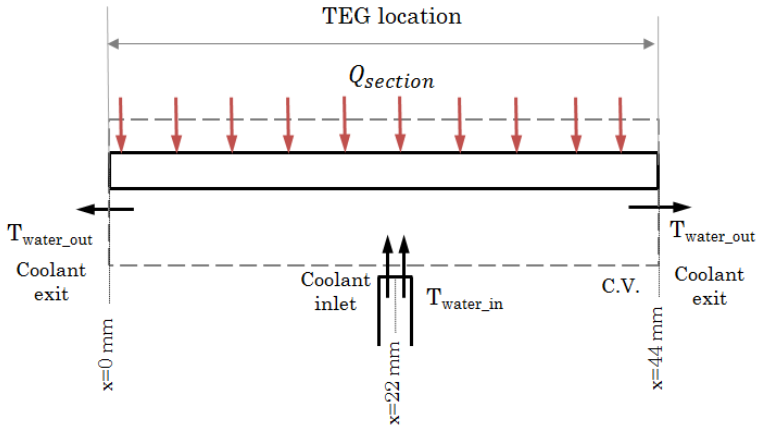

Figure 5.25. A schematic depicting a single TEG cooling section and the boundary conditions applied to it. The TEG location with respect to the impinging jet is also depicted.

As the cooling water exits the jet and strikes the heated surface, its temperature increases, the water will continue to be heated until the water exits from the heated area. For the thermal and flow conditions applied on a single section the increase in the water temperature ΔT_{water} is equal to 8 °C.

To compute the wall temperature distribution inside a single cooling section, the heat transfer coefficient (h_x) is required (see Eqn. 5.18). To compute h_x the local Nusselt number (Nu_x) is required. However, as discussed before in the literature review, correlations capable of predicting Nu_x for a single liquid impinging jet are not available. Thus the heat transfer coefficient profile could not be found analytically.

The liquid jets utilized in the impinging jets heat exchanger, were geometrically similar to the liquid jets tested by Li and Garimella [65] who graphically showed the local heat transfer coefficients for a single jet (D_j= 3.18 mm and H/D_j = 2). It is assumed that the heat exchanger jets have a similar local heat transfer profile as the jets tested by Li and Garimella [65]. Based on this assumption, the local heat transfer coefficient for the jet utilized by the impinging jets heat exchanger and can be obtained and later used to give an idea about the wall temperature distribution for a single cooling section.

The graphically obtained heat transfer coefficient profile (from Li and Garimella) and the experimentally measured average jet heat transfer coefficient were used to establish the local heat transfer coefficient distribution (h_x) of the jets utilized by the impinging jets heat exchanger. Then the local heat transfer coefficient, the cooling section heat flux ($q"$= $Q_{section}/A_{section}$) and the local water temperature (T_{water_x}) were used in Eqn. 5.18 to calculate the local wall temperature. The local wall and water temperature distributions for a cooling section are plotted in Figure 5.26. The surface temperatures T_{s_L} and T_{s_R} are also plotted in Figure 5.26.

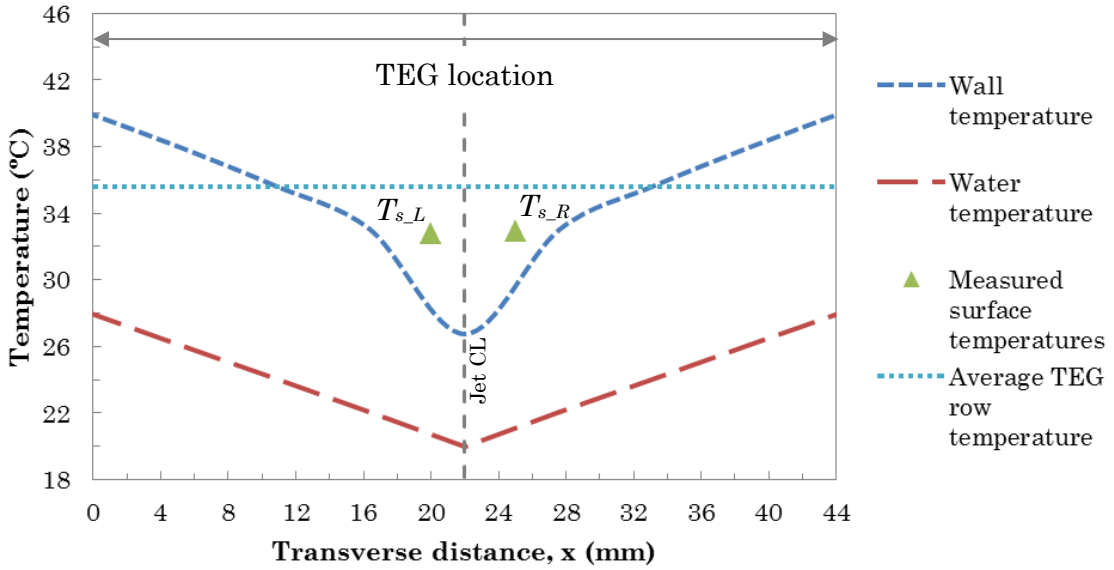

Figure 5.26. The transverse wall temperature distribution for one cooling section of a single TEG and the corresponding water temperature distribution.

Figure 5.26 indicates that the wall temperature is lowest at the jet centerline (i.e. stagnation zone) and it increases further away from it. Furthermore, the wall temperature distribution is nonlinear because the local heat transfer coefficient profile is nonlinear. The heat transfer coefficient is maximum in the stagnation zone (x = 22 mm) and decreases away from it (see Figure 2.6). Therefore the lowest wall temperature is found in the stagnation zone. Moving further away from the stagnation zone, the wall temperature increases due to the decrease in the local heat transfer coefficient. The wall temperature distribution for a single cooling section is symmetric about the jet centreline.

Although the wall temperature profile is not analytically obtained from correlations, it is still useful for making qualitative observations. Figure 5.26 indicated that the lowest wall temperature is 27 °C and it occurs at the centre of the cooling section. In contrast the wall temperature reaches 40 °C at the edge of the cooling section resulting in an averaged wall temperature

of 35 °C. The wall temperature corresponding to the location a single TEG changes by 13 °C between the centre and the outer edges. In other words, if TEGs were mounted on the cooling surface of the impinging jets heat exchanger, the cold side surface temperature of each TEG module will vary by approximately 13 °C between the centre and the outer edges of the TEG.

Each TEG module mounted on the impinging jets heat exchanger is cooled by a dedicated liquid jet which operates independently of the other jets (i.e. in parallel). Therefore, each TEG module will have the same temperature distribution as shown in Figure 5.26. Essentially, when two rows of TEGs are mounted on the on the surface of the impinging jets heat exchanger, the average surface temperature of all the TEGs is row 1 will be the same as the average surface temperature is row 2. Thus, the total electrical power generated from the TEGs in row 1 will be the equal to the total electrical power generated from row 2. This allows all the TEGs to be connected electrically in series allowing for easier installation.

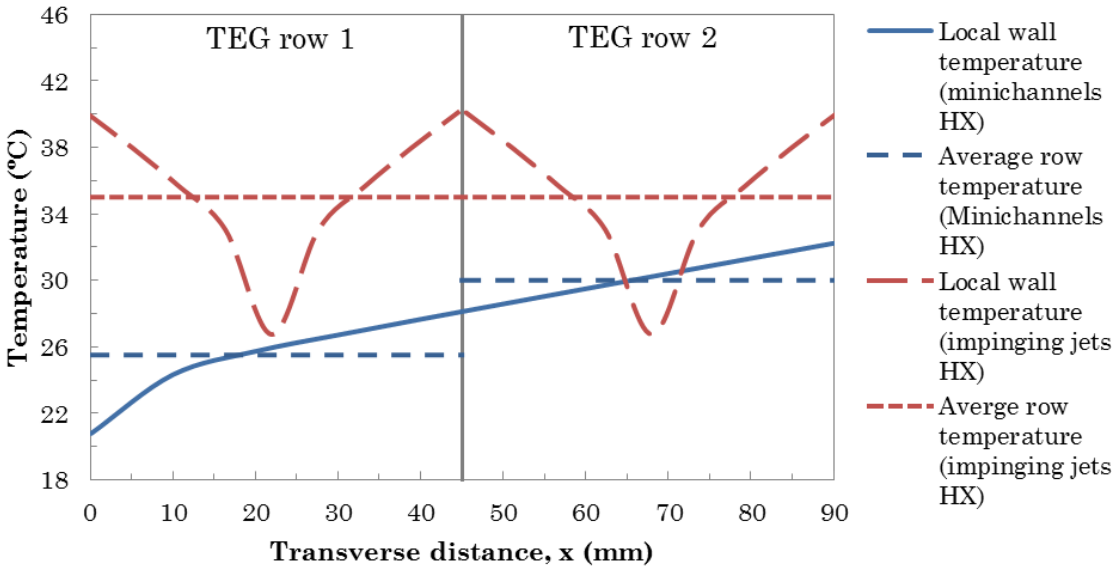

Figure 5.27. The transverse temperature distribution of both heat exchanger prototypes, also shown is the location of the two TEG rows.

The transverse temperature distribution profiles for both heat exchanger prototypes are plotted and compared in Figure 5.27 the locations of the TEG rows and the average row temperature are also shown in the figure. Figure 5.27 clearly shows that the minichannels heat exchanger offers better temperature uniformity per row compared to the impinging jets heat exchanger. The local wall temperature of the TEGs located in row 1 is always lower for the minichannels heat exchanger compared to the impinging jets heat exchanger. Similarly, except near the stagnation zone, row 2 TEGs mounted on the minichannels heat exchanger have a lower local wall temperature compared the row 2 TEGs mounted on the impinging jets heat exchanger. In general, the TEGs mounted on the minichannels heat exchanger experience lower average wall temperature compared to the TEGs mounted on the impinging jets heat exchanger.

The average wall temperature for the TEGs in row 1 is 25.5 °C and 35 °C for the minichannels heat exchanger and the impinging jets heat exchanger, respectively. The average temperature of row 1 mounted on the minichannels heat exchanger is lower by 9.5 °C compared to the average row 1 temperature of the TEGs mounted on the impinging jets heat exchanger. As a result, the electrical power generated by row 1 TEGs mounted on the impinging jets heat exchanger could generate approximately 11% lower electrical power compared to the row 1 TEGs mounted on the minichannels heat exchanger.

Regarding row 2, the average row temperature for the TEGs mounted on the minichannels heat exchanger and the impinging jets heat exchanger are 30 °C and 35 °C respectively. Since the average temperature of row 2 TEGs is higher by 5 °C for the impinging jets heat exchanger case, the electrical power generated by row 2 mounted on the impinging jets heat

exchanger could be lower by 6% compared to the electrical power generated by row 2 mounted on the minichannels heat exchanger.

To conclude, it is found that the minichannels heat exchanger offers better surface temperature distribution per TEG row compared to the impinging jets heat exchanger.

5.5. The Effect of Implementing the Different Heat Exchanger Prototypes on the Performance of the TEG POWER System

As explained in Section 1.2, decreasing the TEG's cold side temperature (T_{Cold}) while keeping the hot side temperature (T_{Hot}) constant will increase the amount of electrical power generated by the TEG. T_{Cold} is affected by the thermal performance of the cold side heat exchanger. A heat exchanger with high thermal conductance (i.e. low thermal resistance) decreases T_{Cold} which leads to an increase in the total electrical power generated by the TEGs (assuming all other parameters remain constant). Since the minichannels heat exchanger has higher thermal conductance compared to the impinging jets heat exchanger, it is important to determine how the total electrical power generated by the TEG POWER system, would be affected if each exchanger prototypes is implemented in the TEG POWER system.

To investigate the former concept further, a numerical model (system model) validated against experimental results was developed in order to predict the performance of the TEG POWER system under a variety of working conditions. The details and the calculation steps for the system model are discussed and presented in Appendix B. For specified thermal conditions at the cold side and hot side heat exchangers, the system model is capable of predicting the total electrical power generated by the 48 TEG modules (P_E) utilized in the TEG POWER system and the thermal energy harvested from the exhaust gas stream (Q_{system}).

The tested cold side heat exchanger prototypes are about half the size of the actual cold side heat exchangers designs required for the TEG POWER system. The full scale cold side heat exchangers will have the same design as the tested prototypes; therefore the thermal performance (i.e. hA) of the full scale heat exchangers can be predicted using appropriate correlations applicable to the tested heat exchanger prototypes. The thermal performance of the full minichannels heat exchanger was well described by the Hausen correlation (Eqn. 2.3). Therefore, it can be used to predict the hA of the full scale minichannels heat exchanger for a given coolant flow rate. Similarly, the hA of the full scale impinging jets heat exchanger can be predicted using the developed correlation for the impinging jets heat exchanger prototype (Eqn. 5.15).

The TEG POWER system requires two identical full scale cold side heat exchanger each capable of cooling 24 TEG modules. Once the coolant mass flow rate of the system ($\dot{m}_{system}$) is specified the thermal conductance of both cold side heat exchangers (hA_{system}) can be calculated based on the thermal conductance (hA) of a single full scale cold side heat exchanger.

The system model requires the thermal conditions of the hot side heat exchanger and the cold side heat exchanger to be specified. The thermal conditions for the hot side heat exchanger were kept constant at an oven exhaust gas temperature of 272 °C (oven set point of (600 °F) 315 °C) and an exhaust gas flow rate of 0.062 kg/s. For the cold side heat exchangers, the coolant temperature was set to 16 °C and the system mass flow ($\dot{m}_{system}$) rate was varied in order to change hA_{system}. The system model simulation results for both heat exchanger prototypes are listed in Table 5.2.

Table 5.2 indicates that higher coolant flow rates yield higher hA values which leads to an increase in the amount of electrical power generated. This trend is obvious for both heat exchanger prototypes.

Regarding the thermal performance, it can be noticed that T_{Cold} is higher for the impinging jets heat exchanger compared to the minichannels heat exchanger. This is attributed to the lower hA for the impinging jets heat exchanger. Most importantly, implementing the minichannels heat exchanger leads to greater electrical power generated by the TEG POWER system compared to the impinging jets heat exchanger. In addition, Table 5.2 illustrates that more thermal energy can be harvested from the exhaust gases when the minichannels heat exchanger is implemented in the TEG POWER system. Since the recovered thermal energy is transferred to the thermal storage system, recovering more thermal energy from the exhaust gases will reduce the charging time required for the thermal storage system which is beneficial for operational stability.

Table 5.2. The total electrical power generated by the TEG POWER system using different cold side heat exchanger prototypes.

Minichannels HX implemented as the cold side heat exchanger				
$\dot{m}_{system}$ (kg/s)	hA_{system} (W/K)	Electrical power, P_{E_MC} (W)	Thermal energy, Q_{system_MC} (kW)	T_{Cold} (°C)
0.25	430	91	4.4	28.8
0.17	392	89	4.3	30.1
0.08	342	82	4.2	35.5
Impinging jets HX implemented as the cold side heat exchanger				
$\dot{m}_{system}$ (kg/s)	hA_{system} (W/K)	Electrical power, P_{E_IJ} (W)	Thermal energy, Q_{system_IJ} (kW)	T_{Cold} (°C)
0.25	253	83	4.3	34.6
0.17	215	79	4.2	38.3
0.08	156	68	4.0	48

Table 5.3. Percent difference in the electrical power generated by the TEG POWER system and the thermal energy recovered as a result of using the different heat exchanger prototypes.

$\dot{m}_{system}$ (kg/s)	$\frac{(P_{E\_MC} - P_{E\_IJ})}{P_{E\_MC}} \times 100\%$	$\frac{(Q_{system\_MC} - Q_{System\_IJ})}{Q_{system\_MC}} \times 100\%$
0.25	8.8	2.3
0.17	11.2	2.6
0.08	17.1	4.7

Table 5.3 tabulates the differences (in percent) in the electrical power and the thermal energy recovered as a result of using the different heat exchanger designs. It is observed that at higher coolant flow rates ($\dot{m}_{system}$=0.25 kg/s), the difference in power generated and the thermal energy recovered is 8.8% and 2.3% respectively. At lower flow rates ($\dot{m}_{system}$=0.08 kg/s), the difference in the electrical power generated and the thermal energy recovered becomes 17.1% and 4.7%, respectively.

To summarize, the minichannels heat exchanger offers better thermal and hydrodynamic performance compared to the impinging jets heat exchanger. In addition, implementing the minichannels heat exchanger in the TEG POWER system increases the total electrical power generated by the TEG POWER system.

Regarding the temperature distribution, the minichannels heat exchanger is better suited for cooling two rows of TEG because the wall temperature variation in the TEG area is not as significant compared to the impinging jets heat exchanger case. Due to favorable overall performance, the minichannels heat exchanger should be utilized as the cold side heat exchanger in the TEG POWER system. All the performance characteristics for both heat exchanger prototypes are summarized and presented in the following section.

6. Conclusions and Recommendations for Future Work

6.1. Conclusions

Research is being conducted in order to develop waste heat recovery systems capable of generating net electrical power using thermoelectric generators. Continuous electrical power generation using TEGs requires the implementation of a cold side and hot side heat exchangers, such that large temperature differences across the TEG module can be established and sustained.

Based on the findings of the literature review, single-phase forced convection through minichannels and liquid impinging jets were identified as promising cooling techniques for designing two cold side heat exchanger prototypes. The main objectives of this research was to design, fabricate and characterize the thermal and hydrodynamic performance of different flat-plate heat exchanger prototypes; that can be implemented as the cold side heat exchangers in waste heat recovery systems. An experimental facility capable of thermally and hydrodynamically testing the different heat exchangers was designed and constructed.

The calculated Nusselt numbers for the minichannels heat exchanger were in good agreement with conventional heat transfer correlations. However, the Nusselt numbers for the impinging jets heat exchanger were 44% lower compared to available heat transfer correlations for single submerged liquid jets. The differences between the experimental results and the jet correlation were attributed to the wall confinement which affected the radial flow emerging from the jet in the case of the impinging jets heat exchanger.

Heat transfer results indicated that for a given value of coolant flow rate the minichannels heat exchanger has higher thermal conductance compared to the impinging jets heat exchanger. At $\dot{m}$ = 0.19 kg/s, that the thermal conductance, hA, of the minichannels heat exchanger was 238 W/°C, while the thermal conductance for the impinging jets heat exchanger was 111 W/°C. The higher thermal conductance of the minichannels heat exchanger is attributed to the greater heat transfer area.

Total pressure drop experiments revealed the impinging jets heat exchanger has total pressure drop of 27.4 kPa, in comparison the total pressure drop for the minichannels heat exchanger of 23.3 kPa. The minor losses associated with the inlet and the outlet heat exchanger fittings were experimentally measured. Tests results revealed that the pressure drop associated with the inlet/outlet fittings losses can be a significant portion of the total heat exchanger's pressure drop. On average, for the minichannels heat exchanger, 50% of the total pressure drop was attributed to inlet/outlet fitting losses. For the impinging jets heat exchanger prototype, the inlet/outlet fittings losses accounted for 80% of the total pressure drop. Regarding the pressure losses inside the heat exchanger prototypes in the turbulent flow regime, the minichannels heat exchanger and the impinging jets heat exchanger have loss coefficients, K_{HX}, of 7 and 3, respectively. The obtained values of K_{HX} loss coefficients are comparable to the loss coefficients of a fully open globe valve and fully open angle valves which have loss coefficients of 10 and 5, respectively [86].

The hydraulic pumping power requirements were found to be 5.7 W for the minichannels heat exchanger and 6.8 W for the impinging jets heat exchanger. The actual required pumping power for both heat exchanger prototypes is less than 10 W (assuming pump efficiency of 80%). The electrical pumping power requirements for operating the both heat exchanger

prototypes are approximately one order of magnitude lower compared to the net electrical power generated by the TEG POWER system.

Considering the longitudinal temperature distribution, it was found that the average surface temperature of minichannels heat exchanger is lower by 6 °C compared to the surface temperature of the impinging jets heat exchanger. Regarding the transverse temperature distribution, the minichannels heat exchanger offered more uniform surface temperature distribution per TEG row compared to the impinging jets heat exchanger. As a result, if two TEG rows are to be placed on top of the cooling surface of each heat exchanger prototypes, the electrical power generated by TEG row 1 and TEG row 2, mounted on the impinging jets heat exchanger, was found to be 11% to 6% lower than the corresponding TEG rows mounted on the minichannels heat exchanger.

Simulation data indicated that depending on the coolant flow rate, the minichannels heat exchanger is expected to result in the generation of 8.8% to 17.1% higher electrical power compared to impinging jets heat exchanger when implemented in the TEG POWER system. In addition, using the minichannels heat exchanger instead of the impinging jets heat exchanger in the TEG POWER system could increase the thermal energy recovered from the exhaust gases by 2.3% to 4.7% depending on the coolant flow rate.

This thesis is part of a larger research initiative known as the TEG POWER system which focuses on harvesting the wasted thermal energy from the exhaust gases of commercial pizza ovens. The TEG POWER system is a result of research collaboration between TMRL, Pizza Pizza, Acrolab and Thermal Electronics Corp. The contribution of this work to the TEG POWER system is to experimentally determine which cold side heat exchanger prototype is best suited for the POWER Project. Based on the testing results, the minichannels heat exchanger offers the best combination of heat transfer

and pressure drop, when compared to the impinging jets heat exchanger, making it the preferred heat exchanger prototype for implantation in the TEG POWER system.

6.2. Recommendations for Future Work

This research work was focused on determining the thermal and hydrodynamic performance of each heat exchanger prototype. Considering the experimental results, the minichannels heat exchanger is recommended for implementation in the TEG POWER Project.

However, an important factor that was not discussed in this work is the manufacturing process required for fabricating each heat exchanger prototype. The manufacturing process required is an important factor that should be considered carefully when designing any heat exchanger. Therefore, investigating the cost effectiveness of the manufacturing process required for fabricating each heat exchanger prototype is recommended for future work.

6.2.1. Heat Exchanger Manufacturing Process

Machining the minichannels on the heat transfer plate was the most difficult and time consuming process during the fabrication of the minichannels heat exchanger. As mentioned previously, a high precision CNC milling centre was used to carefully machine the minichannels onto the heat transfer plate. To prevent milling cutter's premature failure, slow feed rate and smaller depth of cut were used for milling the minichannels. Using such machining parameters slowed down the milling process and resulted in a longer machining time. Therefore, manufacturing the minichannels using a milling technique may not economical for mass production. Other possible manufacturing techniques must be investigated for making the minichannels features.

Stamping and extrusion are alternative manufacturing processes that can be used to create the straight minichannel features on the heat transfer plate. The idea of stamping the minichannel on the heat transfer plate, and the feasibility of extruding the heat transfer plate with the minichannel features should both be investigated further in detail to determine if they are applicable for mass production.

If the cost of making the straight (or curved) minichannels heat exchanger is too high, then the second option is to utilize the impinging jets heat exchanger as the cold side heat exchanger. Unlike the minichannels heat exchanger, the impinging jets heat exchanger did not contain any miniature features making it easier to fabricate. All the design features of the impinging jets heat exchanger were machined using larger diameter milling cutters (compared to the minichannels milling cutter), which allowed for faster feed rate and larger depth of cut which resulted in shorter machining time (compared to the minichannels heat exchanger). Shorter machining time makes the heat exchanger design less expensive to manufacture making it economical for mass production. Furthermore, since the impinging jets heat exchanger body does not contain any miniatures features essential for achieving the required heat transfer; it can be easily manufactured using plastic injection molding techniques. Injection molding widely used manufacturing technology because it is well suited for mass production. Further research and analysis can be devoted to determine if it is economical for manufacturing the impinging jets heat exchanger.

6.2.2. Enhanced Cold Side Heat Exchanger Designs

For other waste heat recovery systems that have higher heat flux dissipation requirements, cold side heat exchanger designs utilizing curved minichannels and impinging jets arrays could be designed and implemented.

Curved channels are known to have higher heat transfer capability compared to straight channels due to the enhanced mixing attributed to the inception of Dean vortices. The drawback of curved minichannels is that they are more difficult to machine using conventional milling fabrication techniques compared to straight to minichannels. Curved minichannels could possibly be created, without much difficulty, using a stamping operating instead of conventional milling techniques. The idea of using stamping to manufacture curved minichannels should be investigated further to determine if it is suitable and economical for producing the curved minichannels.

An alternative cold side heat exchanger design capable of handling high heat flux loads could utilize an array of jets, instead of single jets, for cooling a single TEG. The heat transfer performance of jet arrays is either equivalent or higher compared to single impinging jets. Furthermore, using a single jet for cooling a heated area can result in a large wall temperature variation due to the significant variation in the local heat transfer coefficient. Submerged impinging jets arrays have more uniform heat transfer coefficient due to the utilization of multiple jets for heat dissipation. Therefore, the wall temperature distribution in the heated area is more uniform for the case of submerged jet arrays. The merit of employing liquid jet arrays for designing the cold side heat exchanger should be investigated along with manufacturing techniques suitable for making the jet arrays.

References

[1] "Canada's Electricity Industry," Canadian Electricity Association, [Online]. Available: http://www.electricity.ca/media/Electricity101/Electricity101.pdf. [Accessed 5 July 2014].

[2] "World electricity generation by source of energy: Terawatt hours (TWh)," OECD Factbook 2013, [Online]. Available: http://www.oecd-ilibrary.org/economics/oecd-factbook-2013/electricity-generation_factbook-2013-43-en;jsessionid=1c0s513rvp8kj.x-oecd-live-02. [Accessed 27 June 2014].

[3] N. Zhou, X. Wang, Z. Chen and Z. Wang, "Experimental study on organic rankine cycle for waste heat recovery from low-temperature flue gas," *Energy,* vol. 55, pp. 216-225, 2013.

[4] J. Holman, "Perspective: waste heat to power — still waiting for a breakthrough," July 2011. [Online]. Available: http://www.heatispower.org/wp-content/uploads/2011/11/IDC-Waste-Heat-to-Power.pdf. [Accessed 5 June 2014].

[5] S. Bédard, "Waste heat to power: a process integration perspective," 2009. [Online]. Available: http://www.nrcan.gc.ca/sites/www.nrcan.gc.ca/files/canmetenergy/files/pubs/2009-200_e.pdf. [Accessed 10 June 2014].

[6] BCS, Incorporated, "Waste heat recovery: technology and opportunities in the U.S. industry," March, 2008.

[7] K. Ebrahimi, G. Jones and A. Fleischer, " A review of data center cooling technology, operating conditions and the corresponding low-grade waste heat recovery opportunities," *Renewable and Sustainable Energy Reviews,* vol. 31, pp. 622-638, 2014.

[8] D. Finnerty, "The development of methodologies and a novel test facility for the charaterisation of thermoelectric generators," Master's Thesis Dept. of Mechanical Engineering McMaster University, Hamilton, ON., 2013.

[9] A. Rezania and L. Rosendahl, "Thermal effect of a thermoelectric generator on parallel microchannel heat sink," *Energy,* vol. 37, pp. 220-227, 2012.

[10] A. Rezania, K. Yazawa, L. Rosendahl and A. Shakouri, "Co-optimized design of microchannel heat exchangers and thermoelectric generators," *International Journal of Thermal Sciences,* vol. 72, pp. 73-81, 2013.

[11] B. Agostini, M. Fabbri, J. Park, L. Wojtan, J. Thome and B. Michel, "State of the art of high heat flux cooling technologies," *Heat Transfer Engineering,* vol. 28, pp. 258-281, 2007.

[12] I. Mudawar, "Assessment of high-heat-flux thermal management schemes," *IEEE Transactions on Component and Packing Technologies,* vol. 24, pp. 122-141, 2001.

[13] S. Jajja, W. Ali, H. Ali and A. Ali, "Water cooled minichannel heat sinks for microprocessor cooling: effect of fin spacing," *Applied Thermal Engineering,* vol. 64, pp. 76-82, 2014.

[14] S. Bintoro, A. Akbarzadeh and M. Mochizuki, "A closed-loop electronics cooling by implementing single phase impinging jet and mini channels heat exchanger," *Applied Thermal Engineering,* vol. 25, pp. 2440-2753, 2005.

[15] S. Kandlikar and W. Grande, "Evaluation of microchannel flow passages-Thermohydraulic performance and fabrication technology," *Heat Transfer Engineering,* vol. 24, pp. 3-17, 2003.

[16] X. Xie, Z. Liu, Y. He and W. Tao, "Numerical study of laminar heat transfer and pressure drop characteristics in a water-cooled minichannel heat sink," *Applied Thermal Engineering,* vol. 29, pp. 64-74, 2009.

[17] W. Dean and J. Hurst, "Note on the motion of fluid in a curved pipe," *Mathematika,* vol. 6, pp. 77-85, 1959.

[18] Y. Sui, C. Teo, P. Lee, Y. Chew and C. Shu, "Fluid flow and heat transfer in wavy microchannels," *International Journal of Heat and Mass Transfer,* vol. 53, pp. 2760-2772, 2010.

[19] Y. Sui, P. Lee and C. Teo, "An experimental study of flow friction and heat transfer in wavy microchannels with rectangular cross section," *International Journal of Thermal Sciences,* vol. 50, pp. 2473-2482, 2011.

[20] Y. Cengel and A. Ghajar, Heat and Mass Transfer Fundamentals and Applications, New York: McGraw-Hill, 2010.

[21] F. Kreith and M. Bohn, Principles of Heat Transfer, New York: Harper & Row, 1986.

[22] S. Eiamsa-ard and P. Promvonge, "Experimental investigation of heat transfer and friction characteristics in a circular tube fitted with V-nozzle turbulators," *International Communications in Heat and Mass Transfer,* vol. 33, pp. 591-600, 2006.

[23] F. Incropera, Liquid cooling of Electronic Devices by Signle Phase Convection, New York: Wiley, 2009.

[24] P. Tie, Q. Li and Y. Xuan, "Investigation on the submerged liquid jet arrays impingement cooling," *Applied Thermal Sciences,* vol. 31, pp. 2757-2763, 2011.

[25] D. Womac, S. Ramadhyani and F. Incropera, "Correlating equations for impingement cooling of small heat sources with single circular liquid jets," *Journal of Heat Transfer,* vol. 115, pp. 106-115, 1993.

[26] D. Tuckerman and R. Pease, "High performance heat sink for VLSI," *IEEE Electron Device Letters,* Vols. EDL-2, pp. 126-129, 1981.

[27] A. Adham, N. Mohd-Ghazali and R. Ahmad, "Thermal and hydrodynamic analysis of microchannel heat sinks: a review," *Renewable and Sustainable Energy Reviews,* vol. 21, pp. 614-622, 2013.

[28] G. Morini, "Single-phase convective heat transfer in microchannels: a review of experimental results," *International Journal of Thermal Sciences,* vol. 43, pp. 631-651, 2004.

[29] S. Mehendale, A. Jacobi and R. Shah, "Fluid flow and heat transfer at micro-and meso-scales with applications to heat exchanger design," *Applied Mechanics Reviews,* vol. 53, pp. 175-193, 2000.

[30] M. Steinke and S. Kandlikar, "Single-phase liquid friction factors in microchannels," *International Journal of Thermal Sciences ,* vol. 45, pp. 1073-1083, 2006.

[31] C. Sobhan and S. Garimella, "A comparative analysis of studies on heat transfer and fluid flow in microchannels," *Microscale Thermophysical Engineering,* vol. 5, pp. 293-311, 2001.

[32] A. Duncan and G. Peterson, "Review of Microscale Heat Transfer," *Applied Mechanics Reviews,* vol. 47, pp. 397-429, 1994.

[33] P. Lee, S. Garimella and D. Liu, "Investigation of heat transfer in rectangular microchannels," *International Journal of Heat and Mass Transfer,* vol. 48, pp. 1688-1704, 2005.

[34] B. Wang and X. Peng, "Experimental investigation on liquid forced convection heat transfer through microchannels," *International Journal of Heat and Mass Transfer,* Vols. 37, Supplement (1), pp. 73-82, 1994.

[35] X. Peng and G. Peterson, "Convective heat transfer and flow friction for water flow in microchannel structures," *International Journal of Heat and Mass Transfer,* vol. 39, pp. 2599-2608, 1996.

[36] T. Harms, M. Kazmierczak and F. Gerner, "Developing convective heat transfer in deep rectangular microchannels," *International Journal of Heat and Fluid Flow,* vol. 20, pp. 149-157, 1999.

[37] O. Mokrani, B. Bourouga, C. Castelain and H. Peerhossaini, "Fluid flow and convective heat transfer in flat microchannels," *International Journal of Heat and Mass Transfer,* vol. 52, pp. 1337-1352, 2009.

[38] M. Rahman, "Measurements of heat transfer in microchannel heat sinks," *International Communications in Heat and Mass Transfer,* vol. 27, pp. 495-506, 2000.

[39] W. Qu and I. Mudawar, "Experimental and numerical study of pressure drop and heat transfer in a single-phase micro-channel heat sink," *International Journal of Heat and Mass Transfer,* vol. 45, pp. 2549-2565, 2002.

[40] B. Xu, K. Ooi, N. Wong and W. Choi, " Experimental investigation of flow friction for liquid flow in microchannels," *International Communications in Heat and Mass Transfer,* vol. 27, pp. 1165-1176, 2000.

[41] Mirmanto, D. Kenning, J. Lewis and T. Karayiannis, "Pressure drop and heat transfer characteristics for single-phase developing flow of water," *Journal of Physics: Conference Series,* vol. 395, pp. 1-13, 2012.

[42] H. Park and J. Punch, "Friction factors and heat transfer in multiple microchannels with uniform flow distribution," *International Journal of Heat and Mass Transfer,* vol. 51, pp. 4535-4543, 2008.

[43] N. Caney, P. Marty and J. Bigot, "Friction losses and heat transfer of single-phase flow in a mini-channel," *Applied Thermal Engineering,* vol. 27, pp. 1715-1721, 2007.

[44] P. Lee, S. Garimella and D. Liu, "Investigation of heat transfer in rectangular microchannels," *International Journal of Heat and Mass Transfer,* vol. 48, pp. 1688-1704, 2005.

[45] D. Pfund, D. Rector, A. Shekarriz, A. Popescu and J. Welty, "Pressure drop measurements in a microchannel," *AIChE Journal,* vol. 46, pp. 1496-1507, 2000.

[46] S. Shen, J. Xu, J. Zhou and Y. Chen, "Fluid flow and heat transfer with rough wall surface," *Energy Conversion and Management,* vol. 47, pp. 1311-1325, 2006.

[47] X. Peng and G. Peterson, "Convective heat transfer and flow friction for water in microchannel structures," *International Journal of Heat and Mass Transfer,* vol. 39, pp. 2599-2608, 1996.

[48] H. Park and J. Punch, "Friction factors and heat transfer in multiple microchannels with uniform flow distribution," *International Journal of Heat and Mass Transfer,* vol. 51, pp. 4535-4543, 2008.

[49] N. Caney, P. Marty and J. Bigot, "Friction losses and heat transfer of single-phase flow in a mini-channel," *Applied Thermal Engineering,* vol. 27, pp. 1715-1721, 2007.

[50] D. Pfund, D. Rector, A. Shekarriz, A. Popescu and J. Welty, "Pressure drop measurement in microchannels," *AIChE Journal ,* vol. 46, pp. 1469-1507, 2000.

[51] S. Kakak, R. Shah and W. Aung, Handbook of Single-Phase Convective Heat Transfer, New York: John Wiley & Sons, 1987.

[52] P. Jiang, M. Fan, G. Si and Z. Ren, "Thermal-hydraulic performance of small scale micro-channel and porous-media heat exchangers," *International Journal of Heat and Mass Transfer,* vol. 44, pp. 1039-1501, 2001.

[53] M. Moharana, G. Agarwal and S. Khandekar, "Axial conduction in single-phase simultaneously developing flow in a rectangular mini-channel array," *International Journal of Thermal Sciences,* vol. 50, pp. 1001-1012, 2001.

[54] F. Incropera and D. DeWitt, Fundamentals of Heat and Mass Transfer, New York: John Wiley and Sons, 1996.

[55] A. Robinson, "A Thermal–hydraulic comparison of liquid microchannel and impinging liquid jet array heat sinks for high-power electronics cooling," *IEEE Transactions on Components and Packaging Technologies,* vol. 32, pp. 347-357, 2009.

[56] B. Petukhov, "Heat transfer and friction factors in turbulent pipe flow with physical properties," *Advances in Heat Transfer,* vol. 6, pp. 503-564, 1970.

[57] V. Gnielinski, "New equations for heat and mass transfer in turbulent pipe channel flow," *International Chemical Engineering,* vol. 16, pp. 359-368, 1976.

[58] R. Shah, "A Correlation for laminar hydrodynamic entry length solutions for circular and noncircular ducts," *Journal of Fluids Engineering,* vol. 100, pp. 177-179, 1978.

[59] R. Shah and A. London, Laminar flow forced convection in ducts: Supplement 1 to Advances in Heat Transfer, New York: Academic Press, 1978.

[60] R. Fox, P. Pritchard and A. McDonald, Introduction to Fluid Mechanics, New York: John Wily & Sons, Inc., 2009.

[61] K. Jambunathan, E. Lai, M. Moss and B. Button, "A review of heat transfer data for single circular jet impingement," *International Journal of Heat and Fluid Flow,* vol. 13, pp. 106-115, 1992.

[62] B. Webb and C. Ma, "Single-phase liquid impingement heat transfer," *Advances in Heat Transfer,* vol. 26, pp. 105-217, 1995.

[63] S. Garimella and R. Rice, "Confined and submerged liquid jet impingement heat transfer," *Journal of Heat Transfer,* vol. 117, pp. 871-877, 1995.

[64] C. Ma, Y. Gan, Y. Tian and D. Lei, "Liquid jet impingement heat transfer with or without boiling," *Journal of Thermal Science,* vol. 2, pp. 32-49, 1993.

[65] C. Li and S. Garimella, "Prandtl-number effects and generalized correlations for confined and submerged jet impingement," *International Journal of Heat and Mass Transfer,* vol. 44, pp. 3471-3480, 2001.

[66] B. Elison and B. Webb, "Local heat transfer to impinging liquid jets in the initially laminar, transitional, and turbulent regimes," *International Journal of Heat and Mass Transfer,* vol. 37, pp. 1207-1216, 1994.

[67] S. Garimella and B. Nenaydykh, "Nozzle-geometry effects in liquid jet impingement heat transfer," *International Journal of Heat and Mass Transfer,* vol. 39, pp. 2915-2923, 1996.

[68] L. Brignoni and S. Garimella, "Effects of nozzle-inlet chamfering on pressure drop and heat transfer in confined air jet impingement," *International Journal of Heat and Mass Transfer,* vol. 43, pp. 1133-1139, 2000.

[69] M. Molana and S. Banooni, "Investigation of heat transfer processes involving liquid impingement jets: a review," *Brazilian Journal of Chemical Engineering,* vol. 30, pp. 413-435, 2013.

[70] S. Sitharamayya and K. Raju, "Heat transfer between an axisymmetric jet and a plate held normal to the flow," *The Canadian Journal of Chemical Engineering,* vol. 47, pp. 365-368, 1969.

[71] A. Robinson and E. Schnitzler, "An experimental investigation of free and submerged miniature liquid jet array impingement heat transfer," *Experimental and Thermal Fluid Sciences,* vol. 32, pp. 1-13, 2007.

[72] D. Womac, F. Incopera and S. Ramadhyani, "Correlating equations for impingement cooling of small heat sources with multiple circular liquid jets," *Journal of Heat Transfer,* vol. 116, pp. 482-486, 1994.

[73] B. Whelan, R. Kempers and A. Robinson, "A liquid-based system for CPU cooling implementing a jet array impingement waterblock and a tube array remote heat exchanger," *Applied Thermal Engineering,* vol. 39, pp. 86-94, 2012.

[74] X. Luo and S. Liu, "A microjet array cooling system for thermal management of high-brightness LEDs," *IEEE Transactions on Advanced Packaging,* vol. 30, pp. 475-484, 2007.

[75] C. Hsu, G. Huang, H. Chu, B. Yu and D. Yao, "Experiments and simulations on low-temperature waste heat harvesting system by thermoelectric power generators," *Applied Energy,* vol. 88, pp. 1291-1297, 2001.

[76] A. Rezania, L. Rosendahl and S. Andreasen, "Experimental investigation of thermoelectric power generation versus coolant pumping power in a microchannel heat sink," *International Communications in Heat and Mass Transfer,* vol. 39, pp. 1054-1058, 2012.

[77] X. Niu and J. Yu, "Experimental study on low-temperature waste heat thermoelectric generator," *Journal of Power Sources,* vol. 188, pp. 621-626, 2009.

[78] D. Dai, Y. Zhou and J. Liu, "Liquid metal based thermoelectric generation system for waste heat recovery," *Renewable Energy,* vol. 36, pp. 3530-3536, 2011.

[79] Unifrax, "FiberFrax product information sheet," [Online]. Available: http://www.unifrax.com.au/prodsheets/Fiberfrax%20Paper.pdf. [Accessed 15 May 2014].

[80] K. Electronic, "Heat-Conductive Paste Arctic Silver 5," [Online]. Available: http://www.kuhne-electronic.de/fr/produkte/andere-komponenten/waermeleitpaste-arctic-silver-5.html. [Accessed 15 August 2014].

[81] C. Y. Ho and T. Chu, "Electrical resistivity and thermal conductivity of nine selected AISI stainless steels," prepared for AISI, Rep. 15, Washington, D.C, September 1977.

[82] S. Kline and F. McClintock, "Describing uncertainties in single-sample experiments," *Mechanical Engineering,* vol. 75, pp. 3-8, 1953.

[83] V. Natarajan and K. Christensen, "The impact of surface roughness on flow through a rectangular microchannel from laminar to turbulent regimes," *Microfluidics Nanofluidics,* vol. 9, pp. 95-121, 2010.

[84] M. Rao and S. Khandekar, "Simultaneously developing flows under conjugated conditions in a minichannel array: liquid crystal thermography and computational simulations," *Heat Transfer Engineering,* vol. 30, pp. 751-761, 2009.

[85] M. Shoukri and A. Calka, "On the heat transfer characteristics of constrained air jets impinging on a flat surface," *International Journal of Heat and Mass Transfer,* vol. 30, pp. 203-205, 1986.

[86] Y. Cingel and J. Cimbala, Fluid Mechanics Fundamentals and Applications, New York: McGraw Hill, 2010.

Appendix A: Uncertainty Analysis

Various parameters were measured and calculated in this thesis. The uncertainties associated with the measured and calculated parameters are discussed in below.

A1. The Uncertainty in the Measured Parameters

Pressure

Pressure drop measurements was measured using a Validyne DP15 pressure transducer with 5 PSI (34 kPa) pressure diaphragm. The signal from the pressure transducer was passed to a signal conditioner (Validyne CD23) then read by the DAQ system. The same instrumentations and setup were used for measuring the pressure drop while conducting the experiments.

The pressure transducer was calibrated, using high accuracy pressure calibrator (Crystal is33), in order to decrease the transducer's uncertainty and improve the reading accuracy. Initially, the pressure transducer was calibrated starting from 0 PSI to 5 PSI in 0.25 PSI increments. To account for possible hysteresis errors, the calibration procedure was repeated but this time starting from 5 PSI to 0 PSI with 0.25 decrements. The data from both calibration procedures were used to obtain a linear calibration equation for the pressure transducer.

The uncertainty associated with the pressure measurement was due to the errors in the measurement devices and the calibration technique.

Pressure diaphragm uncertainty

According to the manufacturer's data, the accuracy of the 5 PSI pressure diaphragm is 0.25% of full scale reading. The stated uncertainty includes the effect of linearity, hysteresis, and repeatability. Thus, the pressure diaphragm uncertainty is equal to,

$$\delta P_{Accuracy} = \left(\frac{0.25}{100} * 34.474\ kPa\right) = 0.086\ kPa.$$

Pressure calibrator uncertainty

According to the manufacturer's specifications, the uncertainty in the pressure calibrator is 0.005% of full scale. The pressure calibrator had two pressure ranges: high and low. The low pressure range (max. 36 PSI or 248.2 kPa) was used for calibrating the pressure transducer. The uncertainty in the pressure calibrator reading is,

$$\delta P_{Calibration} = \left(\frac{0.005}{100} * 248.2\ kPa\right) = 0.012\ \text{kPa}$$

Calibration equation error

The calibration data were used to obtain linear calibration equation for the pressure transducer. The maximum error between the calibration equation and the measured calibration data is 0.051 kPa.

For a measured variable U that has various uncertainties (x_i), the total uncertainty is given by Eqn. A.1.

$$\delta U = \sqrt{\sum_{i=1}^{n} (\delta(x_i))^2} \qquad \text{A.1}$$

Using the pressure uncertainties calculated above, the total uncertainty in the pressure reading can be estimated by,

$$\delta P_{total} = \sqrt{(0.086)^2 + (0.012)^2 + (0.051)^2} = 0.101\ \text{kPa}$$

Mass Flow Rate ($\dot{m}$)

The water mass flow rate was measured using a Coriolis effect mass flowmeter. As specified by the manufacturer, the uncertainties associated with the reading of the mass flowmeter were,

- Maximum measured error: 0.3% of reading.
- Readability error: 0.1% of reading.

Using Eqn. A.1, the total uncertainty of the mass flowmeter was calculated to be 0.32% of reading.

Temperature

The thermocouples used in the experimental facility were calibrated to reduce measurement uncertainty. The E-type thermocouples were calibrated using a thermocouple calibrator for a temperature range between 40 °C to 200 °C. The calibrator utilized a well-insulated, electrically heated copper cylinder. The copper cylinder has dedicated holes, which contain thermal oil, for placing a resistive temperature device (RTD) (Omega Engineering Precision DP251) and the thermocouples. The temperatures measured by the E-type thermocouples were inside the range of the thermocouple calibrator.

Since the water temperatures, measured by T-type thermocouples, were not expected to be above (40 °C) the thermocouple calibrator was not suitable for calibrating the T-type thermocouples. Therefore, water bath chiller (Digital Plus RTE 7) was used for calibration. Again the reference temperature of the water bath was measured using an RTD.

The thermocouples and their accessories (wires, connectors, etc.) were connected directly to the measurement DAQ system. Therefore, except for the accuracy errors, the errors associated with thermocouple wire lengths, connections, linearity et cetera, were considered to be compensated for in the calibration. However, the errors associated with the RTD and the calibration curve must be considered. The major errors are considered below.

Uncertainty associated with the RTD

The uncertainty of the RTD is ±0.01 °C as stated by the manufacturer.

Uncertainty associated with the drift of the RTD

The annual drift of the RTD was estimated by Drnovsek et al. [A1] to be ±0.0075 °C/year. The total drift over 10 years is calculated to be ±0.075 °C.

Uncertainty associated with the RTD measurement device

The uncertainty of the RTD measurement device is ±0.01 °C as reported by the manufacturer.

Uncertainty associated with DAQ system

The uncertainty of the DAQ system was estimated to be ±0.1 °C.

Uncertainty associated with the calibration curves

The calibration data for each thermocouple were fitted using linear, parabolic quadratic, cubic fitting equations. Parabolic calibration curves were found to produce the smallest calibration errors. Therefore, parabolic calibration equations were used for all the thermocouples. The calibration errors for all the thermocouples are stated in Table A.1.

Using the information above, the thermocouple total uncertainty of the thermocouples can be calculated using Eqn. A.1. The uncertainty associated with the T-type and E-type thermocouples are shown in Tables A.1 and A.2 respectively.

Table A.1. Thermocouple uncertainty associated with the T-type thermocouples.

	T_{w_in1}	T_{w_in2}	T_{w_out1}	T_{w_out2}
	(°C)	(°C)	(°C)	(°C)
RTD bias	0.010	0.010	0.010	0.010
RTD reader bias	0.010	0.010	0.010	0.010
RTD drift	0.075	0.075	0.075	0.075
DAQ bias	0.100	0.100	0.100	0.100
Calibration error	0.014	0.013	0.016	0.016
Total uncertainty	**0.13**	**0.13**	**0.13**	**0.13**

Table A.2. Thermocouple uncertainty associated with the E-type thermocouples.

	T_{ss1}	T_{ss2}	T_{ss3}	T_{ss4}	T_{ss5}
	°C	°C	°C	°C	°C
RTD bias	0.010	0.010	0.010	0.010	0.010
RTD reader bias	0.010	0.010	0.010	0.010	0.010
RTD drift	0.075	0.075	0.075	0.075	0.075
DAQ bias	0.100	0.100	0.100	0.100	0.100
Calibration error	0.130	0.130	0.169	0.174	0.204
Total uncertainty °C	**0.18**	**0.18**	**0.21**	**0.21**	**0.24**

Table A.2 (continued)

	T_{ss6}	T_{ss7}	T_{ss8}	T_{ss9}	T_{ss10}
	°C	°C	°C	°C	°C
RTD bias	0.010	0.010	0.010	0.010	0.010
RTD reader bias	0.010	0.010	0.010	0.010	0.010
RTD drift	0.075	0.075	0.075	0.075	0.075
DAQ bias	0.100	0.100	0.100	0.100	0.100
Calibration error	0.075	0.117	0.060	0.089	0.193
Total uncertainty	**0.15**	**0.17**	**0.14**	**0.15**	**0.23**

The maximum uncertainty value of the E-Type thermocouples was found to be 0.24 °C.

Energy Supplied to the Electrical Heaters ($Q_{heaters}$)

The electrical power supplied to the electrical heaters ($Q_{heaters}$) was measured using a true RMS multimeter (Extech382860). The multimeter uncertainty was specified by the manufacturer to be 2% of reading + 5 least significant digits.

For the minichannels heat exchanger tests, the maximum input power was 855 W. The measurement uncertainty can be calculated to by

$$\delta Q_{heaters} = \left(\frac{2}{100} * 855 + 5\right) = 22.1\ W$$

$$\frac{\delta Q_{heaters}}{Q_{heaters}} = \frac{22.1}{855} * 100 = 2.6\ \%$$

A2. The Uncertainty in the Calculated Parameters

The error of the calculated parameter, δR, can be calculated using Eqn. A.2.

$$\delta R = \sqrt{\sum_{i=1}^{n} \left(\delta x_i \frac{\partial R}{\partial x_i}\right)^2} \tag{A.2}$$

where R is a mathematical function that depends on the independent arguments x_1 to x_n, $R = f(x_1, x_2, x_3, \ldots, x)$.

The relative error of R can be found by dividing the uncertainty δR by the measurement value, R.

$$\frac{\delta R}{R} = \sqrt{\sum_{i=1}^{n} \left(\frac{\delta x_i}{x_i}\right)^2} \tag{A.3}$$

Average Water Inlet and Outlet Temperatures ($\bar{T}_{w\_in}$, $\bar{T}_{w\_out}$)

The absolute uncertainty in the average inlet and outlet temperatures were calculated by Eqn. A.2.

$$\bar{T}_{w\_in} = \frac{1}{2}(T_{w\_in1} + T_{w\_in2}) \tag{A.4}$$

$$\delta \bar{T}_{w\_in} = \sqrt{\left(\delta T_{w\_in1} * \frac{\partial \bar{T}_{w\_in}}{\partial T_{w\_in1}}\right)^2 + \left(\delta T_{w\_in2} * \frac{\partial \bar{T}_{w\_in}}{\partial T_{w\_in2}}\right)^2}$$

$$\delta \bar{T}_{w\_in} = \left(\left(\frac{1}{2} * 0.13\right)^2 + \left(\frac{1}{2} * 0.13\right)^2\right)^{0.5} = 0.10\ °\text{C}$$

The same steps can be used to for calculating the error for $\delta \bar{T}_{w\_out}$ =0.10 °C.

Energy Transferred to the Cooling Water (Q_{water})

The energy transferred to the water is calculated using the following equation,

$$Q_{water} = \dot{m} C_p (\bar{T}_{w\_out} - \bar{T}_{w\_in}) \quad \text{(A.5)}$$

Using Eqn. A.2 the absolute uncertainty of Q_{water} becomes,

$$\delta Q_{water} = \left(\left(\delta\dot{m} C_p \left(\bar{T}_{w\_out} - \bar{T}_{w\_in} \right) \right)^2 + \left(\dot{m} \delta C_p \left(\bar{T}_{w\_out} - \bar{T}_{w\_in} \right) \right)^2 + \left(\dot{m} C_p \delta \bar{T}_{w\_out} \right)^2 + \left(\dot{m} C_p \delta \bar{T}_{w\_in} \right)^2 \right)^{-0.5}$$

The error in C_p was estimated by obtaining an equation of C_p as a function of temperature. Based on the uncertainty of the water thermocouples; the uncertainty of C_p was found to be 1.7 J/kg·K.

For the minichannels heat exchanger at $\dot{m}$ = 0.19 kg/s and $Q_{heaters}$ = 855 W the uncertainty of Q_{water} was estimated to be 101.6 W which corresponds to relative error of 11.3%.

Temperature Gradient $\left(\left(\frac{dT}{dx} \right)_{ss\_CL} \right)$ and Surface temperature (T'_{s_CL})

The reading from the thermocouples 4, 5, 6 and 7 was used to determine the temperature gradient $\left(\frac{dT}{dx} \right)_{ss\_CL}$ and the surface temperature T'_{s_CL} using the linear regressions analysis. The equation describing the temperature distribution in the SS block is given by,

$$T_i = T'_{s\_CL} - \left(\frac{dT}{dx} \right)_{ss\_CL} x_i \quad \text{(A.6)}$$

where: $\left(\frac{dT}{dx} \right)_{ss\_CL} = \frac{\sum (x_i - \bar{x})(T_i - \bar{T})}{\sum (x_i - \bar{x})^2}$ and $T'_{s\_CL} = \bar{T} - \left(\frac{dT}{dx} \right)_{ss\_CL} \bar{x}$. $\bar{x}$ and $\bar{T}$ are the average location of the thermocouples and average temperature in the SS block, respectively.

The standard deviation of the $\left(\frac{dT}{dx} \right)_{ss\_CL}$ and T'_{s_CL} can be computed using the following equations,

$$\sigma_{\frac{dT}{dx}} = \sigma_\epsilon \sqrt{\frac{1}{n} + \frac{\bar{x}^2}{\sum(x_i - \bar{x})^2}} \tag{A.7}$$

$$\sigma_{T_{s\_CL}} = \sigma_\epsilon \sqrt{\frac{1}{\sum(x_i - \bar{x})^2}} \tag{A.8}$$

The term n is the number of measurements. It is equal to 4 in this case. where $\sigma_\epsilon = \sqrt{\sigma_\epsilon^2}$ the term σ_ϵ^2 is called the mean square error of the regression, it is given by $\sigma_\epsilon^2 = \frac{SSE}{n-2}$. The term $SSE = \sum e_i^2$ is the sum of the squared residuals e_i. The residual e_i is the difference between the temperature predicted by the equation (T_i) and the actual measured temperature (T_m), e_i = T_m-T_i.

The calculated standard deviations ($\sigma_{\frac{dT}{dx}}, \sigma_{T_{s\_CL}}$) were multiplied by 2 to find the 95% confidence interval. The error of T'_{s_CL} was assumed to equal T_{s_CL}. The absolute error in T_{s_CL} was equal to 0.40 °C, at Q_{heater} = 855 W and $\dot{m}$ = 0.19 kg/s.

Log-mean temperature difference (T_{LM_CL})

The log mean temperature difference can be calculated by,

$$\Delta T_{LM\_CL} = \frac{\left(T_{s\_CL} - \bar{T}_{w\_out}\right) - \left(T_{s\_CL} - \bar{T}_{w\_in}\right)}{\ln\left(\frac{T_{s\_CL} - \bar{T}_{w\_out}}{T_{s\_CL} - \bar{T}_{w\_in}}\right)} \tag{A.9}$$

setting $\delta\Delta T_1 = \left(T_{s\_CL} - \bar{T}_{w\_out}\right)$ and $\delta\Delta T_2 = \left(T_{s\_CL} - \bar{T}_{w\_in}\right)$, Eqn. A.9 can be rearranged to become,

$$\Delta T_{LM\_CL} = \frac{\Delta T_1 - \Delta T_1}{\ln\left(\frac{\Delta T_1}{\Delta T_2}\right)} \tag{A.10}$$

The partial derivatives of $\Delta T_{LM_CL}$with respect to ΔT_1 and ΔT_2 are,

$$\frac{\partial \Delta T_{LM\_CL}}{\partial \Delta T_1} = \frac{\ln\left(\frac{\Delta T_1}{\Delta T_2}\right) - \left(1 - \frac{\Delta T_2}{\Delta T_1}\right)}{\left[\ln\left(\frac{\Delta T_1}{\Delta T_2}\right)\right]^2} \text{ and } \frac{\partial \Delta T_{LM\_CL}}{\partial \Delta T_2} = \frac{-\ln\left(\frac{\Delta T_1}{\Delta T_2}\right) + \left(\frac{\Delta T_1}{\Delta T_2} - 1\right)}{\left[\ln\left(\frac{\Delta T_1}{\Delta T_2}\right)\right]^2}$$

Using the derived partial derivatives in Eqn. A.2, the equation describing the uncertainty in δT_{LM_CL} becomes,

$$\delta T_{LM\_CL} = \sqrt{\left(\frac{\partial \Delta T_{LM\_CL}}{\partial \Delta T_1} * \delta \Delta T_1\right)^2 + \left(\frac{\partial \Delta T_{LM\_CL}}{\partial \Delta T_2} * \delta \Delta T_2\right)^2} \qquad \text{(A.11)}$$

where $\delta \Delta T_1 = \sqrt{\left(\delta T_{s\_CL}\right)^2 + \left(\delta \bar{T}_{w\_out}\right)^2}$ and $\delta \Delta T_2 = \sqrt{\left(\delta T_{s\_CL}\right)^2 + \left(\delta \bar{T}_{w\_in}\right)^2}$.

The error values of T_{s_CL}, $\bar{T}_{w\_out}$ and $\bar{T}_{w\_in}$ were calculated above. $\delta \Delta T_1$ and $\delta \Delta T_2$ were calculated and used, in Eqn. A.11, along with the partial derivatives to determine the relative uncertainty in T_{LM_CL} which was found to be 7.9%.

Thermal conductance (hA)

The equation describing the thermal conductance is $hA = \frac{Q_{water}}{\Delta T_{LM\_CL}}$. The relative uncertainty in hA can be found using Eqn. A.3.

$$\frac{\delta hA}{hA} = \sqrt{\left(\frac{\delta Q_{water}}{Q_{water}}\right)^2 + \left(\frac{\delta \Delta T_{LM\_CL}}{\Delta T_{LM\_CL}}\right)^2} \qquad \text{(A.12)}$$

Using the relative errors of Q_{water} and ΔT_{LM_CL} (calculated above), the uncertainty in hA = 13.8%.

Nusselt number (Nu)

For the minichannels heat exchanger, the Nusselt number is given by $Nu = \left(\frac{hD_h}{k_w}\right)$. The relative error in the Nusselt number can be calculated using the following equation,

$$\frac{\delta Nu}{Nu} = \sqrt{\left(\frac{\delta h}{h}\right)^2 + \left(\frac{\delta D_h}{D_h}\right)^2 + \left(\frac{\delta k_w}{k_w}\right)^2} \quad \text{(A.13)}$$

- Based on the CNC milling machine tolerances, the relative error in D_h was estimated to be about 2%.
- The relative error in thermal conductivity was estimated to be 0.3%
- The relative error in the heat transfer coefficient h was calculated using the error in hA and the error associated with A. It was found that the error in h is equal to 13.9%.

Using the listed uncertainties, the total relative uncertainty in Nu was found to be 14%.

Pumping power (P_p)

The pumping power required for coolant circulation is $P_p = \frac{\dot{m}\Delta P}{\rho_w}$. Therefore the relative error in P_p is given by the following equation,

$$\frac{\delta P_p}{P_p} = \sqrt{\left(\frac{\delta \dot{m}}{\dot{m}}\right)^2 + \left(\frac{\delta \rho_w}{\rho_w}\right)^2 + \left(\frac{\delta \Delta P}{\Delta P}\right)^2} \quad \text{(A.14)}$$

For the minichannels heat exchanger, at $\dot{m}$ = 0.19 kg/s, the measured pressure drop was ΔP = 23.3 kPa.

- The relative error in $\dot{m}$ is 0.32% of reading.
- The relative error in ΔP was calculated to be 0.43%.
- The error in ρ_w was negligible.

Based on these error values, the relative error in P_p was equal to 0.54%.

Reynolds number (Re)

The Reynolds number for the minichannels heat exchanger is defined as $Re = \rho_w V D_h / \mu_w$. The equation describing the relative error in Re is,

$$\frac{\delta Re}{Re} = \sqrt{\left(\frac{\delta V}{V}\right)^2 + \left(\frac{\delta \rho_w}{\rho_w}\right)^2 + \left(\frac{\delta D_h}{D_h}\right)^2 + \left(\frac{\delta \mu_w}{\mu_w}\right)^2} \qquad \text{(A.15)}$$

- $V = (\dot{m}/N_c)/(\rho_w A_{flow})$ is the flow velocity in a minichannel. At $\dot{m}$ = 0.19 kg/s, the relative error in V was calculated to be 2.9%.
- Based on the uncertainty in the temperature reading, the relative uncertainty associated with the fluid viscosity, μ_w, was found to be 6.5%.
- As mentioned before, relative uncertainty in the density was negligible. The relative error in D_h was 2%.

Using the error values calculated above, the total relative uncertainty in Re was found to be 7.4%.

References

[A1] J. Drnovsek, I. Pusnik, J. Bojkovski, "Reduction of uncertainties in temperature calibrations by comparison," *Measurement Science and Technology*, vol. 9, pp. 1907-1911, 1998.

Appendix B: The TEG POWER System Model

The POWER system is designed to recover thermal energy from the exhaust gases of a commercial pizza oven. The purpose of the system model is to investigate the effect of using the different cold side heat exchanger designs on the performance of the TEG POWER system. A particular parameter of interest is the amount of total electrical power generated. The TEG POWER system is composed of four main components which are: the hot side heat exchanger, the 48 thermoelectric generators and two cold side heat exchangers (24 TEG per 1 cold side heat exchanger). Figure B.1 is a schematic depicting the TEG POWER system, the thermal resistance of each component and the temperature at various locations are also illustrated.

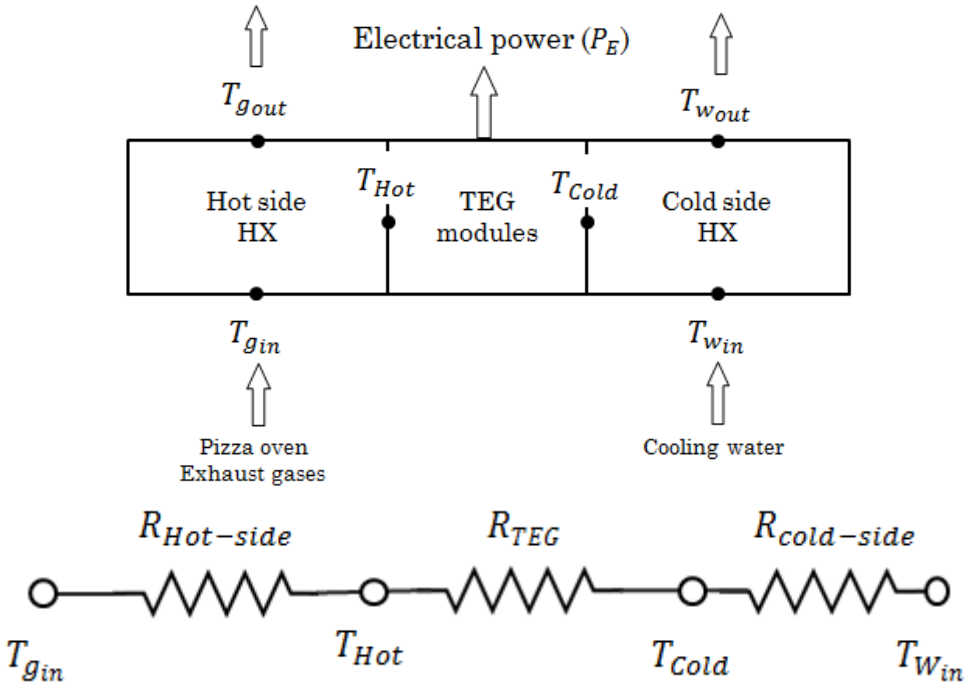

Figure B.1. A schematic depicting the TEG POWER system and the corresponding thermal resistance diagram of the system.

B.1. TEG POWER System Model

The current generation of the TEG POWER system is composed of the following components a commercial pizza oven, a pin fin array acting as the hot side heat exchanger, 48 TEG modules for electrical power generation and two full scale impinging jets heat exchanger acting as the cold side heat exchanger. The full scale impinging jets heat exchanger have an identical design as impinging jets heat exchanger prototype tested in this thesis.

The Pizza Oven

The TEG POWER system utilized a commercial pizza oven rated (Q_{oven}) at 15.3 kW of thermal energy at full operation. The typical cooking temperature (T_{cook}) of a regular pizza is about 300 °C. Assuming the inlet air temperature to the oven is 25 °C the mass flow rate of exhaust gases ($\dot{m}_g$) required can be calculated using the following equation

$$Q_{oven} = \dot{m}_g \, C_p \, (T_{cook} - T_{room}) \qquad \text{(B.1)}$$

The exhaust gases are assumed to be air. All the properties of air are evaluated at the average gas temperature of $\frac{T_{cook}+T_{room}}{2}$, using Eqn. B.1 the air mass flow rate is found to be 0.055 kg/s. It should be noted that the exhaust gas temperature is lower than the cooling temperature. This is due to convection, radiation and infiltration losses from the oven. For example, experiments with the pizza oven indicated that for an oven set point of 315 °C (600 °F) the exhaust gas temperature is around 270 °C.

The Hot Side Heat Exchanger (Pin Fin Heat Exchanger)

The pin fin heat exchanger is made from 354 pin fins 9.52 mm (3/8") in diameter and 101.6 mm (4 in) long. The pin fin heat exchanger is made from aluminum 6061-T6. The available heat transfer area for the pin fin heat

exchanger is 1.08 m². Figure B.2 illustrates the design of the pin fin heat exchanger.

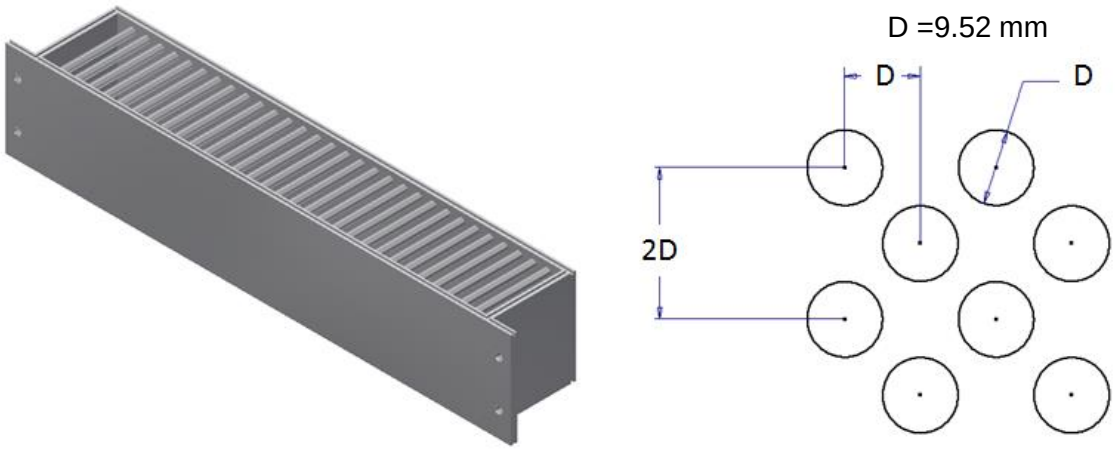

Figure B.2. A CAD model showing the design of the pin fin array (left), and the staggered pin fin geometry and its dimensions (right).

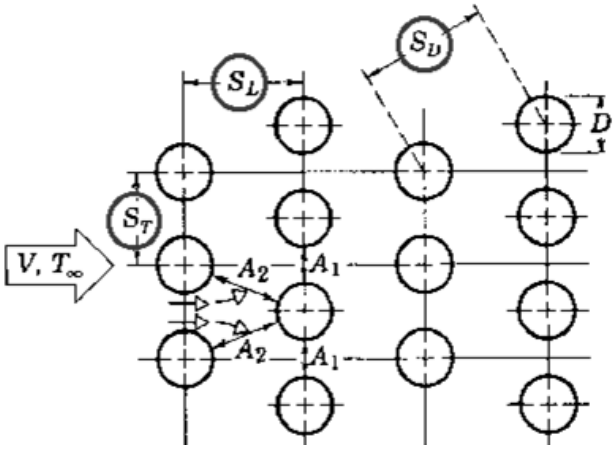

Figure B.3. The geometrical parameters associated with a staggered pin fin array [51].

To quantify the heat transfer from the pin fin array the Re_D and Nu must be calculated for the pin fin geometry. The following steps are used to find Re_D which is later used to find Nu and the heat transfer coefficient (h).

The hot exhaust gases from the pizza oven enter the pin fin heat exchanger via a straight rectangular shape duct 609.6 mm × 101.6 mm (24" ×

4"), the duct cross sectional area (A_{duct}) is found to be 0.06193 m^2. The fluid approach velocity (V) (i.e. before the pin fin array, refer to Figure B.3) can be calculated using by

$$V = \frac{\dot{m}_g}{\rho_{air} A_{duct}} \tag{B.2}$$

The exhaust gases are assumed to have similar properties as air. All the air properties were evaluated at the average exhaust gases temperature which is $\frac{T_{g_{in}} + T_{g_{out}}}{2}$. The approach velocity (V) for the exhaust gases was found to be 8.81×10^{-4} m/s. The maximum velocity (V_{max}) that occurs inside the pin fin array can be calculated using the pin fin array geometry and the fluid properties.

$$V_{max} = \frac{S_T}{2(S_D - D)} V \tag{B.3}$$

where S_D is the longitudinal pitch. S_D is a function of the transverse pitch (S_T) and the longitudinal pitch (S_L), $S_D = \left(S_L^2 + \left(\frac{S_T}{2}\right)^2\right)^{0.5}$. For the pin fin array, the values of S_L and S_T are equal to 9.52 mm and 19.52 mm, respectively, which yielded a value of S_D of 13.47 mm. Using the values of V, S_T and S_D in Eqn. B.3, the value of V_{max} was found to be 2.1×10^{-3} m/s. The value of V_{max} can be used to calculate the Reynolds number of the pin fins arrays (Re_D).

$$Re_D = \frac{\rho_{air} V_{max} D}{\mu_g} \tag{B.4}$$

where V_{max}, air properties and pin diameter (D) was used to calculated the Re_D which was found to be 964.8. For staggered grids with $500 < Re_D < 1000$ Zukauskas presented the following correlation for predicting the Nusselt (from [51]),

$$Nu_D = 0.71 Re_D^{0.5} Pr^{0.36} \left(\frac{Pr}{Pr_s}\right)^{0.25} \tag{B.5}$$

where Pr_s is evaluated at the fin surface temperature T_s. The value of $\frac{Pr}{Pr_s}$ was approximately equal to 1, Pr was equal to 0.7014 at the average exhaust temperature and Re_D for the pin fin array was 964.8. For these conditions Nu for the pin fin array was 19.5; which corresponded to a heat transfer coefficient (h) of 60.6 W/m^{2}K. Given that the heat transfer area of the pin fin array is 1.08 m^2 the thermal conductance (hA) for the pin fin array is 65.5 W/K. The fin efficiency equations (discussed in 3.1.1) were used to estimate the pin fin efficiency which was found to be 89% for the specified fin geometry. The total heat transfer from the pin fin array can be quantified by the following equation,

$$Q_{hot-side} = 58.16 \left(\frac{\left(T_{g_{in}} - T_{Hot}\right) - \left(T_{g_{out}} - T_{Hot}\right)}{\ln \frac{\left(T_{g_{in}} - T_{Hot}\right)}{\left(T_{g_{out}} - T_{Hot}\right)}} \right) \qquad \text{(B.6)}$$

where T_{Hot} is the surface temperature of the pin fin array, $T_{g_{in}}$ and $T_{g_{out}}$ are the inlet and outlet exhaust temperatures to/from the pin fin array. $T_{g_{in}}$ is a function of the oven set point temperature at an oven set point of 315 °C (600 °F) the exhaust gas temperature $T_{g_{in}}$ is 272 °C. Note that the T_{Hot} and $T_{g_{out}}$ are not known, therefore $T_{g_{out}}$ has to be assumed in order to calculate T_{Hot}. Once $T_{g_{out}}$ is specified, the heat transfer from the exhaust gases to the pin fin array ($Q_{hot-side}$) can be calculated. $Q_{hot-side}$ is equal to the heat lost by the exhaust gas stream which given by,

$$Q_{hot-side} = \dot{m}_g \, C_p \, (T_{g_{in}} - T_{g_{out}}) \qquad \text{(B.7)}$$

The TEG Modules

The performance of TEG modules as a function of hot side and cold side surface temperatures T_{Hot} and T_{Cold} was studied by Finnerty [8], mechanistic

models were presented for calculating the short circuit current (I_{sc}) and the open circuit voltage (V_{oc}) for TEG 1.

$$I_{sc} = 0.9485 + 0.0338\,T_{Hot} - 0.045\,T_{Cold} \quad \text{(B.8)}$$

$$V_{oc} = 0.6228 + 0.0102\,T_{Hot} - 0.018\,T_{Cold} \quad \text{(B.9)}$$

The values of I_{sc} and V_{oc} can be used to calculated the TEG electrical resistance (R_{E_TEG}) and the Seebeck coefficient (α) and the electrical power generated (at the matched load condition) by a single TEG (P_{E_TEG}) which are given by the following equations.

$$R_{E\_TEG} = \frac{V_{oc}}{I_{sc}} \quad \text{(B.10)}$$

$$\alpha = \frac{V_{oc}}{(T_{Hot} - T_{Cold})} \quad \text{(B.11)}$$

$$P_{E\_TEG} = \frac{V_{oc} I_{sc}}{4} \quad \text{(B.12)}$$

The total thermal conductivity for a single TEG (K_{TEG}) has two components a thermal component ($K_{Thermal}$) and an electrical component. The total thermal conductivity for a single TEG (K_{TEG}) as given by the following equation.

$$K_{TEG} = 2.6 \times \frac{\alpha^2 (T_{Hot} + T_{Cold})/2}{2 * R_{E\_TEG}} + K_{Thermal} \quad \text{(B.13)}$$

The thermal component of the thermal conductance is approximately equal to 0.7 W/K. The total thermal conductivity (K) of the 48 TEGs will be equal to 48 $\times K_{TEG}$. Similarly, the total electrical power (P_E) generated by the 48 TEGs will be equal to $48 \times P_{E\_TEG}$.

Note that all TEG parameters depend on T_{Hot} and T_{cold}. At this stage T_{Hot} is known but T_{cold} is not, therefore it has to be assumed and checked later. Once T_{Hot} and T_{cold} are specified. All the TEG parameters (Eqns. B.10 to B.13) can be calculated.

The Cold Side Heat Exchangers

The cooling water flowing through the cold side heat exchanger ($T_{w_{in}}$) will have a fixed inlet temperature of 16 °C. From energy balance the heat transferred to the cold side heat exchanger ($Q_{cold-side}$) is equal to $Q_{hot-side} - P_E$. The outlet water temperature ($T_{w_{out}}$) can be determined using

$$Q_{Cold-side} = Q_{hot-side} - P_E = \dot{m}_w C_p \left(T_{w_{out}} - T_{w_{in}}\right) \quad \text{(B.14)}$$

The heat transferred from the TEG cols side surface to the cooling water is given by,

$$Q_{Cold-side} = hA_{cold-side} \left(\frac{\left(T_{w_{in}} - T_{Cold}\right) - \left(T_{w_{out}} - T_{Cold}\right)}{\ln \frac{\left(T_{w_{in}} - T_{Cold}\right)}{\left(T_{w_{out}} - T_{Cold}\right)}} \right) \quad \text{(B.15)}$$

The purpose of the system model is to determine the effect of using the different heat exchanger design on the performance of the TEG POWER system. To achieve this task, the hot side flow conditions will be kept constant (i.e. $hA_{Hot-side}$) and the thermal conditions ($hA_{cold-side}$) at the cold side will be altered. Altering the $hA_{cold-side}$ at the cold side can be achieved by either changing the cold side heat exchanger or coolant flow rate circulating through the cold side heat exchanger.

Upon the determination of $hA_{cold-side}$, it can be inserted into Eqn. C.15 in order to calculate an updated value of the cold side surface temperature (called T^*_{Cold}). If T^*_{Cold} is not equal to T_{cold} then the guess of T_{cold} has to be updated by setting it equal to T^*_{Cold}.

Total Energy Flow through the TEGs Modules

An updated value of the hot side surface temperature (called T^*_{Hot}) can be calculated based on the thermal conductivity of the 48 TEGs (K). The amount of energy flowing through the TEG (Q_{Hot}) can be estimated by,

$$Q_{Hot-side} = K(T^*_{Hot} - T^*_{Cold}) \quad \text{(B.16)}$$

Based on the updated value of T^*_{Hot}, an updated value of exhaust gas outlet temperature ($T^*_{g_{out}}$) can be calculated. If the updated value gas outlet temperature ($T^*_{g_{out}}$) is not equal to the assumed value of $T_{g_{out}}$ then the solution has not converged yet and $T_{g_{out}}$ has to be updated by setting it equal to $T^*_{g_{out}}$. The iteration process should continue until convergence meaning that the assumed values do not change anymore.

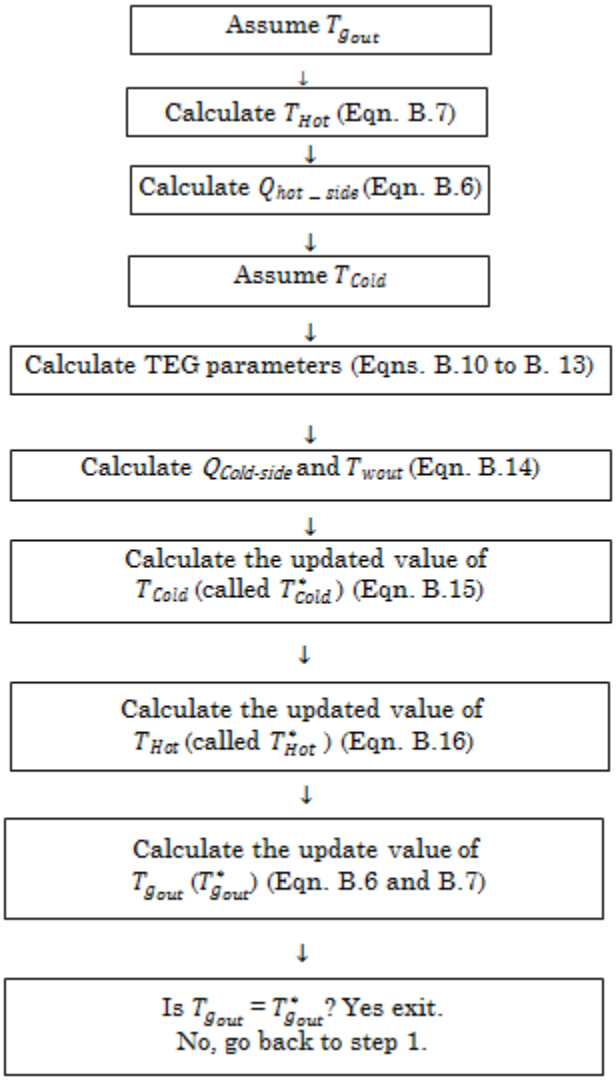

Figure B.4. A tree diagram showing the iteration process required to calculate the performance of the TEG POWER Project.

Validating the System Model Predictions with the Experimental Results of the TEG POWER System

The numerical system model is validated using experimental results obtained using the existing TEG POWER system set up. The TEG POWER system utilizes two full scale impinging jets heat exchanger designs each capable of cooling 24 TEGs, while the pin fin array is used as the hot side heat exchanger. The full scale impinging jets heat exchanger has the same design as the tested impinging jets heat exchanger prototype.

For the system model the developed impinging jets correlation (Eqn. 5.15) is used to calculate the thermal conductance of the impinging jets cold side heat exchangers. The thermal performance of the pin fin array and the TEG can be modelled using equations B.5-B.13 , respectively.

The model validation is based on comparing the thermal energy harvested from the exhaust gas stream (Q) and the total electrical power generated by the 48 TEG modules (P_E). The experimental data are for an oven set temperature of 315 °C (600 °F) for which the inlet temperature of the exhaust gases is $T_{g_{in}}$ was around 262 °C. The system model validation results are presented in Table B.1.

Table B.1. Comparing the experimental results from the TEG POWER system and the developed system model.

	Experimental results from the TEG POWER system		Developed system model results		% difference in P_E	% difference in Q
$\dot{m}_{system}$ (kg/s)	P_E(kW)	Q (W)	P_E (kW)	Q (kW)		
0.21	104	4.13	78	4.12	25.0	0.24
0.18	102	4.07	76	4.09	25.5	-0.49
0.08	93	3.89	65	3.93	30.1	-1.02

Table B.1 indicates that the developed system model is capable of accurately predicting the harvested thermal energy (Q) within 1%. It can be seen that the experimental results of P_E are not in good agreement with the predicted results by the model. The system model predictions for the total electrical power generated are about 25% to 30% lower compared to the experimental results. The discrepancy in P_E could be attributed to the TEG electrical performance variability and different thermal conditions at the TEG's cold and hot side between the developed correlations (Eqns. B.8 and B.10) and the TEG POWER system.

Based on the validation results, the developed system model can be used to predict the performance of the TEG POWER system. In addition, the system model can be used to study the effect of implementing different cold side heat exchanger designs on the overall performance of the TEG POWER system.